LI

# THE IMPLEMENTATION OF OPTIMAL FULL STATE FEEDBACK USING AREA AVERAGING SENSORS

Patrick Anthony Cazeau

S. B., Aeronautics and Astronautics,
Massachusetts Institute of Technology, 1992

Submitted to the Department of Aeronautics and Astronautics
in Partial Fulfillment of the Requirements
for the Degree of

## MASTER OF SCIENCE

at the

## MASSACHUSETTS INSTITUTE OF TECHNOLOGY

May 1994

Signature of Author_____
Department of Aeronautics and Astronautics
May 18, 1994

Certified by_____
Dr. David W. Miller
Principal Research Scientist.Thesis Supervisor

Accepted by_____
Professor Harold Y. Wachman
Chairman, Department Graduate Committee

1

# THE IMPLEMENTATION OF
# OPTIMAL FULL STATE FEEDBACK
# USING AREA AVERAGING SENSORS

Patrick Anthony Cazeau

## ABSTRACT

This paper describes the implementation of a Linear Quadratic Regulator (LQR) control design for an infinite-order cantilevered structure. The control design is derived and interpreted in terms of spatially distributed feedback kernels acting on measurements of spatially continuous curvature and curvature rate state functions. Predictions of the exact spatially distributed feedback kernels are found computationally and, through the use of area averaging sensors, implemented experimentally. The sensor shapes depend on the particular state and control weighting chosen in the formulation of the LQR cost. Two performance metrics are considered, and experimental closed-loop results are provided to verify that predicted performance is actually achieved.

Thesis Advisor:     Dr. David W. Miller

Title:              Principal Research Scientist,

                    MIT Space Engineering Research Center

# Acknowledgments

I would like to dedicate this thesis to my mother, Jesula, whose love and care has motivated and inspired me to succeed in this life. I would like to thank my father, Albert. Through his hard work, he has supported me and served as my role model in my studies at MIT. Mom and Dad, I love you very much, and I hope that this work makes you proud. I would also like to thank Nicholas, Cheryl, Marie, and Peter and my entire family for their support. I would like to especially thank Ronnie for her love, patience, inspiration and care. You've given me so much that I can never repay, and I love you for that. I am very grateful for the support of all my friends, to my unified-partners-in-crime Ben, Scot, and Paul. Ben, you have always been there for me. Through unified, Theta Chi, MCS, and the endless list of classes and problem sets and projects and presentations and all-nighters. I won't ever forget that. You're okay.

I would like to thank my thesis advisor, Dave Miller, for the hours spent counseling and guiding me, and for the hours listening to my crazy ideas. I would also like to thank Professor Dugundji for the wealth of knowledge his classes brought me. I would like to thank God for all of these people, and for structural dynamics, piezoelectric materials, optimal control, and all the crazy things that interest me that I can make a living from.

3

# Table of Contents

# List of Figures

# List of Tables

# Nomenclature

## Roman

| | |
|---|---|
| $a(x)$ | Infinite-order companion matrix |
| $a_i, b_i, c_i, d_i$ | Unknown coefficients in cubic spline relation |
| $b$ | Beam width |
| $b_s$ | Structural forcing gain matrix |
| $b(x)$ | Infinite-order control transmission matrix |
| $c_c^j, c_{cr}^j$ | Modal contribution vectors |
| $e_{31}$ | Piezoelectric field intensity constant |
| $\tilde{f}, f, f(x,t), f_d, f_{dr}$ | Force, feedback force |
| $g_{cker}, g_{cker}$ | Curvature, curvature rate gains |
| $h$ | Beam thickness |
| $l_i, l_{i-1}, l_e$ | Coordinates for element, length of element |
| $m$ | Element matrix |
| $q$ | Infinite-order state weighting |
| $r$ | Infinite-order control weighting |
| $s$ | inter-element constraint matrix |
| $t$ | Time variable |
| $u$ | Geometric boundary constraint matrix |
| $v$ | Length variable in convolution expressions |
| $w, \dot{w}, \ddot{w}$ | Displacement, rate, acceleration state vectors |
| $w_i$ | Element generalized displacement state vector |
| $x$ | Length variable |
| $x_o$ | Location at which actuation is applied |
| $y$ | Performance output |
| $z$ | Global state vector |
| $z_p, z_s$ | Modeled and unmodeled states |
| $A$ | Finite-order companion matrix |
| $A_{pp}, A_{ps}, A_{sp},$ and $A_{ss}$ | Parts of companion matrix |

| | |
|---|---|
| $B$ | Finite-order control transmission matrix |
| $B_p, B_s$ | Parts of control transmission matrix |
| $C$ | Performance output matrix |
| $C_s$ | Structural damping Matrix |
| $C_f$ | Piezofilm capacitance |
| $E$ | Beam Modulus of elasticity |
| $E_o$ | Logarithmic error |
| $EI$ | Beam rigidity |
| $F(x)$ | Piezofilm electrode shape |
| $G_{nom}$ | Nominal transfer function |
| $G_{LTF}$ | Loop transfer function |
| $G_{fit}, G_{fit\,1}, G_{fit\,2}$ | Approximations to desired transfer functions |
| $G_{cker}, G_{crker}$ | Curvature, curvature rate kernel transfer functions |
| $H_p(j\varpi)$ | Modeled sensor-element transfer functions |
| $I$ | Beam moment of inertia about y-axis |
| $K_s$ | Structural stiffness matrix |
| $K_d(x), K_{dr}(x)$ | Displacement, displacement rate kernels |
| $K_c(x), K_{cr}(x)$ | Curvature, curvature rate kernels |
| $L$ | Beam length |
| $M_s$ | Structural mass matrix |
| $M$ | Global matrix |
| $N$ | Number of beam elements |
| $P(x)$ | Interpolation function matrix |
| $Q$ | State weighting matrix |
| $R$ | Control weighting matrix |

# Greek

| | |
|---|---|
| $\alpha, \alpha_i$ | Displacement kernel coefficient vectors |
| $\beta(x)$ | Length variable vector for kernel cubic spline |
| $\delta x, \delta t$ | Differentiation in length, time |
| $\varepsilon(x,t)$ | Beam surface strain |
| $\gamma, \gamma_t$ | Displacement rate kernel coefficient vectors |
| $\varphi_r$ | Curvature mode shape functions |
| $\kappa_d, \kappa_{dr}$ | Displacement, displacement rate kernels |

10

| | |
|---|---|
| $\kappa_1, \kappa_2$ | Displacement, control gains |
| $\lambda_r$ | Beam wave number |
| $\rho$ | Control weighting |
| $\rho A$ | Beam mass per unit length |
| $\sigma$ | Solution to infinite-order functional Ricatti equation |
| $\tau$ | Limit time variable |
| $\varpi$ | Frequency variable |
| $\omega(x,t)$ | Continuous displacement state function |
| $\zeta(x,t)$ | Infinite-order state vector |
| $\Sigma$ | Solution to finite-order algebraic Ricatti equation |
| $\Psi$ | Curvature mode shape matrix |

# Other Symbols

| | |
|---|---|
| $\Im$ | Linear Quadratic Regulator performance index |
| $\langle ..,.. \rangle$ | Inner product |
| $(...)^{\mathrm{T}}$ | Complex-conjugate transpose |
| $(\cdots)*(\cdots)$ | Convolution |
| $\overline{(\cdots)}$ | Adjoint |

# Chapter 1

# Introduction

## 1.1 THE NEED FOR SMART STRUCTURES

All structures are infinite-order systems, possessing an infinite number of resonant vibration modes. Each resonant mode is a particular form of motion that the structure experiences. They occur at particular frequencies of excitation. When most structures are disturbed from a rest state, their lower frequency modes dominate the overall motion. Aircraft surfaces, helicopter blades, solar arrays and other flexible, lightweight structures all tend to vibrate at these lower frequencies when disturbed by exterior influences. There are many advantages to the use of lightweight structures, but their sensitivity to disturbances is not desirable.

An advantage that heavier, rigid structures have is their insensitivity to disturbances. However, such massive structures violate the weight and cost efficiency requirements for many applications, including aircraft and spacecraft design. Lightweight structures are compatible with these applications, but their lightly-damped behavior can limit their applicability. What would be desirable is to have structures behave more like rigid masses without actually having to add large amounts of mass to their design. This can be achieved by integrating a method of regulating the motion of the structure in to its design. These smarter, lightweight structures would move to and remain in commanded positions

without experiencing large vibrations. A regulator, using sensors and actuators to measure and influence the motion, would allow for the vibration control of lightweight structures to be achieved. A common type of regulator is a feedback controller [1], using measurements of a system's status to determine the correct command signals to regulate some aspect of the system. Many controllers for structures require the use of sensors and actuators at multiple locations. The devices must therefore be lightweight, rugged, and compact so that their presence doesn't change or hinder the structure's functionality.

Piezoelectric materials can be used in this type of control design. They can be used as sensors that produce an output voltage proportional to any induced strain. They can also be used as actuators that elongate or contract when a voltage is applied to them. Some piezoelectric materials serve one of these functions better than the other. Most of them are durable and lightweight, and they can be glued on or imbedded into a structure without significantly changing the system's overall dynamics.

One type of piezoelectric material is polyvinylidene floride (PVDF). PVDF is a long chain polymer film. Straining the film causes a voltage across its two sides to be generated. Many beneficial sensing applications using PVDF film have been developed [2], since the relationship between the measured voltage and the applied strain is linear for a large range of operation. The film is also durable and flexible, allowing for its ease of integration into the structural design. Each side of the film is coated with a vapor-deposited metal electrode. The electrodes can be interpreted as spatial sensitivity weighting functions. They can be shaped by the control designer to provide different filtering properties [3, 4, 5, 6, 17, 27, 31]. Several researchers have demonstrated some of the different innovative properties that are possible. Collins and Miller [3, 4] researched many different applications of PVDF film, including the determination of certain sensor

electrode shapes that would provide roll-off without phase lag. Collins [3, 4] and Lee [5] investigated the use of film sensors with mode-shaped electrodes, and Burke and Hubbard [27] looked the properties of PVDF film with rectangular and triangular electrode shapes. These PVDF film sensors with shaped electrodes are part of a class of measurement devices called area averaging sensors [7]. An area averaging sensor is any form of apparatus providing a continuously distributed measurement. The PVDF film is a useful medium for creating area averaging sensors which give a distributed measurement of surface strain.

The voltage output of an PVDF area averaging sensor is proportional to the average surface strain over the area covered by the electrodes. The sensors have an advantage over point sensors in that they can provide distributed sensing. They can measure and filter information about the structure over the entire area that they cover. They can also provide filtered information about a single location. All these advantages are a function of the shape of the sensor electrodes, and they can be exploited in different vibration control designs for structures [3, 4, 5, 6, 17, 27, 31].

## 1.2   FEEDBACK CONTROL DESIGNS FOR STRUCTURES

Various feedback control designs exist to reduce the vibration of structures. The controllers work to damp the structural motion, essentially reducing their sensitivity to disturbances. They can also stiffen the structure by shifting the vibration frequencies to higher values. Shifting the frequencies to higher values also benefits the structure's response to commands. The optimal time response for the structure is achieved with the right combination of dampening and stiffening.

In establishing a control design, some measurable aspect of the structure's motion is defined as the performance output. Reducing unwanted vibrations of the structure corresponds to minimizing the effect of exterior disturbances on this performance output. For example, with an aircraft wing, it is of considerable interest to reduce any deflection of the tip of the wing due to wind disturbances during flight. It is also of interest to reduce any twisting of the wing tip caused during maneuvers. The performance output could consist of one or both of these motions. The criterion for a good control design could be based on a combination of the time response and steady state value of the performance, or on minimizing some cost functional associated with the performance. The task of finding the best design can be an iterative process, where the optimal design would achieve the best time response and steady state value combination or the lowest cost.

Optimal control design techniques exist that can accomplish this task [8, 28]. One of the basic techniques is the Linear Quadratic Regulator (LQR) control design [8]. The LQR control design minimizes a quadratic performance index based on the measured motion of the structure and the control authority of the actuators. The minimization leads to the development of a control law. The control law defines a feedback command signal which uses information about the global motion of the structure to reduce the vibration. Applying the LQR control design calls for a mathematically exact model of the structure's behavior, capturing all of its resonant modes. Such a model requires the use of the continuous, partial differential equation of motion for the structure subjected to the appropriate boundary conditions. The structure's motion in this infinite-order model is described in terms of continuous state functions. The LQR feedback command signal relies on information from these state functions to reduce the vibration.

In practice it is difficult or impossible to find an exact, closed-form LQR control design for most infinite-order structures, except in some particular cases [9]. Therefore, infinite-order structures are often modeled in a discrete framework, using only a finite number of states. Finite element methods and finite difference methods [10] are a few common examples among the many methodologies used to develop finite-order control design models. The states are the modeled degrees-of-freedom of the structure. They provide information about a particular location on the structure. The equation of motion for a single state is applied at each location. The equations collectively form a matrix ordinary differential equation, which serves as the finite-order model of the structure. The finite-order model gives an approximation of the global motion in terms of the states. For a model of this form, the exact LQR control design can be found computationally. The feedback control law defines the needed feedback signal as a linear combination of all the states of the model multiplied by feedback gains.

There are many problems with applying a finite-order control design to an infinite-order structure. The finite-order model is essentially a truncated model of the structure's behavior. Given that model truncation is one of the main contributors to the spillover problem [11], it is best to include as many states in the finite-order model as possible to increase the fidelity. This is a costly approach, both in terms of computation and implementation. An increased number of modeled states requires the use of more feedback sensors in the implementation. The compensator used to generate the feedback signal will need to multiply more feedback gains with the increased number of state measurements. Also, the larger the size of the finite-order model, the more time and effort it takes to calculate the needed LQR feedback gains. These aspects decrease the attractiveness and the efficiency of applying a finite-order LQR

control design to an infinite-order structure. The problems are all a result of the fact that the points sensors cannot provide all the information that is needed.

There is, however, a novel approach to implementing the LQR control design that can circumvent these problems. The alternate method of implementation is based on the infinite-order formulation of the LQR control design. Instead of using point sensors, it employs area averaging sensors to provide the needed feedback signal [7]. The formulation of the LQR control design in an infinite-order framework defines the feedback control signal as a convolution of spatially distributed feedback kernels with spatially continuous state functions [9]. The state functions are those used to describe the spatial motion of the structure in the continuous equation of motion. The feedback kernels are spatial weightings on those functions. The implementation of this type of signal requires continuously distributed measurements, which can be provided for with area averaging sensors.

## 1.3    USEFULNESS OF AREA AVERAGING SENSORS

It is of particular interest in this thesis to investigate the behavior of PVDF area averaging sensors on beams. Beams are very important structural elements, and there are many systems which are simple cantilevered beams. Aircraft wings, rotor blades, solar arrays, robot arms and helicopter blades are among a few common examples. For an area averaging sensor attached to a simple cantilevered beam, the voltage output has been shown to be the convolution of the spatial sensitivity weighting function of the sensor with the beam's curvature state function [7]. This parallel 'convolution' relation between the infinite-order LQR control law and the output of an area averaging sensor attached to a cantilevered beam is very useful. The sensor electrode shapes can be related to

the shape of the continuous feedback kernels from the infinite-order control law. Area averaging sensors with certain electrode shapes would allow for an optimal LQR vibration control solution to be implemented on a cantilevered structure.

What is needed to accomplish this is a method of calculating the feedback kernels for specific LQR designs, which cannot be determined directly from an infinite-order model of the beam. What can be determined with ease are the feedback gains for a finite-order LQR control design. The solutions found for the finite-order design are related to the infinite-order case, and the relation can be used to solve for the kernels.

## 1.4    THESIS OUTLINE

This thesis develops the infinite-order LQR control design for beams as well as a method of implementation using PVDF area averaging sensors. In Chapter 2, the formulation for finite and infinite-order LQR control designs are derived. The infinite-order control design for the beam is investigated, and a method of determining the feedback kernels needed to implement the control is shown. In Chapter 3, a control design for a reference example is done to show the ability to predict and verify the kernel predictions. In Chapter 4, experiments involving the derivation of the kernels and the control implementation through the use of PVDF area averaging sensors are performed. Two performance metrics are considered, and experimental closed-loop results are provided to verify that predicted performance is actually achieved. Problems with the implementation of the second performance metric motivate the work presented in Chapter 5, where an alternate control design using an array of rectangular-shaped area averaging sensors is investigated.

# Chapter 2

# Theory

## 2.1 OPTIMAL CONTROL BACKGROUND

The following formulations are for the finite and infinite-order Linear Quadratic Regulator (LQR) control designs for a cantilevered, Bernoulli-Euler beam. It is shown that the formulation of the infinite-order problem is similar in nature to the more familiar finite-order case, and that the desired feedback signal for the infinite-order case can be provided for by using area averaging sensors. The control law in the infinite-order case is described in terms of displacement kernels and displacement state functions. An equivalent form expressing the law in terms of curvature kernels and curvature state functions is derived. This is performed to make the feedback signal obtainable with PVDF area averaging sensors.

### 2.1.1 Finite-Order LQR Control Design

In designing a finite-order LQR controller for a cantilevered beam, the beam's structural behavior must first be characterized by some governing equation. It is standard practice to use a matrix differential equation of motion. The equation can be assembled using finite element methods [10]. The results lead to a finite-order matrix equation of the following form,

$$M_s \ddot{w} + C_s \dot{w} + K_s w = b_s f, \qquad (2.1)$$

where $M_s$, $C_s$, and $K_s$ are the mass, damping and stiffness matrices, respectively, and $w$ is the generalized displacement state vector. The states in this vector are the rotations and displacements at discrete points along the length of the structure. The term $bf$ describes the control action, accounting for how the actuators affect the motion of the modeled beam. The matrix equation can be reduced to a first-order, state-space form,

$$\dot{z} = Az + Bf, \qquad (2.2)$$

where

$$A = \begin{bmatrix} 0 & I \\ -M_s^{-1}K_s & -M_s^{-1}C_s \end{bmatrix} \qquad B = \begin{bmatrix} 0 \\ -M_s^{-1}b_s \end{bmatrix}, \qquad (2.3)$$

and the new state vector $z$ consists of the generalized displacement and displacement rate states. The finite-order LQR control design is applied to system models in the form shown in Equation 2.3.

The LQR control law is achieved through the minimization of the following quadratic performance index,

$$\Im = \lim_{\tau \to \infty} \left[ \frac{1}{\tau} \int_0^\tau \left( z^T Q z + f^T R f \right) \delta t \right], \qquad (2.4)$$

where $Q$ and $R$ are the state and control weighting matrices, respectively. The performance index $\Im$ is a minimum when a semi-positive definite solution $\Sigma$ to the following algebraic Riccati equation is found,

$$\Sigma A + A^T \Sigma + Q - \Sigma B R^{-1} B^T \Sigma = 0. \qquad (2.5)$$

The resulting feedback control law is represented by Equation 2.6.

$$f = -R^{-1}B^T \Sigma z = -\begin{bmatrix} G_d & G_{dr} \end{bmatrix} \begin{Bmatrix} w \\ \dot{w} \end{Bmatrix}. \qquad (2.6)$$

It is a linear combination of the generalized displacement and displacement rate states multiplied by feedback gains.

In applying the LQR control design, the designer can pick a particular performance output

$$y = Cz \qquad (2.7)$$

which she wishes to regulate, where $C$ is the matrix defining $y$ as a linear combination of the structural states. By letting

$$Q = C^T C \qquad (2.8)$$

in the performance index expression in Equation 2.4, the feedback signal derived from the minimization of the index is tailored to regulate the performance output $y$. The control weighting matrix $R$ is chosen based on the desired levels of authority on the actuators or combination of actuators. The stability of the modeled, closed-loop system is guaranteed if the system vibration modes are observable from the performance output $y$ and controllable from the forcing vector $f$ [8].

The finite-order LQR control design is not easy to implement on an infinite-order structure. The finite-order control design model is essentially a truncated approximation of the structure. The complexities that are introduced by using this truncated approximation could be compared to the example of

using a lower-order model to design a controller for a system with a larger but known finite number of states. An example system is given by Equation 2.9,

$$\dot{z} = \begin{Bmatrix} \dot{z}_p \\ \dot{z}_s \end{Bmatrix} = \begin{bmatrix} A_{pp} & A_{ps} \\ A_{sp} & A_{ss} \end{bmatrix} z + \begin{bmatrix} B_p \\ B_s \end{bmatrix} f \tag{2.9}$$

where the subscript $p$ denotes the modeled states and the subscript $s$ accounts for the remaining system dynamics. The modeled system is the truncated version of Equation 2.9, represented by

$$\dot{z}_p = A_{pp} z_p + B_p f. \tag{2.10}$$

The LQR feedback signal generated for the lower order model is

$$f = -G z_p, \tag{2.11}$$

where the term $G$ represents the LQR feedback gains generated for the lower order model. The modeled closed-loop system is

$$\dot{z}_p = \left( A_{pp} - B_p G \right) z_p, \tag{2.12}$$

where the closed-loop dynamics are determined from the eigenvalues of the matrix $A_{pp}$-$B_pG$.

The true closed-loop system would be

$$\dot{z} = \begin{bmatrix} A_{pp} - B_p G & A_{ps} \\ A_{sp} - B_s G & A_{ss} \end{bmatrix} z. \tag{2.13}$$

Its closed-loop dynamics would not be those guaranteed by the lower order design model represented in Equation 2.12. Even assuming that the open-loop companion matrix in Equation 2.9 possesses only stable poles, the presence of the

22

control spillover term $-B_sG$ in Equation 2.13 will alter the closed-loop system from its desired behavior and possibly even de-stabilize the system. The implementation of a finite-order LQR controller on an infinite-order structure poses the same control spillover problem, where the off-diagonal and lower diagonal terms of the companion matrix in Equation 2.9 would then represent the infinite number of unmodeled dynamics.

There are other problems with the application of the finite-order controller to the beam. First, increasing the number of states to increase the accuracy increases the complexity of the computation for the design. Secondly, the number of states in the model is directly related to the number of point sensor measurements needed to implement the control. The more states that are used, the more point sensors that are required. Thirdly, there are rotation states used in the present model represented by Equation 2.2, and they are not easily measured with point sensors. Applying the feedback control without the contributions from these states could amplify the control spillover problem.

As an alternative, the model in Equation 2.2 could be reduced in size with static condensation techniques, like the Guyan Reduction method [12]. Such techniques provide a reduced order control design model of the beam with errors that are less than those introduced by simply truncating the model. Unfortunately, these alternate methods also cause the original model in Equation 2.2 to be a less accurate approximation of the structure's physical behavior, further reducing the accuracy and achievable performance levels of the control design. Therefore, an LQR control design in an infinite-order framework is investigated to determine whether it is possible to avoid these problems.

### 2.1.2   Infinite-Order LQR Design

The approach and solution for an infinite-order LQR control design [9]

parallels the finite-order case. The beam's behavior is described by a continuous, partial differential equation of motion,

$$\rho A \frac{\delta^2}{\delta t^2}\omega(x,t) + c_s\frac{\delta}{\delta t}\omega(x,t) + EI\frac{\delta^4}{\delta x^4}\omega(x,t) \;=\; \tilde{f}(x,t), \qquad (2.14)$$

where $\omega$ is the spatially continuous displacement state function describing the transverse motion of the beam at any location or instant in time. The term $\rho A$ is the mass per unit length, $c_s$ is the damping per unit length, and $EI$ represents the beam's rigidity. The term $\tilde{f}$ is the distributed force per unit length acting on the beam. In the particular case for which the actuation is applied at a single point $x_o$, the forcing term can be modeled with a Dirac delta function [29]. The expression for $\tilde{f}$ becomes

$$\tilde{f}(x,t) \;=\; \partial(x - x_o)f(t), \qquad (2.15)$$

where $f$ is the force applied at $x_o$. The magnitude of the Dirac delta function is in units of inverse length. It is also advantageous, as it was in the finite-order case, to reduce the expression in Equation 2.14 to a first order, state-space form,

$$\frac{\delta}{\delta t}\zeta(x,t) \;=\; a(x)\zeta(x,t) + b(x)f(t), \qquad (2.16a)$$

or more explicitly,

$$\frac{\delta}{\delta t}\left\{\begin{array}{c}\omega(x,t)\\[4pt]\frac{\delta}{\delta t}\omega(x,t)\end{array}\right\} \;=\; \left[\begin{array}{cc} 0 & 1 \\[6pt] -\dfrac{EI}{\rho A}\dfrac{\delta^4}{\delta x^4} & -\dfrac{c_s}{\rho A} \end{array}\right]\left\{\begin{array}{c}\omega(x,t)\\[4pt]\frac{\delta}{\delta t}\omega(x,t)\end{array}\right\} + \left[\begin{array}{c} 0 \\[6pt] \dfrac{\partial(x - x_o)}{\rho A} \end{array}\right]f(t), \qquad (2.16b)$$

where the differential operators $a$ and $b$ are shown in their matrix form. The vector $\zeta$ contains the continuous displacement and displacement rate state

functions. The infinite-order LQR control design is applied to the form of Equation 2.16.

The infinite-order LQR performance index

$$\Im \;=\; \lim_{\tau \to \infty}\left[\frac{1}{\tau}\int_0^{\tau}\int_0^{L}(\langle q\zeta,\zeta\rangle + \langle rf,f\rangle)\delta x\,\delta t\right] \tag{2.17}$$

is a minimum when the differential operator $\sigma$ in the following functional Riccati equation is found,

$$\sigma a\zeta + \bar{a}\sigma\zeta + q\zeta - \sigma br^{-1}\bar{b}\sigma\zeta \;=\; 0. \tag{2.18}$$

The bars above the differential operators $a$ and $b$ denote the adjoint functions. The resulting form of the infinite-order control law for the structure is

$$f(t) \;=\; -r^{-1}\bar{b}\sigma(x)*\zeta(x,t)$$

$$=\; -\frac{1}{r}\left[0 \quad \frac{\partial(x-x_o)}{\rho A}\right]\int_0^{L}\begin{bmatrix}\sigma_{11}(x-v) & \sigma_{12}(x-v)\\ \sigma_{21}(x-v) & \sigma_{22}(x-v)\end{bmatrix}\left\{\begin{array}{c}\omega(v,t)\\ \dfrac{\delta}{\delta t}\omega(v,t)\end{array}\right\}\delta v$$

$$=\; -\partial(x-x_o)\left[0 \quad \frac{1}{\rho A r}\right]\int_0^{L}\begin{bmatrix}\sigma_{11}(x-v) & \sigma_{12}(x-v)\\ \sigma_{21}(x-v) & \sigma_{22}(x-v)\end{bmatrix}\left\{\begin{array}{c}\omega(v,t)\\ \dfrac{\delta}{\delta t}\omega(v,t)\end{array}\right\}\delta v$$

$$=\; \partial(x-x_o)g(x,t)$$

$$=\; -\partial(x-x_o)\int_0^{L}\begin{bmatrix}\kappa_d(x-v) & \kappa_{dr}(x-v)\end{bmatrix}\left\{\begin{array}{c}\omega(v,t)\\ \dfrac{\delta}{\delta t}\omega(v,t)\end{array}\right\}\delta v, \tag{2.19}$$

25

where $\kappa_d$ and $\kappa_{dr}$ are the spatially distributed feedback kernels [7]. The form of Equation 2.19 is that of the convolution rule [13].

The presence of the Dirac delta function in Equation 2.19 defines the expression as a scaled impulse at $x_o$. The symbol $\partial(x - x_o)$ is not actually a function as its name suggests; it is an operation. The definition of the symbol specifies the operation

$$\int_0^L \partial(x - x_o)\ldots\delta x \tag{2.20}$$

which, when applied to a continuous function $g(x,t)$, sifts out or selects the value $g(x_o,t)$ of this function at the spatial point $x_o$. This definition can be exploited to obtain a more refined expression for the feedback force. By dividing Equation 2.19 by $L$ and integrating it over the length of the beam, the feedback force $f$ applied at $x_o$ becomes

$$\frac{1}{L}\int_0^L f(t)\delta x \;=\; \frac{1}{L}f(t)L \;=\; f(t)$$

$$=\; \frac{1}{L}\int_0^L \partial(x - x_o)g(x,t)\delta x \;=\; \frac{1}{L}g(x_o,t)$$

$$=\; \frac{1}{L}\int_0^L \left\{ \left[ -\partial(x - x_o) \right] \int_0^L \left[ \kappa_d(x - v) \quad \kappa_{dr}(x - v) \right] \left\{ \begin{array}{c} \omega(v,t) \\ \dfrac{\delta}{\delta t}\omega(v,t) \end{array} \right\} \delta v \right\} \delta x$$

$$=\; \frac{1}{L}\left\{ -\int_0^L \kappa_d(x_o - v)\omega(v,t)\delta v \;-\int_0^L \kappa_{dr}(x_o - v)\frac{\delta}{\delta t}\omega(v,t)\delta v \right\}. \tag{2.21}$$

26

By exchanging the length variable $x$ for $v$, the control law can be rewritten as

$$f(t)_{x_o} = -\int_0^L K_d(x_o - x)\omega(x,t)\delta x - \int_0^L K_{dr}(x_o - x)\frac{\delta}{\delta t}\omega(x,t)\delta x$$

$$= -\int_0^L K_d(x)\omega(x,t)\delta x - \int_0^L K_{dr}(x)\frac{\delta}{\delta t}\omega(x,t)\delta x, \qquad (2.22)$$

where $K_d$ and $K_{dr}$ are the displacement and displacement rate feedback kernels, respectively.

This is a profound, but not yet useful result. The implementation of the displacement and displacement rate feedback kernels requires the use of continuously distributed displacement and displacement rate sensors. The type of distributed sensors currently available are the PVDF area averaging sensors. These sensors measure the continuous curvature and curvature rate state functions of the beam. Fortunately, the measurement of the displacement and curvature state functions are related. The relation makes it possible to use the output of PVDF area averaging sensors to obtain the infinite-order LQR feedback command signal.

### 2.1.3 Providing the Feedback with PVDF Area Averaging Sensors

This subsection relates the displacement kernels to an associated pair of curvature kernels. The LQR feedback control signal represented by Equation 2.22 is re-expressed in terms of the curvature kernels, showing that it can be measured by a pair of distributed curvature sensors. The voltage output of the PVDF area averaging sensors is defined to show that they can provide a distributed measurement of the curvature along the length of the beam, and that a pair of the sensors can provide the needed feedback signal.

PVDF area averaging sensors actually measure the surface strain, and for

27

a simple Bernoulli-Euler beam, the surface strain $\varepsilon$ is defined as

$$\varepsilon(x,t)_{\frac{h}{2}} = \frac{h}{2}\frac{\delta^2}{\delta x^2}\omega(x,t), \tag{2.23}$$

which is the curvature times the distance $h/2$ from the beam's neutral axis to its surface. The voltage signal from a PVDF area averaging sensor attached to the surface of the beam is expressed in terms of the surface strain, and is given by

$$V(t) = \frac{e_{31}}{C_f}\int_0^L F(x)\varepsilon(x,t)\delta x, \tag{2.24}$$

where $C_f$ is the sensor capacitance, $e_{31}$ is the piezoelectric field intensity constant, and $F$ is the spatial weighting etched on the electrode.

The form of Equation 2.24 is beneficial. It shows that the control can be implemented with these sensors if there is a way of expressing the control law in terms of *curvature* kernels and *curvature* state functions. It is possible to do this for a cantilevered beam structure. The displacement kernels from Equation 2.22 can be directly related to an associated set of curvature kernels. The relationship transforms the feedback form in Equation 2.22 into an equivalent feedback of curvature state functions along with point measurements. The point measurements enable the ability to retain rigid body control.

The infinite-order LQR control law is transformed in this manner by employing two simple mathematical operations. The first operation involves introducing some formal definitions for the structure of the curvature kernels. The second operation is integration by parts which, when used in conjunction with the first, re-interprets the law as desired.

The process begins with defining the desired structure for the curvature kernels. Using the first Fundamental Theorem of Calculus [30], the displacement

kernel $K_d$ can be expressed as

$$K_d(x) = \frac{\delta}{\delta x}\int_a^x K_d(\varsigma)\delta\varsigma. \tag{2.25}$$

It is chosen that the integral expression in Equation 2.25 be defined as

$$\int_a^x K_d(\varsigma)\delta\varsigma = K_r(x) = \hat{K}_r(x) - \hat{K}_r(a), \tag{2.26}$$

where $K_r$ is defined as the rotation kernel. A similar definition is made for the expression $K_r$, where

$$K_r(x) = \frac{\delta}{\delta x}\int_a^x K_r(\xi)\delta\xi = \frac{\delta}{\delta x}K_c(x) = \frac{\delta}{\delta x}(\hat{K}_c(x) - \hat{K}_c(a)). \tag{2.27}$$

In this equation, $K_c$ is defined as the curvature kernel. The above definitions are valid as long as the kernels are continuous over the domain including the lower limit of the integral $a$ [30]. In the statement of the fundamental theorem, the choice of $a$ is arbitrary, but it is advantageous to choose $a$ to be equivalent to the beam length $L$ for the following formulations. The advantage to this is revealed shortly.

Using the above definitions for $K_r$, $K_c$, and $a$, the second operation of integrating by parts is performed. Doing this to the first part of Equation 2.22 yields

$$f_d(t)_{x_o} = -\int_0^L K_d(x)\omega(x,t)\delta x$$

$$= -\{\omega(x,t)K_r(x)\}\Big|_0^L + \int_0^L K_r(x)\frac{\delta}{\delta x}\omega(x,t)\delta x$$

$$= -\left\{\omega(x,t)K_r(x)\right\}\Big|_0^L + \left\{\frac{\delta}{\delta x}\omega(x,t)K_c(x)\right\}\Big|_0^L$$

$$- \int_0^L K_c(x)\frac{\delta^2}{\delta x^2}\omega(x,t)\delta x. \tag{2.28}$$

This expression can be simplified since, by the established kernel definitions, $K_r$ and $K_c$ have been circumscribed to be zero at $x$ equal to $L$. Applying these conditions gives

$$f_d(t)_{x_o} = \left\{\omega(x,t)K_r(x) - \frac{\delta}{\delta x}\omega(x,t)K_c(x)\right\}\Big|_0 - \int_0^L K_c(x)\frac{\delta^2}{\delta x^2}\omega(x,t)\delta x. \tag{2.29}$$

Equation 2.29 re-expresses the first part of the control law in Equation 2.22 as the convolution of a curvature kernel with the curvature state function of the beam plus point measurements of the rotation and displacement at the root. The simplicity of the expression is based on the choice of the lower limit value $a$ in the kernel definitions. It is important to note that changing the value of $a$ wouldn't change the above calculations on any basic level. Doing so would just express $f_d$ in terms of *other* kernel functions that are non-zero at $x$ equal to $L$. There is, however, a disadvantage in using other kernel functions: two additional point measurements at the tip are needed to provide the feedback. The choice of $a$ equal to $L$ makes the result in Equation 2.29 simpler and more analogous to the PVDF sensor outputs.

Equation 2.29 can be reduced even further for a cantilevered beam. The point measurements at the root are conveniently zero, as specified by the geometric boundary conditions. Performing a similar sequence of operations for the second half of Equation 2.22 yields an alternate form of the infinite-order LQR control law,

$$f(t)_{x_o} = -\int_0^L K_c(x)\frac{\delta^2}{\delta x^2}\omega(x,t)\delta x - \int_0^L K_{cr}(x)\frac{\delta^3}{\delta t\delta x^2}\omega(x,t)\delta x, \qquad (2.30)$$

expressed in terms of curvature and curvature rate feedback kernels $K_c$ and $K_{cr}$, as desired. The explicit relationship between $K_c$ and $K_d$ has been defined as

$$K_c(x) = \int_L\int_L K_d(\varsigma)\delta\varsigma\,\delta\xi, \qquad (2.31a)$$

and the one between $K_{cr}$ and $K_{dr}$ is

$$K_{cr}(x) = \int_L\int_L K_{dr}(\varsigma)\delta\varsigma\,\delta\xi. \qquad (2.31b)$$

The definitions for the curvature and curvature rate kernels are convenient mathematically, and they also make sense physically. For a Bernoulli-Euler beam, the curvature is defined to be zero at the unconstrained end. Along with the two geometric boundary conditions, the beam dynamics represented by a fourth-order equation require two more boundary conditions to provide a unique solution. One of these boundary conditions requires a zero transverse bending moment at $x$ equal to $L$, and this bending moment is directly proportional to the curvature. Physically, there is no curvature at the free end to apply any spatial weighting to. It is hypothesized that any formulation using kernels that are non-zero at $x$ equal to $L$ would still be equivalent. It is possible in such cases that the additional point measurements required at the beam tip compensate for the effects introduced by the other types of kernels.

In contrast to Equation 2.22, the statement in Equation 2.30 is a profound and useful result. A pair of area averaging sensors could be used to obtain this type of feedback signal by directly relating the etched spatial weightings on the

sensor electrodes to the shapes of the curvature feedback kernels. This would reduce the full state feedback expression into the linear combination of two sensor outputs multiplied by gains $G_1$ and $G_2$, expressed by

$$f(t)_{x_o} = -G_1 \frac{e_{31}h}{2C_f} \int_0^L F_{sensor1}(x) \frac{\delta^2}{\delta x^2} \omega(x,t)\delta x$$

$$- G_2 \frac{e_{31}h}{2C_f} \frac{\delta}{\delta t} \int_0^L F_{sensor2}(x) \frac{\delta}{\delta x^2} \omega(x,t)\delta x. \qquad (2.32)$$

The gains are used to provide the proper sensitivity scaling. For example, the gain $G_1$ is determined by the expression

$$G_1 = \frac{K_c(x)}{\frac{e_{31}h}{2C_f} F_{sensor1}(x)}, \qquad (2.33)$$

where the electrode shape represented by the term $F_{sensor\,1}$ is chosen to be identical in shape to the curvature kernel $K_c$.

What is needed to progress further is a method of *determining* the kernels. It is not possible to solve directly for the kernels in the infinite-order model expressions shown above. It is possible, however, to solve for the LQR feedback gains for any controllable, observable finite-order model in state-space form. The parallelism that exists between the finite-order and infinite-order LQR formulations can be exploited to use the feedback gains to solve for the kernels.

### 2.1.4   Existence of a Solution for the Kernels

The linear combination of states and feedback gains in the finite-order control law is related to the integral expressions in the infinite-order case. As the

32

number of states increases, the linear combination, or summation, approaches a continuous integral over the length of the structure in the limit. The integral achieved in the limit is exactly equivalent to the infinite-order expression shown in Equation 2.22. The reverse is also possible. Using the available finite element approximation techniques, the integral expression of the infinite-order control law can be discretized. It can be approximated in terms of a finite number of generalized states. With some finesse, this discretized form can be related to a finite-order control law determined from a model with the same number of states. Doing so yields an estimate of the displacement kernels $K_d$ and $K_{dr}$.

The whole kernel estimation process is essentially a transformation of the LQR displacement and displacement rate feedback gains. The gains are transformed into a pair of kernel estimates $K_d$ and $K_{dr}$. The displacement kernel estimates are then integrated numerically to produce the curvature kernel estimates $K_c$ and $K_{cr}$. This is done since it is the curvature kernels that are used in the implementation. The accuracy of the kernel estimates is a function of the order of the control design model used to determine the feedback gains.

Some properties of the curvature kernel estimates actually vary with model order, like the shape and magnitude. Fortunately, the varying properties are convergent. By increasing the fidelity of the finite-order model, better estimates of the kernels $K_c$ and $K_{cr}$ can be made. The best *estimates* would be determined from the largest, most accurate finite-order model the control designer's computer could generate. However, a sufficiently large enough model needed to produce an accurate, implementable estimate of the curvature kernels may not be available.

A more vigorous approach is to use a *set* of finite-order models. Each individual model in the set contains invaluable information about the convergence rate of the curvature kernel estimates. By using the set of models

together, the rates of change of the kernel shapes and magnitudes can be determined. Knowledge of the rates of change over a sufficient domain of model orders allows for the *true* infinite-order values of the kernel shapes and magnitudes to be found. The only restrictions on the finite-order models is that they employ only physical states to describe the beam. This makes models generated from finite element methods an ideal choice for such a procedure.

## 2.2 KERNEL DERIVATION TECHNIQUE

The path to achieving the true infinite-order curvature kernels is as follows: a finite element model of the infinite-order beam is derived. An LQR performance index is specified, and the generalized displacement and displacement rate feedback gains are determined using standard Riccati solvers. In parallel to these operations, the continuous expression of the infinite-order control law in Equation 2.22 is discretized in a fashion similar to finite element methods. Performing the discretization interprets the two displacement kernels $K_d$ and $K_{dr}$ in terms of two unknown kernel coefficient vectors. The discretized form of the infinite-order control law possesses a configuration similar to the finite-order LQR control law in Equation 2.6, which is expressed in terms of the feedback gains. Since the feedback gains are known, a direct solution of the unknown kernel coefficient vectors can be found by equating the two relations. The displacement and displacement rate kernel estimates are determined with the coefficient vectors, and then integrated numerically to yield the curvature and curvature rate kernel estimates $K_c$ and $K_{cr}$. The curvature and curvature rate kernel estimates are then decomposed into a linear combination of a finite number of curvature mode shapes multiplied by weighting coefficients.

34

The weighting coefficients represent the important information achieved in all these operations. By performing these operations for a number of models, the changes in the weighting coefficients from model to model can be observed. The curvature mode shapes are used in this manner mainly for convenience. Observing the variations in the weighting coefficients is an easy way of characterizing the changes in shape and magnitude of the kernels. It also puts the needed feedback in a useful perspective. The amount that a particular mode shape contributes to the feedback kernel shapes corresponds to the level that the vibration associated with that mode is penalized in achieving the desired closed-loop performance.

The observed behavior of the each weighting coefficients reveals the decay rate of that particular mode contribution to the kernel shapes. As the model order increases, the change in the value of the weighting coefficients decreases. In fact, the plot of each coefficient versus the model order resembles a decaying exponential function. The information in each plot can be modeled, and each model can be evaluated at infinity to determine the infinite-order contribution of that mode to the kernel shapes. Then all the infinite-order contributions can be used to assemble the infinite-order kernel predictions.

The two following subsections put the above 'road-map' of the Kernel Derivation Technique into mathematical expressions. The first subsection shows how estimates of the displacement and displacement rate kernels are made by discretizing the infinite-order control law. The second subsection shows how the curvature and curvature rate kernels are determined, and how they are decomposed into a linear combination of curvature mode shape vectors multiplied by weighting coefficients. It also explains the form of modeling of the weighting coefficient behavior that produces the infinite-order curvature and curvature rate kernel predictions.

35

## 2.2.1 Kernel Derivation Technique: Solving for Displacement and Displacement Rate Kernels

Estimates of the displacement and displacement rate kernels are made by discretizing the infinite-order control law. The continuous integral expression in Equation 2.22 is reinterpreted as a summation of integrals over $N$ smaller intervals, or elements, of the beam. Doing so involves no estimation, but is simply an alternate way of expressing the integral over its domain. The equation form of this is given by

$$f(t)_{x_o} = \left\{ f_d(t) + f_{dr}(t) \right\}\Big|_{x_o} = \left\{ \sum_i^N f_d{}^i(t) + \sum_i^N f_{dr}{}^i(t) \right\}\Big|_{x_o} \qquad (2.34)$$

where $f_d$ and $f_{dr}$ are the contributions to the control action from the displacement and displacement rate state functions, respectively. The superscript $i$ denotes the contributions from the different elements. Specifying the terms in the summation, the control law is expressed as

$$f(t)_{x_o} = \sum_i^N \int_{l_{i-1}}^{l_i} K_d^i(x)\omega(x,t)\delta x + \sum_i^N \int_{l_{i-1}}^{l_i} K_{dr}^i(x)\frac{\delta}{\delta t}\omega(x,t)\delta x \qquad (2.35)$$

where $K_d^i$ and $K_{dr}^i$ are segments of the displacement and displacement rate kernel functions over each element $i$.

The segments of the kernels and the state functions are then approximated with some simple cubic spline relations. The state functions are approximated to be a linear combination of the finite element interpolation functions [10] and the generalized states of that element. The approximation is represented by the following equation form,

36

$$f_d(t) = \sum_{i=1}^{N} \int_{l_{i-1}}^{l_i} K_d^i(x)\,\omega(x,t)\,\delta x$$

$K_d(x)$

$\omega(x,t)$

$l_0 = 0$      $l_N = L$

$$f_d^i(t) = \int_{l_{i-1}}^{l_i} K_d^i(x)\,\omega(x,t)\,\delta x$$

$K_d(x)$

displacement kernel
segment $K_d^i(x)$

$\omega(x,t)$

$l_0 = 0$      $l_{i-1}$    $l_i$      $l_N = L$
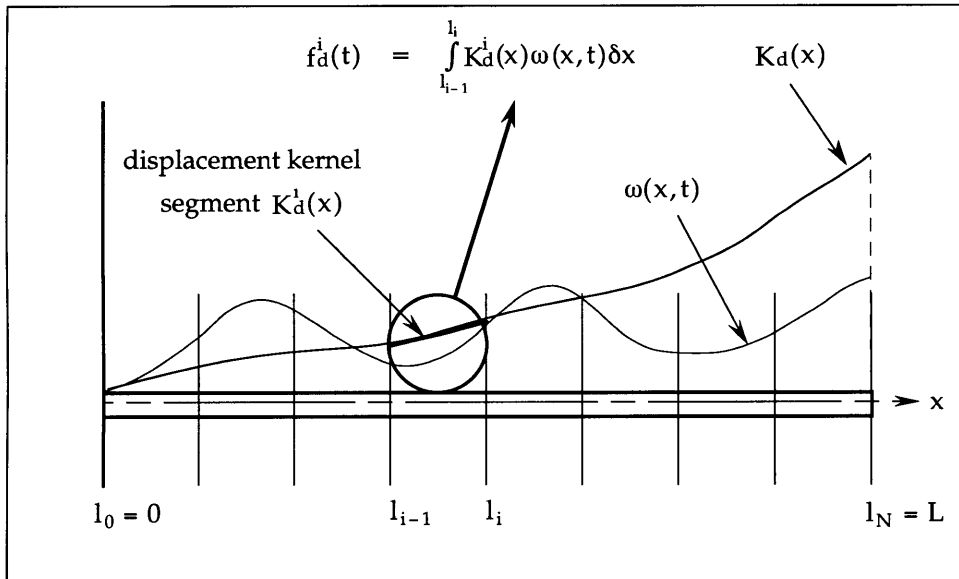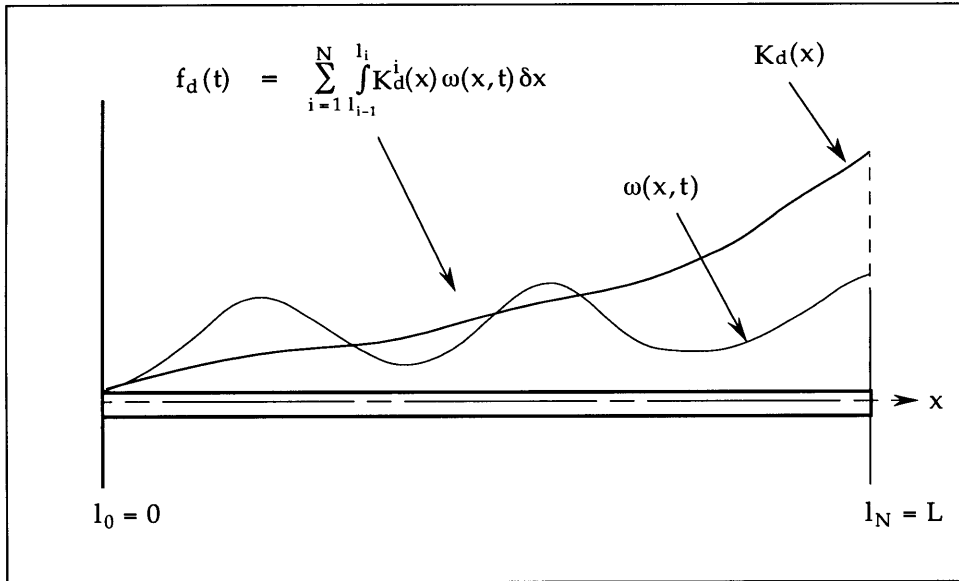
**Figure 2.1:** Graphical representation of integration of displacement kernel segment $K_d^i$ with state function over an interval $i$.

37

$$\omega(x,t) \cong P(x)w_i(t), \qquad l_{i-1} \geq x \geq l_i,$$

$$P(x) = \left[1 - \frac{3x^2}{l_e^2} + \frac{2x^3}{l_e^3} \quad x - \frac{2x^2}{l_e} + \frac{x^3}{l_e^2} \quad \frac{3x^2}{l_e^2} - \frac{2x^3}{l_e^3} \quad -\frac{x^2}{l_e} + \frac{x^3}{l_e^2}\right]$$

$$w_i(t) = \left\{\omega(l_{i-1},t) \quad \frac{\delta}{\delta x}\omega(l_{i-1},t) \quad \omega(l_i,t) \quad \frac{\delta}{\delta x}\omega(l_i,t)\right\}^T \qquad (2.36)$$

where $P$ is the interpolation function matrix for a Bernoulli-Euler beam, and $w_i$ is the generalized displacement state vector for the element $i$. The term $l_e$ is the element length. The displacement rate state function is estimated in a similar manner.

The approximation for the displacement kernels expresses each segment $K_d^i$ in terms of four unknown coefficients. The approximation for the segment is represented by the following equation form,

$$K_d^i(x) \cong \alpha_i\beta(x) = a_i + b_i x + c_i x^2 + d_i x^3,$$

$$\alpha_i = \left\{a_i \quad b_i \quad c_i \quad d_i\right\},$$

$$\beta(x) = \begin{bmatrix} 1 & x & x^2 & x^3 \end{bmatrix}^T, \qquad (2.37)$$

where $a_i$, $b_i$, $c_i$, and $d_i$ are the unknown coefficients defining the kernel segment for element $i$. The approximation of the displacement rate kernel segments are defined in a similar manner.

Using these approximations, Equation 2.35 becomes

$$f(t)_{x_0} \cong \sum_i^N \alpha_i \left(\int_{l_{i-1}}^{l_i}\beta(x)P(x)\delta x\right)w_i(t) + \sum_i^N \gamma_i \left(\int_{l_{i-1}}^{l_i}\beta(x)P(x)\delta x\right)\dot{w}_i(t)$$

$$\cong \sum_i^N \alpha_i m w_i(t) + \sum_i^N \gamma_i m \dot{w}_i(t). \qquad (2.38)$$

38

The interpolation function matrix $P$ and the matrix $\beta$ are known, such that the integrals can be solved explicitly, generating the element matrix $m$. The solution for $m$ is

$$m = \begin{bmatrix} \dfrac{l_e}{2} & \dfrac{l_e^2}{12} & \dfrac{l_e}{2} & -\dfrac{l_e^2}{12} \\[2mm] \dfrac{31 l_e^2}{20} & \dfrac{l_e^3}{30} & \dfrac{71 l_e^2}{20} & -\dfrac{l_e^3}{20} \\[2mm] \dfrac{l_e^3}{15} & \dfrac{l_e^4}{60} & \dfrac{41 l_e^2}{15} & -\dfrac{l_e^4}{30} \\[2mm] \dfrac{l_e^4}{28} & \dfrac{l_e^5}{105} & \dfrac{31 l_e^2}{14} & -\dfrac{l_e^5}{42} \end{bmatrix}. \tag{2.39}$$

By re-expressing the summations in Equation 2.38 into a global matrix form, the following equation is found,

$$\sum_i^N f_d{}^i(t) + \sum_i^N f_{dr}{}^i(t) \cong -\begin{bmatrix} \alpha^T M & \gamma^T M \end{bmatrix} \begin{Bmatrix} w \\ \dot{w} \end{Bmatrix} \tag{2.40}$$

expressing a discrete form of the infinite-order LQR control law in terms of a finite number of states [7]. The terms $\alpha$ and $\gamma$ are the unknown kernel coefficient vectors. They contain the coefficients for the cubic splines describing the displacement and displacement rate kernels $K_d$ and $K_{dr}$. The global matrix $M$ is assembled from linear combinations of the element matrix $m$. This discrete form is related to a control law for a finite-order model with the same number of states (represented by Equation 2.6) to solve for $\alpha$ and $\gamma$.

For a unique solution of the kernel coefficient vectors $\alpha$ and $\gamma$ to be found, two sets of constraints need to be included. The first set of constraints are on the slope and magnitude of the kernels between the elements. The continuity of the kernels is enforced by requiring the slope and magnitude to be continuous along

39

the beam length. The continuity requirements come from the application of the first Fundamental Theorem of Calculus in Subsection 2.1.3, which is used to define the structure of the curvature kernels. The constraints for the displacement kernel, applied between each pair of adjacent elements, are represented in equation form by

$$a_{i+1} = a_i + b_i l_e + c_i l_e^2 + d_i l_e^3$$

$$b_{i+1} = b_i + 2 c_i l_e + 3 d_i l_e^2$$

$$\begin{bmatrix} 0 & 0 \end{bmatrix} = \begin{bmatrix} a_i & b_i & c_i & d_i & a_{i+1} & b_{i+1} & c_{i+1} & d_{i+1} \end{bmatrix} \begin{bmatrix} 1 & 0 \\ l_e & 1 \\ l_e^2 & 2 l_e \\ l_e^3 & 3 l_e^2 \\ -1 & 0 \\ 0 & -1 \\ 0 & 0 \\ 0 & 0 \end{bmatrix}$$

$$= \begin{bmatrix} \alpha_i^T & \alpha_{i+1}^T \end{bmatrix} \begin{bmatrix} s \end{bmatrix}, \tag{2.41}$$

where $s$ is the inter-element constraint matrix. The constraints for the displacement rate kernel are defined in a similar manner. The other set of constraints are geometric boundary conditions for the beam. They are described by Equation 2.42.

$$\begin{bmatrix} 0 \\ 0 \end{bmatrix} = \begin{bmatrix} 1 & 0 & 0 & 0 \\ 0 & 1 & 0 & 0 \end{bmatrix} \left\{ \omega(0,t) \quad \frac{\delta}{\delta x} \omega(0,t) \quad \omega(l_1,t) \quad \frac{\delta}{\delta x} \omega(l_1,t) \right\}^T$$

$$= \begin{bmatrix} u \end{bmatrix} w_i(t). \tag{2.42}$$

The term $u$ describes the geometric boundary constraint matrix. Using the above

Equations 2.40 through 2.42, the feedback gains $G_d$ and $G_{dr}$ can be related to the unknown coefficient vectors $\alpha$ and $\gamma$. The relation is given by

$$
\text{Tc} = \begin{bmatrix} T_d & 0 \\ 0 & T_{dr} \end{bmatrix} \begin{Bmatrix} \alpha \\ \gamma \end{Bmatrix} = g = \begin{Bmatrix} \begin{Bmatrix} G_d^T \\ 0 \end{Bmatrix} \\ \begin{Bmatrix} G_{dr}^T \\ 0 \end{Bmatrix} \end{Bmatrix}.
\qquad (2.43)
$$

The global matrix $T$ is assembled from the matrices $M$, $s$, and $u$. It is square and invertible, such that a unique solution for the coefficient vectors $\alpha$ and $\gamma$ is found. The vectors are then used to generate estimates of the displacement kernels for that model order.

### 2.2.2  Kernel Derivation Technique: Solving for Curvature and Curvature Rate Kernels

The displacement kernel estimates are integrated twice to produce curvature kernel estimates. The curvature kernel estimates are then decomposed into a number of curvature mode shape vectors. The curvature mode shapes for a Bernoulli-Euler beam [22] are described by the following functions,

$$
\varphi_r(x) = -\lambda_r^2 \left[ (\sin\lambda_r x + \sinh\lambda_r x) + \frac{(\cos\lambda_r L + \cosh\lambda_r L)}{(\sin\lambda_r L - \sinh\lambda_r L)}(\cos\lambda_r x + \cosh\lambda_r x) \right].
$$

$$
(2.44)
$$

The subscript $r$ in Equation 2.44 denotes the mode number. By using a finite number of these functions, a matrix of the form

$$
\Psi = \begin{bmatrix} \varphi_1(x) & \varphi_2(x) & \cdots \cdots & \varphi_{n-1}(x) & \varphi_n(x) \end{bmatrix}
\qquad (2.45)
$$

can be assembled. The curvature mode shape functions form the vector columns

41

of $\Psi$. Each row of $\Psi$ contains the values of the mode shapes at a particular point. Using a matrix of this form, the curvature kernel estimates for each model order are decomposed into a weighted sum of the mode shape vectors, represented by

$$K_c^j = \sum_{r=1}^{n} \varphi_r c_{c_r}^j = \Psi c_c^j \qquad (2.46a)$$

and

$$K_{cr}^j = \sum_{r=1}^{n} \varphi_r c_{cr_r}^j = \Psi c_{cr}^j, \qquad (2.46b)$$

where $K_c^j$ and $K_{cr}^j$ are the curvature and curvature rate kernel estimates. The superscript $j$ in the above equation denotes the different size models. The vectors $c_c^j$ and $c_{cr}^j$ contain the weighting coefficients for the curvature and curvature rate kernels, respectively. The weighting coefficients characterize the contribution of each mode to a kernel. The coefficients are found by performing a least-squares fit of the columns of the matrix $\Psi$ onto the kernel function vectors. The equations for the procedure are

$$c_c^j \cong \left( \Psi^T \Psi \right)^{-1} \Psi^T K_c^j \qquad (2.47a)$$

and

$$c_c^j \cong \left( \Psi^T \Psi \right)^{-1} \Psi^T K_c^j. \qquad (2.47b)$$

Given a kernel vector with $p$ points, the dimensions of $\Psi$ must be $p$ by $n$. The calculations are made for a set of finite-order models, and the individual weighting coefficients of the vectors $c_c^j$ and $c_{cr}^j$ are observed as a function of increasing model order.

42

The weighting coefficients are modeled as exponentially decaying functions of model order. The models of the weighting coefficients are essentially curve fits. They are observed in the limit as the model order goes to infinity. The final value of each weighting coefficient model yields the infinite-order mode shape contribution for that mode. The final values are used together to construct the infinite-order kernel predictions.

# Chapter 3

# Reference Example

This chapter concentrates on validating the techniques used to find the infinite-order curvature kernels. An approach to verifying the kernels is presented. A Linear Quadratic Regulator (LQR) control design is derived for a reference cantilevered beam influenced by a dynamic tip force. The associated curvature kernels are predicted. Properties about the kernels are discussed, relating them to the control objective. A verification model is used show that the pair of distributed curvature kernel sensors can provide the needed feedback.

## 3.1 VALIDATING THE KERNEL PREDICTIONS: APPROACH

Figure 3.1 shows a uniform, cantilevered beam subjected to a dynamic tip force. In formulating an LQR control design for such a structure, the desired performance index must be specified. The index describes a specified performance output and the desired control authority for the design. In evaluating the design, it is important to observe the performance output transfer function for open and closed-loop conditions. The performance output transfer function is the transmission from the specified performance output to the force acting on the structure. The open and closed-loop measurements can be compared to show the effectiveness of the control design.
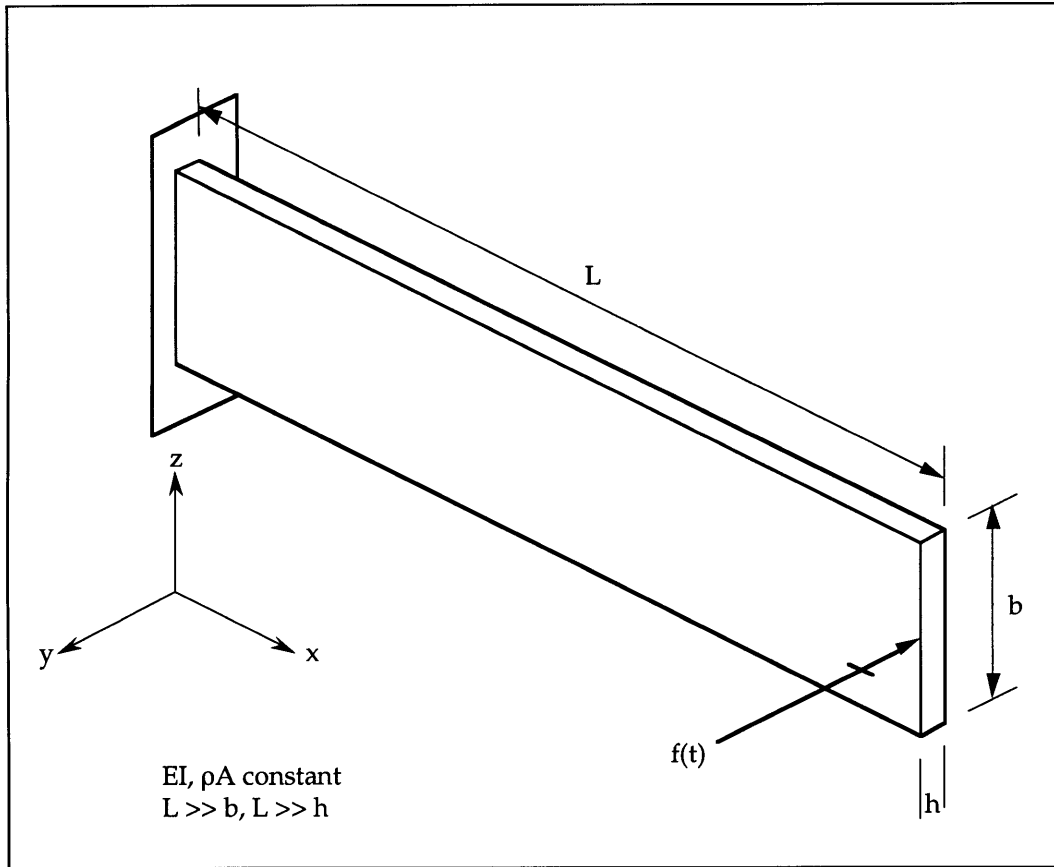
**Figure 3.1:** Illustration of a uniform, cantilevered Bernoulli-Euler beam subjected to a dynamic tip force $f$.

Another important transfer function to the control design is the loop transfer function (LTF). The LTF is defined as the transmission from the LQR feedback force to the tip force, and is illustrated in the block diagram of Figure 3.2. The feedback force represents a filtered measurement of the structural motion, used to react against disturbances. When a disturbance sets the structure into motion, the feedback force works to reduce that motion. Because of this, it is very important for the feedback force to have the correct phase relative to any induced motion of the structure. The incorrect phase would cause the system to be unstable, with the feedback force to amplifying the motion of the beam instead of reducing it. The relative phase of the feedback force to the induced
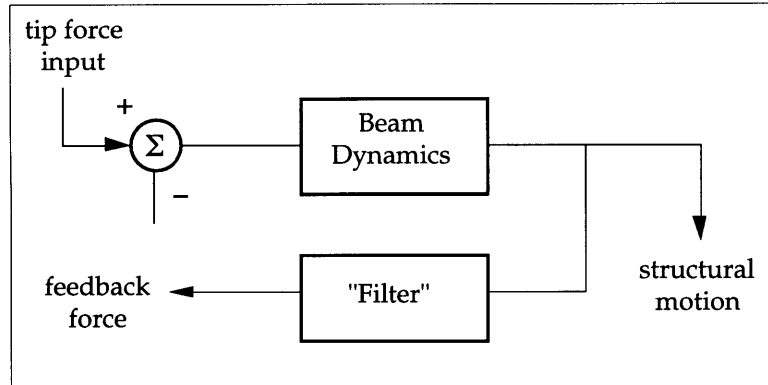
**Figure 3.2:**   General block diagram, illustrating the LTF.

motion of the structure is represented by the phase of the LTF. For an LQR control design, the LTF is guaranteed to have the correct phase to provide stability.

The feedback force can also be biased to respond against certain types of motion, represented by the mode shapes of the beam. The response to the different modes may vary, and the relative magnitude of the feedback force to these induced motions is represented by the magnitude of the LTF. For an LQR control design, the relative magnitude the feedback force has and the frequency range of modes for which it is effective at reducing vibrations are a function of the control weighting in the control design performance index. The smaller the control weighting, the larger the relative magnitude. For the beam, a common pattern for a single-input-single-output LTF generated from an LQR control design is to have an alternating pole-zero pattern. The pattern allows the LTF to provide the desired large relative magnitudes to certain modes while maintaining the proper relative phase to insure stability. These are among a few of the interesting properties of the LTF for an LQR control design [8]. In summary, the LTF captures enough information about the control design that it can serve as an evaluation tool.

Using a high fidelity, finite-order model of the beam, the LTF for an LQR control design can be determined fairly accurately. The determination of the LTF in this manner is represented by

$$H_{LTF}(j\varpi) = \begin{bmatrix} G_d & G_{dr} \end{bmatrix}(j\varpi I - A)^{-1}B \tag{3.1}$$

where $G_d$ and $G_{dr}$ are the LQR feedback gain matrices for the generalized displacement and displacement rate states, respectively. The matrices $A$ and $B$ are the companion and control transmission matrices for the finite-order model.

The LTF can also be determined from the infinite-order kernel predictions associated with the LQR control design. The associated kernels can be determined with the Kernel Derivation Technique outlined in Chapter 2. The determination of the LTF from the kernels is represented by

$$H_{LTF}(j\varpi) = \int_0^L \begin{bmatrix} K_c(x) & K_{cr}(x) \end{bmatrix}\frac{\delta}{\delta x}(j\varpi - a(x))^{-1}b(x)\delta x \tag{3.2}$$

where $K_c$ and $K_{cr}$ are the curvature and curvature rate kernels. The terms $a$ and $b$ are the infinite-order companion and control transmission matrices. For the kernel predictions to be valid, the LTF determined from the kernels must match the LTF determined from a high fidelity, finite-order model of the beam. The transfer function in Equation 3.1 can be generated very easily using finite-element methods. There is also a way to determine the transfer function in Equation 3.2. The approach is to essentially numerically integrate the expression in Equation 3.2, determining the transfer function at each frequency point. The better the spatial and frequency resolution used, the better the prediction of the transfer function.

In the following sections, the uniform cantilevered beam in Figure 3.1 is used as a reference example. An LQR control design is derived for the reference

47

beam, calculating the associated kernels. A prediction of the LTF is generated from a high-order finite element model of the beam. A prediction of the LTF is also determined using the kernel predictions. The two are compared in an effort to verify the validity of the kernel predictions.

## 3.2    REFERENCE DESIGN: CONTROL OBJECTIVE

The characteristics of the reference beam are chosen to be those reported in Table 3.1. The performance output is chosen to be the transverse tip displacement of the beam. The LQR control design is tailored to regulate this performance output. The performance index for the control design can be represented by

$$\Im = \lim_{\tau \to \infty} \left[ \frac{1}{\tau} \int_0^\tau \left( y^T y + f^T \rho f \right) \delta t \right], \tag{3.3}$$

where $y$ is the performance output and $f$ is the tip force actuator. The tip actuator

**Table 3.1:**    Properties of the Reference Example

| PROPERTY | SYMBOL | VALUE |
|----------|--------|-------|
| Young's Modulus of Elasticity | E | 70 GPa |
| Material Density | $\rho$ | 2734 kg/m$^3$ |
| Structural Rigidity | EI | 7.113 N m$^2$ |
| Mass per unit length | $\rho$A | 0.330 kg/m |
| Cantilevered Length | L | 0.6096 m |
| Width | b | 0.0381 m |
| Height | h | 0.003175 m |
| Displacement Sensor Gain | $\kappa_1$ | 46.551 m/V |
| Control Actuator Gain | $\kappa_2$ | 3.889e$^{-3}$ N/V |
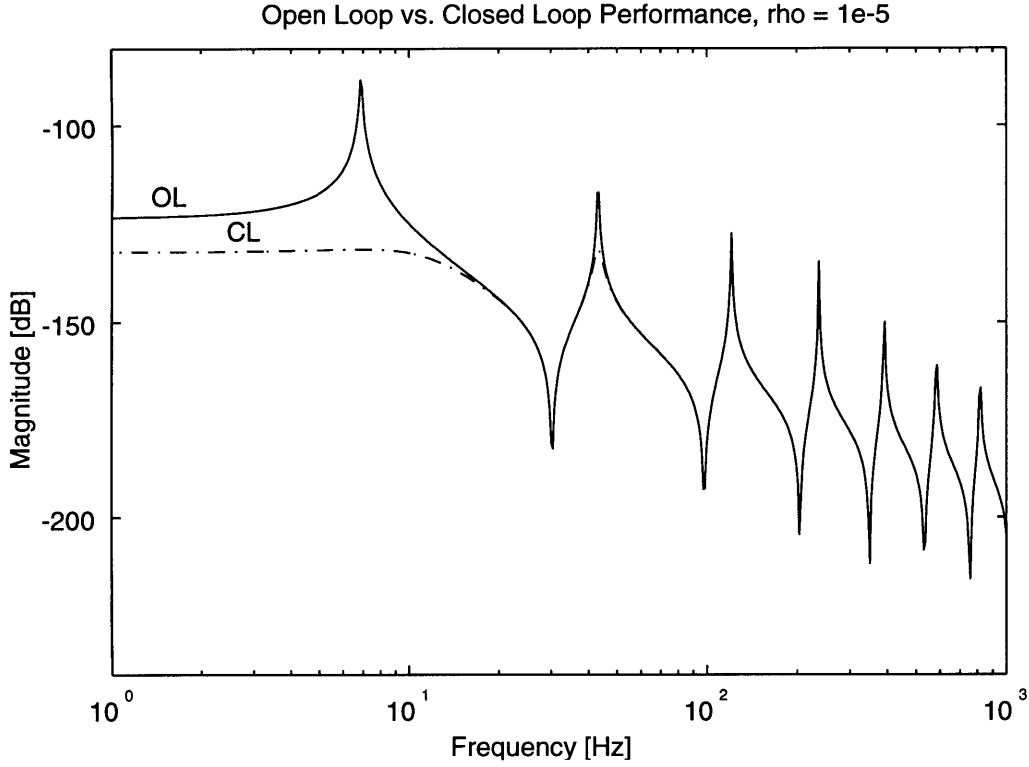
**Figure 3.3:** Open-loop and closed-loop performance output transfer functions for the reference example. Performance defined as the tip displacement. Open-loop (solid line), closed-loop (dashed-dotted line). LQR control weighting chosen to be 1e-5.

control weighting $\rho$ in the performance index is chosen to be 1e[-5]. Figure 3.3 shows the open-loop and closed-loop performance transfer functions for the reference example. The functions are determined with an accurate finite element model of the beam. The LQR feedback gains are determined for the model using standard Riccati solvers. The two functions can be represented by Equation 3.4.

$$H_{POTF}(j\varpi) = \frac{y(j\varpi)}{f(j\varpi)} = \left. C(j\varpi I - A)^{-1} B \right|_{Open-loop} \tag{3.4a}$$

$$H_{POTF}(j\varpi) = \left. C(j\varpi I - A + B[G_d \quad G_{dr}])^{-1} B \right|_{Closed-loop} \tag{3.4b}$$

As shown in Equation 3.4b, the closed-loop plot is determined using the LQR feedback gains.

The LTF for the control design is shown in Figure 3.4. It is also generated using an accurate finite element model of the beam and the LQR feedback gains derived for the model. The formal definition of stability for the system is specified by the Nyquist Stability Criterion [1, 8]. It requires that for all frequencies that the phase of the LTF is at or below -180 degrees, the magnitude of the LTF must not exceed 0 dB. Note that the LTF generated for the LQR control design meets the stability requirements. Also note the alternating pole-zero pattern that provides a stable phase profile for the LTF. These characteristics are guaranteed for an LQR control design.

The LTF has its largest magnitude value at the first bending mode of the beam. This suggests that the feedback force is most sensitive to vibrations associated with the first mode. This observation is reinforced by the results for the closed-loop performance transfer function in Figure 3.3. As shown, the control effort predominantly penalizes the first bending mode.

## 3.2 REFERENCE DESIGN: KERNEL PREDICTIONS

The infinite-order kernel predictions are determined using the Kernel Derivation Technique outlined in Chapter 2. The derivation technique uses twenty finite element models of increasing model order to calculate the kernels. The smallest model uses two beam-elements, and the largest uses forty.

The kernels are estimated for each model, and decomposed into the first ten curvature mode shapes. The weighting coefficients for each curvature mode shape are observed as a function of increasing model order. Plots of the curvature kernel weighting coefficients versus model order are shown in Figure

50
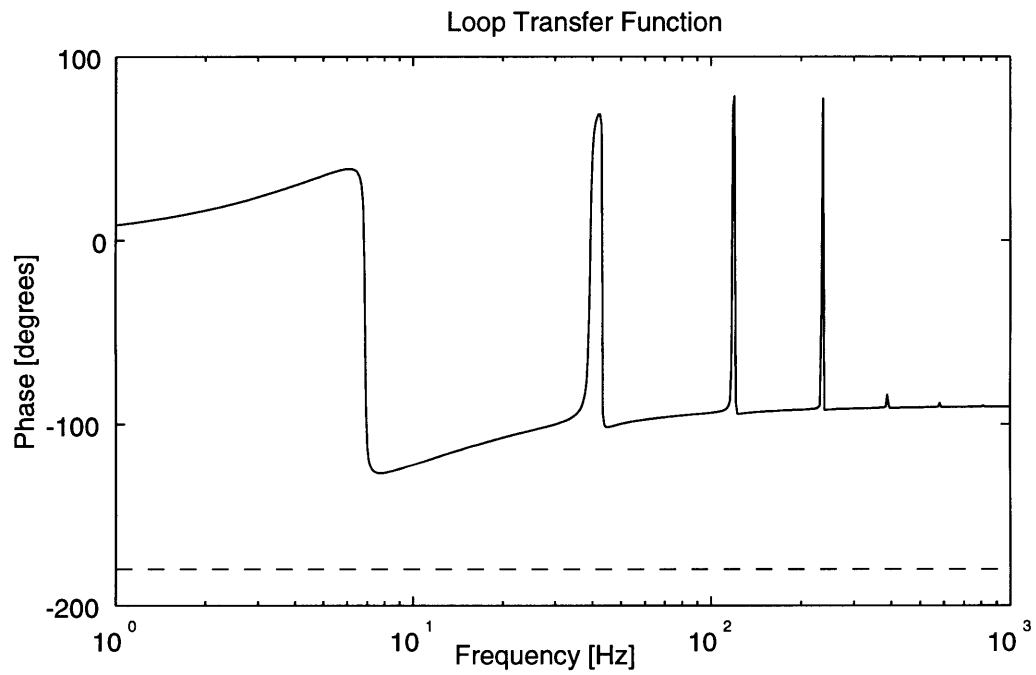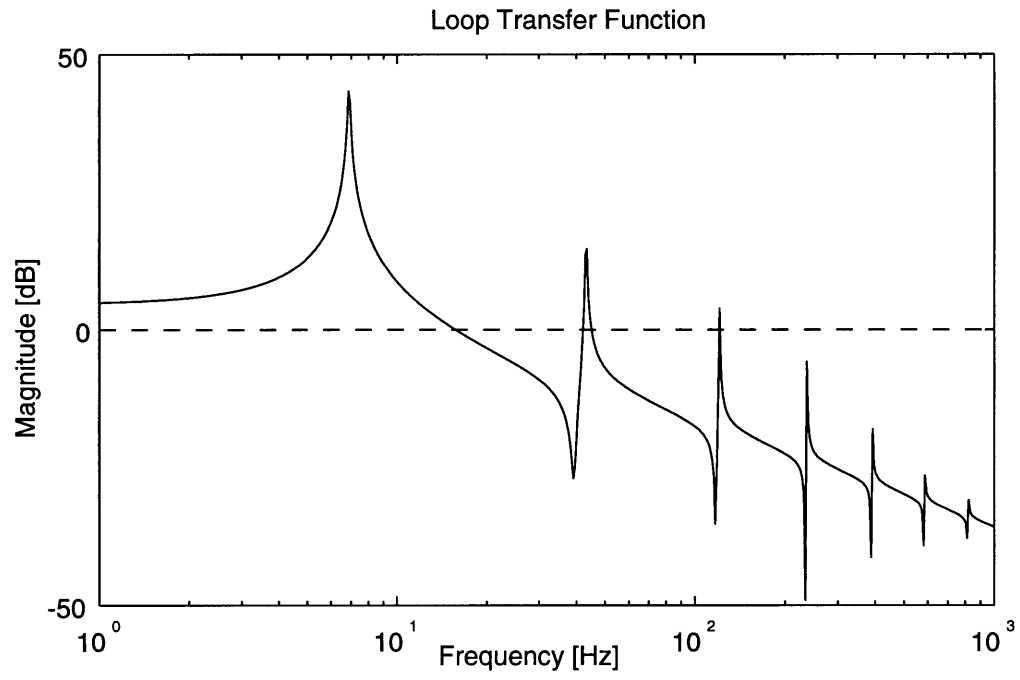
**Figure 3.4:** Loop transfer function for the reference example.

3.5 for the first four modes. The plots for the other six modes and for the curvature rate kernel are not shown, but are similar in nature. In fact, all the different weighting coefficients for the kernels appear to converge at the same rate.

Weighting coefficient models are produced to capture the trends seen in the plots of Figure 3.5. The models are used to determined the infinite-order values of the weighting coefficients. The infinite-order values are shown in Figure 3.6 Note that the first curvature mode shape is the largest contributor to both the curvature and curvature rate kernel predictions. The infinite-order values in Figure 3.6 are used to assemble the infinite-order kernel predictions. The predictions are shown in Figure 3.7. The predictions are used in a verification model that essentially derives the solution for Equation 3.2.

## 3.3   REFERENCE DESIGN: VERIFICATION OF KERNEL PREDICTIONS

The verification process uses a wave model of the cantilevered beam [14, 15]. The wave model can predict the frequency behavior of distributed curvature sensors attached to the beam. It can generate the transfer function from a distributed curvature sensor to a disturbance force at the beam tip.

The model essentially characterizes the behavior of the wave propagation in a uniform structure or uniform member of a structure. The structural member is modeled as a one dimensional wave guide with the appropriate boundary conditions. This type of model can capture the wave transmission characteristics of a uniform, Bernoulli-Euler beam. The approach is independent from the assumptions and methods used to generate a finite-element model of the beam. This allows the wave model to serve as an independent verification model for the kernel predictions.
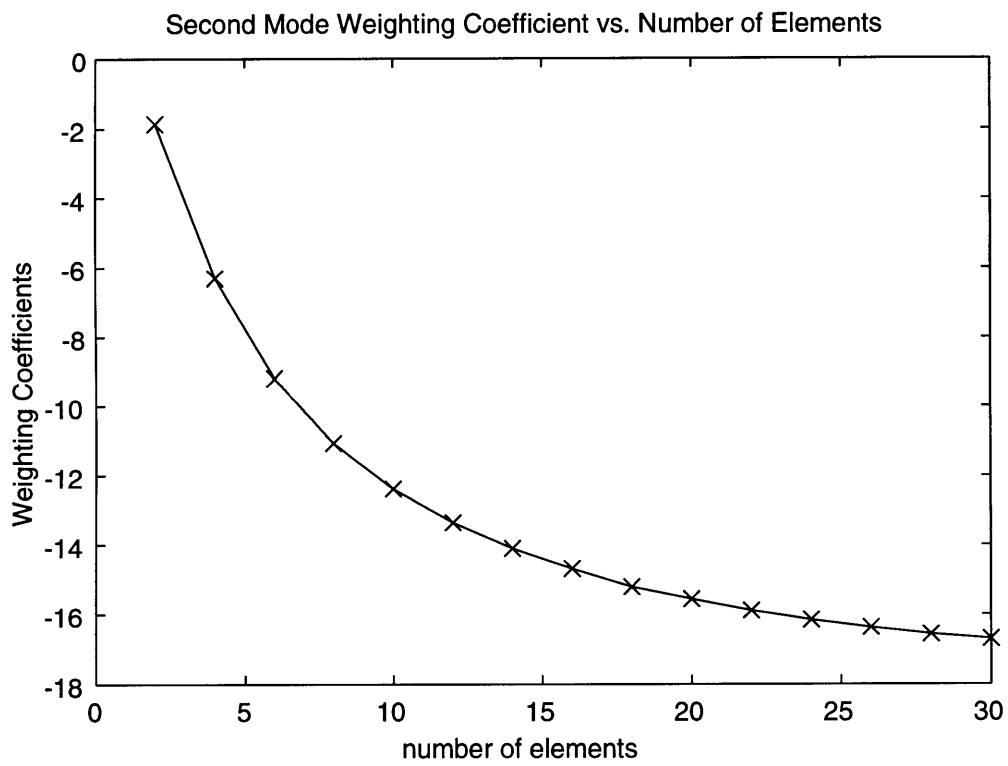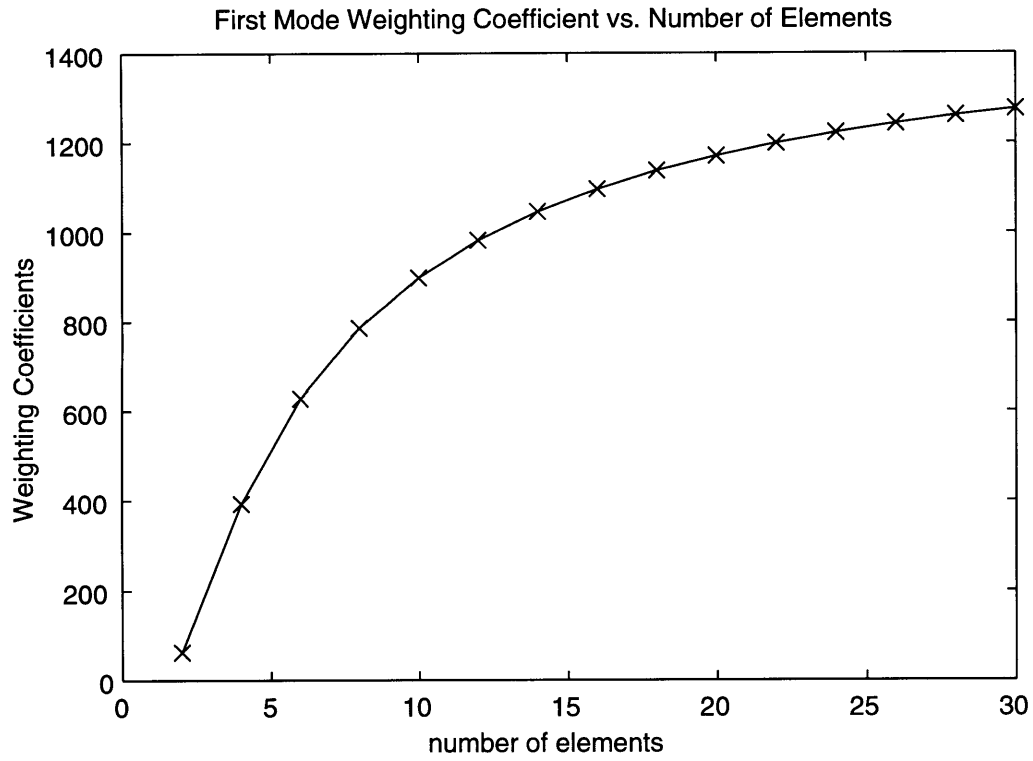
**Figure 3.5a:** First and second mode contributions to curvature kernel versus model order for the reference example kernels.
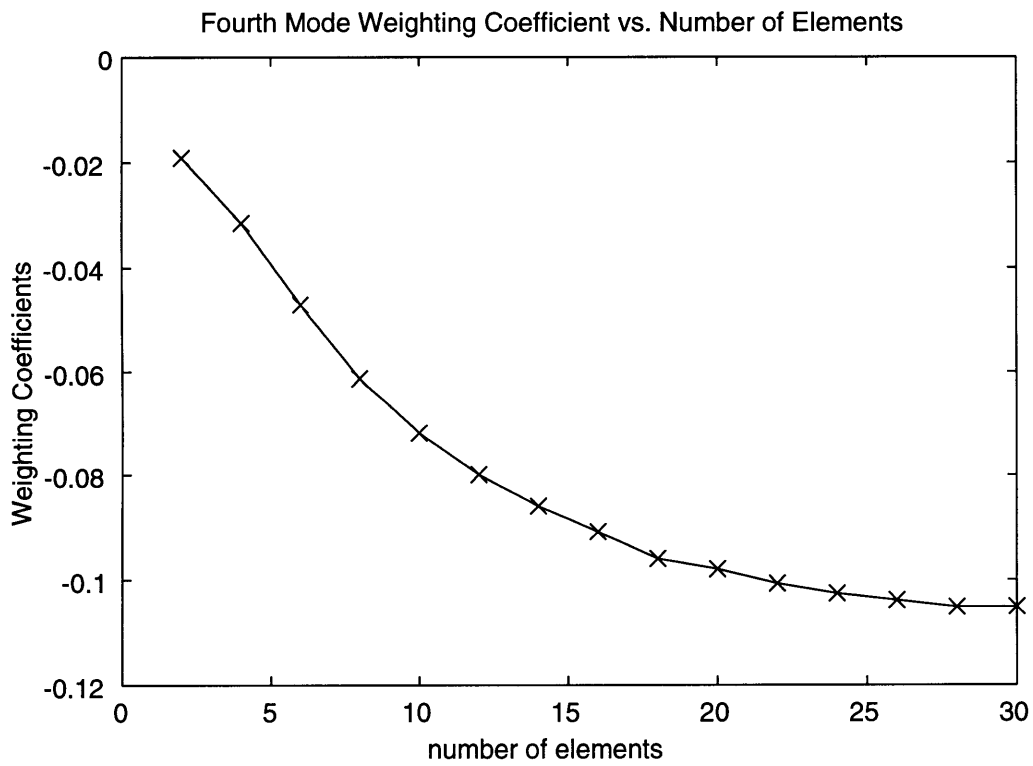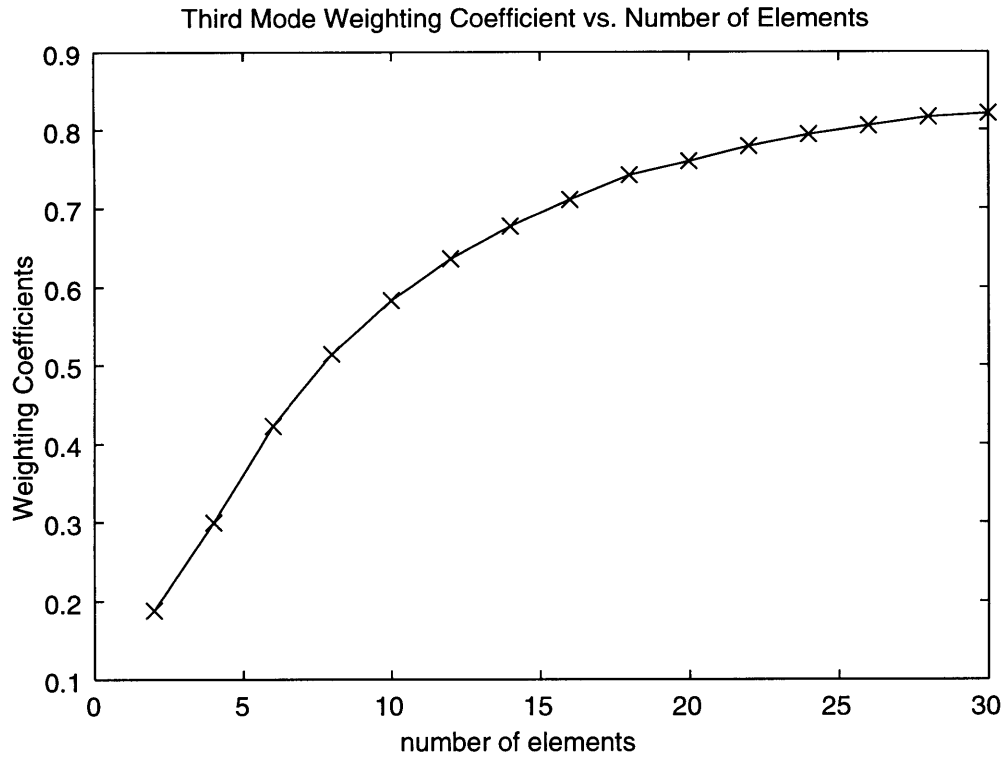
**Figure 3.5b:** Third and fourth mode contributions to the curvature kernel versus model order for the reference example kernels.
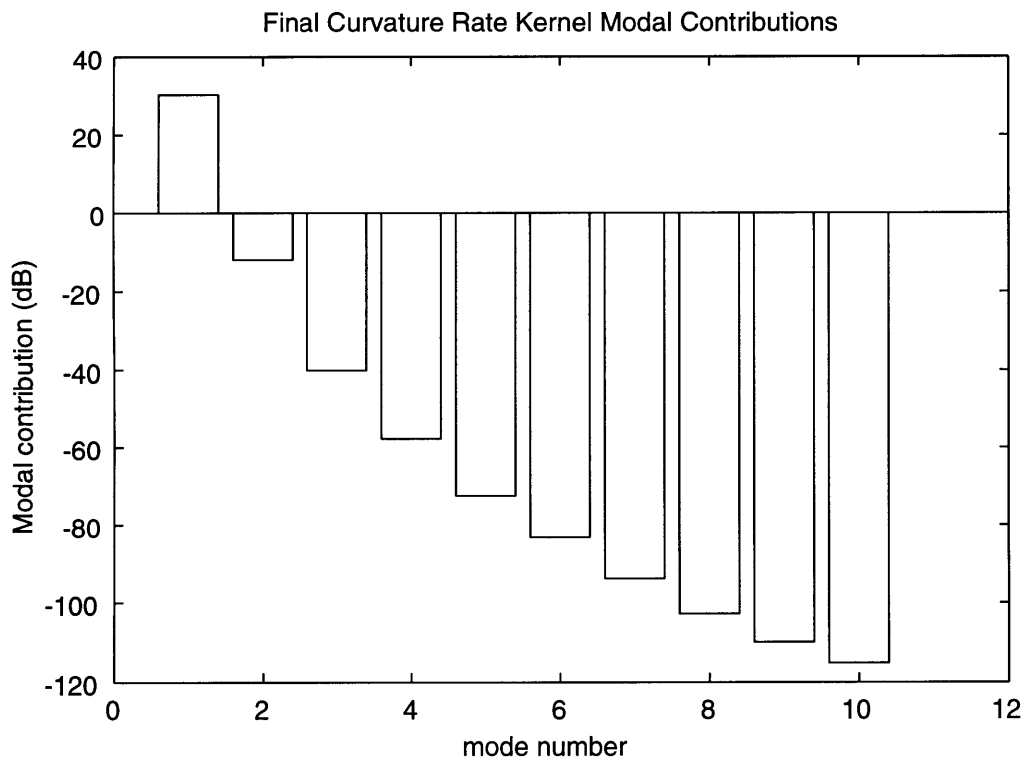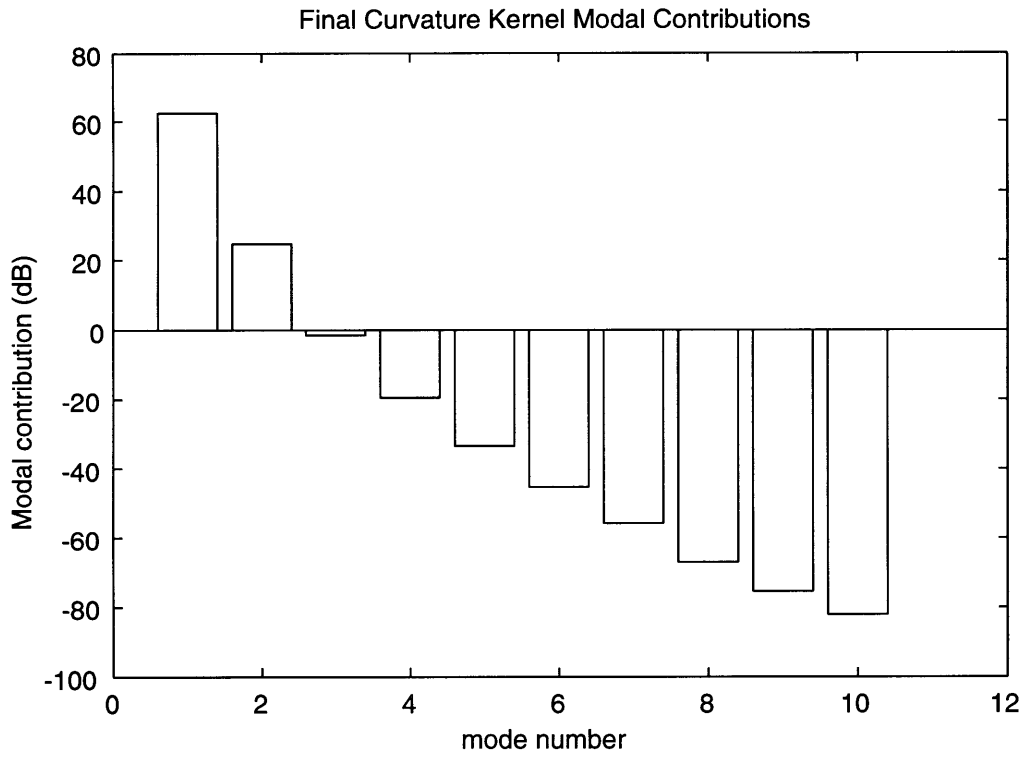
**Figure 3.6:** Final modal contributions for reference example kernels.

Comparison of Kernels, rho = 1e-5

normalized curvature rate kernel -- dashdot

normalized curvature kernel -- solid
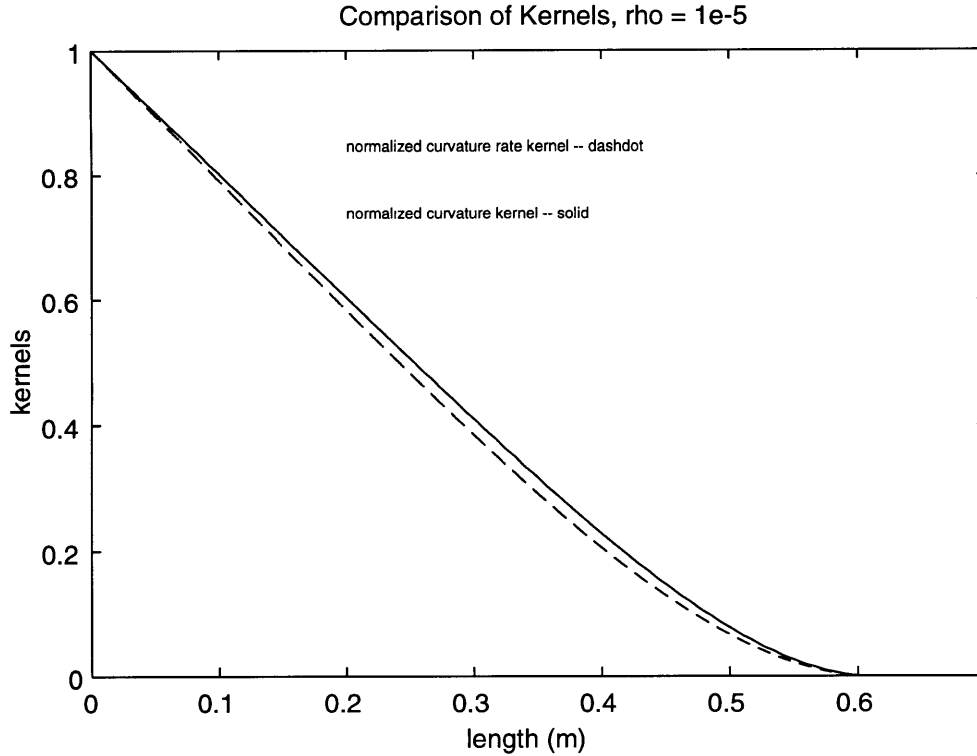
**Figure 3.7:** Infinite-order kernels for reference example. Normalized curvature kernel (solid line), normalized curvature rate kernel (dashed-dotted line).

In the wave model, the spatial weighting for the curvature sensor is variable. This flexibility allows the wave model to predict the frequency behavior of curvature sensors with different spatial weightings. In particular, the wave model can generate a curvature kernel transfer function and a curvature rate kernel transfer function. The two transfer functions correspond to the frequency behavior of distributed curvature sensors with curvature and curvature rate kernel-shaped electrodes, respectively. The prediction of the LTF for the control design is determined from the sum of these two transfer functions.

The finite element LTF and the wave model LTF generated from the kernels are compared in Figure 3.8. Besides some mismatching of the levels of damping on some of the modal frequencies, the two functions are identical. The

56
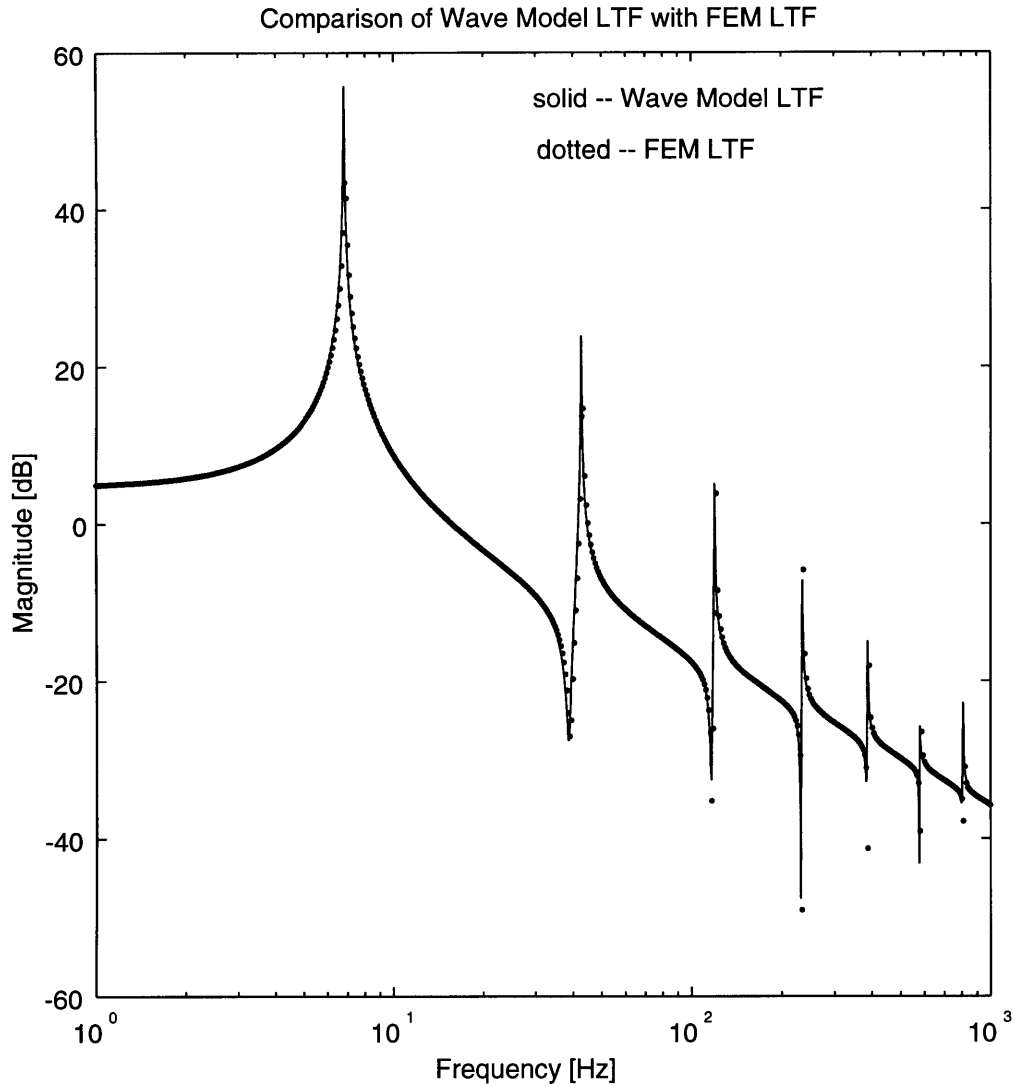
**Figure 3.8:** Comparison of the wave model loop transfer function prediction (dotted) based on the kernels and a high order FEM loop transfer function prediction (solid).

wave model successfully verifies the kernel prediction techniques. The control design is subject to the Bernoulli-Euler beam assumptions that have been made about the reference structure. It should be possible to replicate the modeled closed-loop results experimentally, as long as the test bed's behavior remains within the chosen modeling regime.

# Chapter 4

# Kernel Implementation Experiments

This chapter reports the results of two experiments. The goal of the experiments was to predict and implement the curvature kernels associated with two different Linear Quadratic Regulator (LQR) control designs. The control designs were for the vibration control of a cantilevered, aluminum beam. They were implemented through the use of polyvinylidene floride (PVDF) area averaging sensors attached to the beam. The setup for the experiments is discussed, along with the fabrication techniques for the PVDF area averaging sensors. Measured, closed-loop results are provided and compared with the modeled results to verify the if predicted performance is achieved.

## 4.1  TEST BED DESCRIPTION

The experimental test bed was a cantilevered, aluminum beam based on the reference example in Chapter 3. The properties of the aluminum beam are reported in Table 4.1, and Figure 4.1 shows the experimental setup. Two large metal blocks served as the clamp for the beam. The blocks were fastened together with vices, holding the beam in between them. The blocks holding the beam were fastened to a fairly rigid table. The beam was oriented such that the transverse displacement was perpendicular to the gravity field. This reduced the possibility of any gravity-induced stiffening or softening of the beam. There was

one force actuator located at the free end of the beam, as shown. The actuator was a non-contacting magnetic shaker. It produced a force by varying the magnetic field between a small target on the beam and the actuator magnet. The target was a small piece of steel shim-stock, which was placed on the beam with a piece durable, double-sided tape. In the experiments, PVDF film sensors were glued to the surfaces of the beam, covering the entire area. In this configuration (shown in Figure 4.1b), the target was placed on top of the sensors.

**Table 4.1:** Properties of the Test Bed

| PROPERTY | SYMBOL | VALUE |
|---|---|---|
| Young's Modulus of Elasticity | $E_{AL}$ | 70 GPa |
| Material Density | $\rho_{AL}$ | 2809 kg/m$^3$ |
| Structural Rigidity | EI | 7.113 N m$^2$ |
| Mass per unit length | $\rho A$ | 0.339 kg/m |
| Cantilevered Length | L | 0.6096 m |
| Width | b | 0.0381 m |
| Height | h | 0.003175 m |
| Displacement Sensor Gain | $\kappa_1$ | 46.551 m/V |
| Control Actuator Gain | $\kappa_2$ | 1.809e$^{-3}$ N/V |

There was a roll-off associated with the actuator at about 250 Hertz. The roll-off was a function of the inductor/resistor pole of the actuator and the distance between the magnet and the beam. The actuator was placed as close as possible to the beam to remain within a linear range of operation and to provide the best achievable level of actuation. The system was modeled as a uniform, cantilevered Bernoulli-Euler beam subjected to a tip force. The models of the beam used in the Kernel Derivation Technique (which is outlined in Chapter 2) were based on finite-element methods.
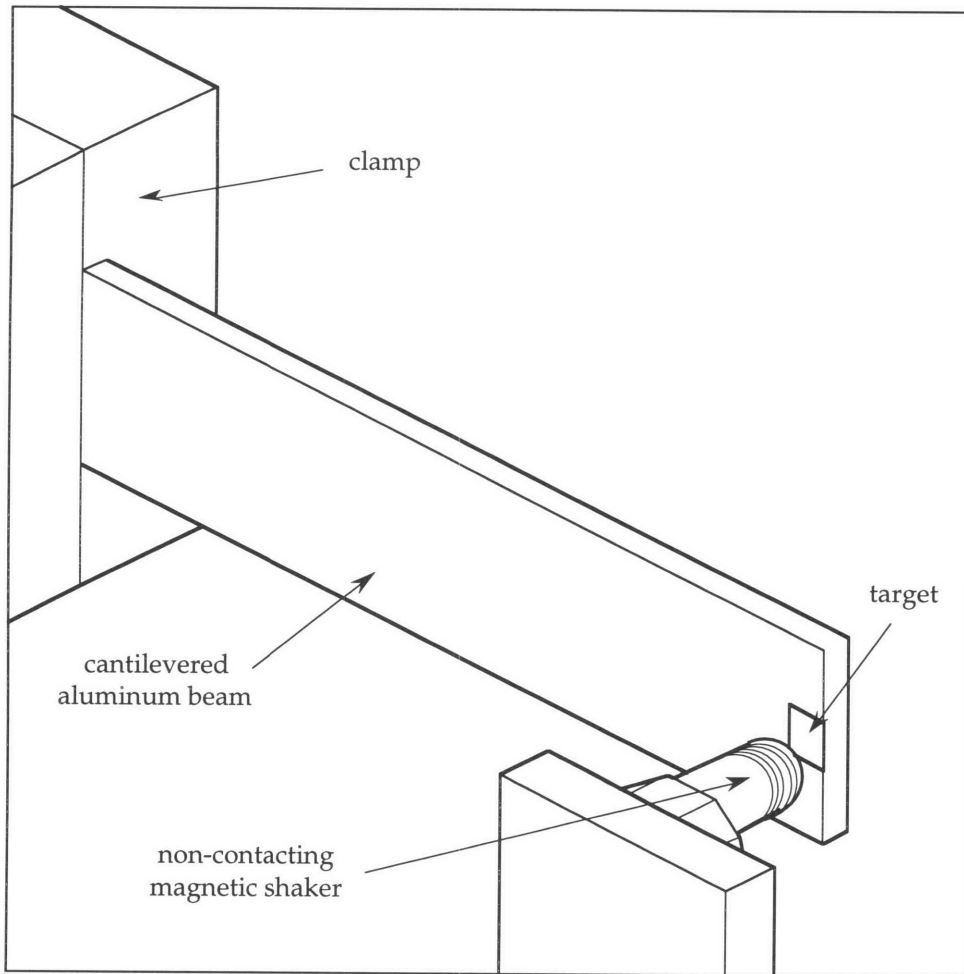
(a) Illustration of the test bed
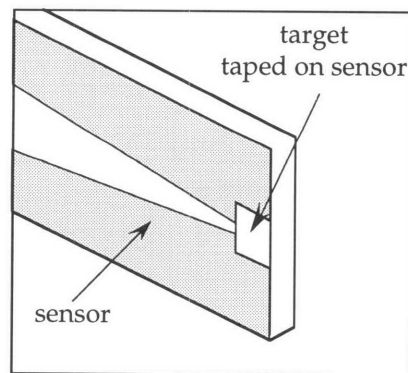


(b) Target configuration with sensors

**Figure 4.1:** Experimental setup of the test aluminum beam.

Additional non-physical states to account for the actuator roll-off were not included in the finite-order design models of the beam. The application of LQR control designs to the models including the non-physical states would introduce complications. The process would produce additional feedback gains for the non-physical states. The additional gains would make the feedback dependent on non-physical measurements. This dependence would affect the kernel predictions. Performing this operation presented an unnecessary complication, since the actuator dynamics didn't introduce any instability to the system. The roll-off was also outside of the effective control bandwidth of the LQR designs. The effective bandwidth for both designs encompassed only the first two bending modes of the beam. Therefore, there weren't any problems introduced by calculating the LQR feedback gains without accounting for the actuator roll-off.

The following two sections discuss the results and engineering choices for the two experiments. The control objective of the first experiment was to penalize the transverse tip displacement of the beam. The objective of the second was to penalize the difference between the transverse tip and mid-point displacement.

## 4.2    EXPERIMENT 1: KERNEL PREDICTIONS

Experiment 1 was essentially an attempt to implement the results obtained in the reference example of Chapter 3. The curvature kernel predictions for the first experiment were found using the Kernel Derivation Technique outlined in Chapter 2. The observed trends and characteristics of the derivation technique were completely identical to those seen for the reference example in Chapter 3.

Comparison of Axially Unsymmetric Kernels, rho = 1e-5

solid -- normalized curvature kernel

dashed -- normalized curvature rate kernel

(a)



Comparison of Axially Symmetric Kernels, rho = 1e-5

solid -- normalized curvature kernel

dashed -- normalized curvature rate kernel
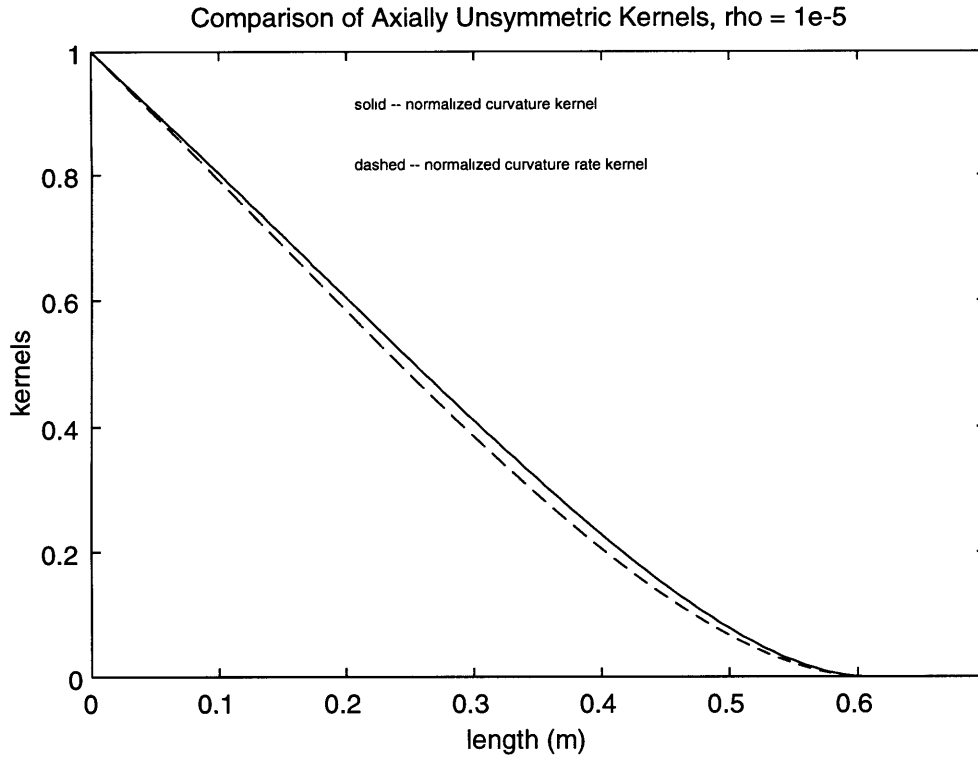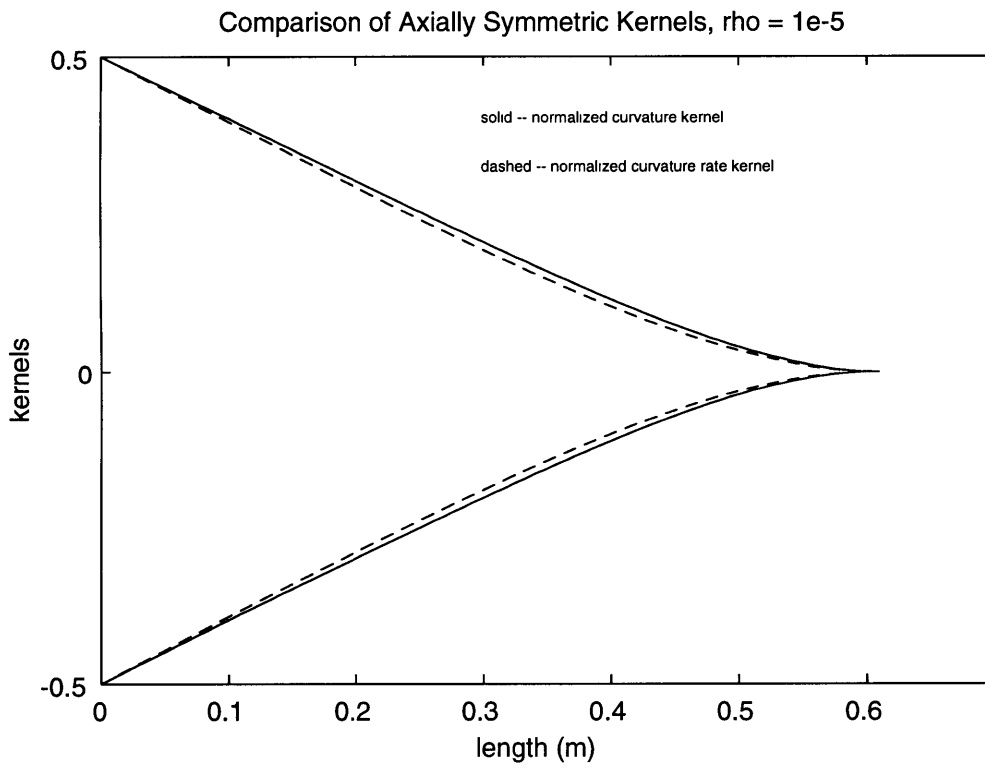
(b)

**Figure 4.2:**      Infinite-order kernel predictions.

The predicted curvature and curvature rate kernels are shown in Figure 4.2a. The resulting shapes were also identical to those derived in Chapter 3.

In an experiment, PVDF sensors fabricated with the unsymmetric electrode shapes in Figure 4.2a would be sensitive to the bending and torsion modes of the beam. The control design was for the vibration control of transverse bending modes only. The sensitivity of the sensor outputs to torsion modes would corrupt the achievable performance levels. Therefore, the sensor electrodes were fabricated with the axially symmetric kernel shapes in Figure 4.2b. The sensors with the symmetric electrodes would be insensitive to any torsional motion. The torsional contributions in the signals associated with the top and bottom halves of these sensors would negate each other, and the output signal would only capture the bending motion, as desired.

## 4.3 EXPERIMENT 1: SENSOR FABRICATION TECHNIQUES

The symmetric shapes were etched onto rectangular pieces of PVDF film in the following manner. The sheets of film were chosen to have the same width and length as the beam. Computer-generated images of the shapes were made. The images were plotted to full scale on opaque, single-sided, adhesive paper. The shapes were carefully cut out of the paper and applied to the surface of the film. The adhesive paper now covered the desired surface area of the electrodes. The unwanted, uncovered electrode surface was removed using a metal etchant. The adhesive paper protected the desired electrode surface during the etching. After the etching, the adhesive paper was removed from the desired electrode surface of the new created sensors.

Initially, two sensors were created: a curvature sensor and a curvature rate sensor. The sensors were glued to the two sides of the beam with epoxy, one

sensor on each side. Thin, adhesive copper strips were used as signal leads. The voltage signals from the film sensors were obtained with some simple conditioning circuitry.

The first tests with the sensors showed that, due to ambient noise levels, measured transfer function data from a tip disturbance to the output of the sensors differed from their predicted behavior. A wave model [14, 15] was used to predict the sensor transfer functions. One major difference between the model and the measured data was in the phase of the zeros. The zeros in the measured transfer function data were observed to be non-minimum phase, when they were predicted to be minimum phase.

There were many possible causes for this behavior. If the zeros in the transfer functions were very lightly-damped, the problem could be blamed on the data acquisition resolution. With such lightly damped zeros, it is often hard to discern if they are non-minimum or minimum phase from measured transfer function data, especially if the ambient noise levels are appreciable. Non-minimum phase behavior is also a common tendency with non-collocated transfer functions. It was possible that the sensors might not be properly aligned on the test structure, leading to the non-minimum phase behavior. Also, there was no modeling accounting for the beam-epoxy-sensor interactions. It was assumed that the epoxy layer was negligible and that it did not alter the surface strain measurement.

A quantitative definition the problem was not discovered, but a means of circumventing the problem was determined. It was found that the observed errors could be alleviated by developing a common-mode-rejection circuit design. Two of each sensor could be placed on either side of the beam with the electrical signals of the pairs differenced. When the beam with these sensors experienced bending, one side would be in compression while the other was in

tension, and the signals from the two sensor pairs associated with the bending would be amplified. Any noise or other signals common to both sides would be canceled out. This four-sensor design is illustrated in Figure 4.3.

For the differenced pair of curvature sensors in the four-sensor design, the desired voltage signal is represented by Equation 4.1a,

$$V_c(t) \;=\; G_c \frac{Q_f(t)}{C_f} \;=\; G_c \left( \left. \frac{Q(t)}{C_f} \right|_{front} - \left. \frac{Q(t)}{C_f} \right|_{back} \right) \tag{4.1a}$$

where

$$\left. \frac{Q(t)}{C_f} \right|_{front} \;=\; - \left. \frac{Q(t)}{C_f} \right|_{back} \;=\; \frac{e_{31}h}{2C_f} \int_0^L F_c(x) \frac{\delta^2}{\delta x^2} \omega(x,t)\delta x. \tag{4.1b}$$
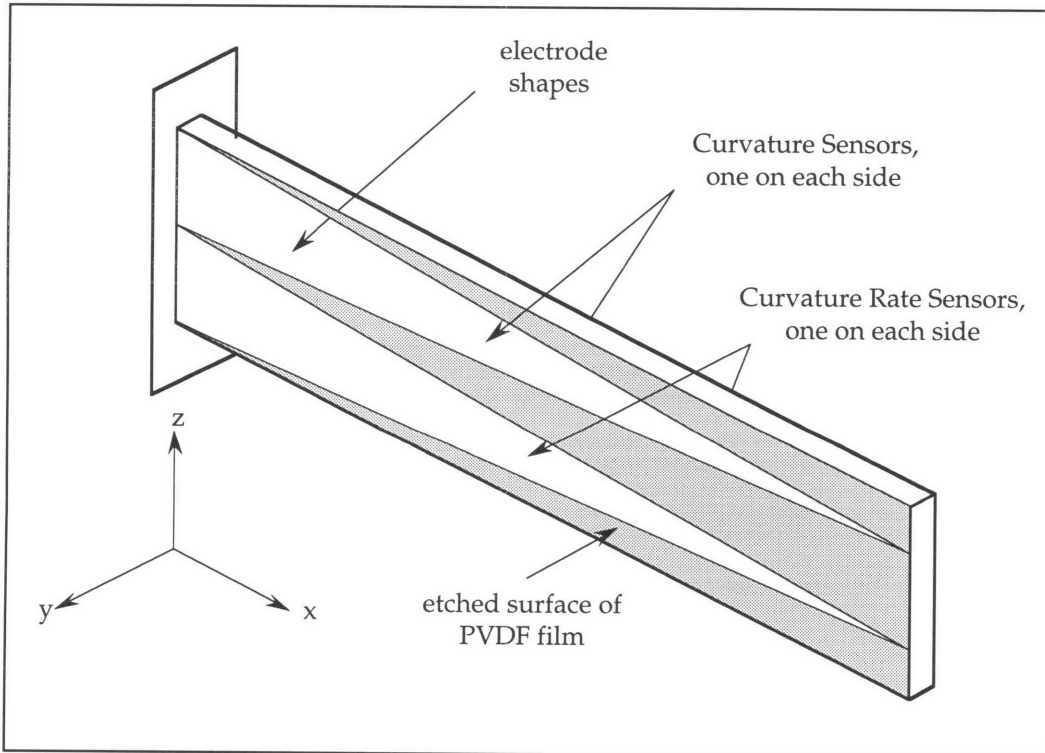


**Figure 4.3:** Four-sensor fabrication design.

In this expression, the differenced voltage signal $V_c$ is proportional to the charge differential $Q_f$ between the two pieces of film on either side of the beam. The term $F_c$ represents the etched shapes on the two PVDF curvature sensors, and the term $G_c$ is the curvature gain, which is defined as

$$G_c = -\frac{C_f K_c(x)}{e_{31} h F_c(x)} \quad \frac{\text{Farads} \cdot \text{Volts}}{\dfrac{\text{Coulomb}}{\text{meters}^2} \cdot \text{meters}^2}.$$ (4.2)

This gain enables the following equality

$$V_c(t) = \frac{1}{\kappa_2} f_d(t),$$ (4.3)

where $f_d$ is the displacement part of the feedback force, and $\kappa_2$ is the newtons-to-volts conversion factor for the experiment. Term $K_c$ in the definition of the curvature gain represents the curvature kernel prediction. The Kernel Derivation Technique is scaled to produce curvature kernel predictions in units of volts, such that the needed scalar gain $G_c$ can be determined.

For the differenced curvature rate sensors, the desired signal is represented by Equation 4.4a,

$$V_{cr}(t) = G_{cr} R_{eq} I_f(t) = G_{cr} \left( R_{eq} I(t) \big|_{\text{front}} - R_{eq} I(t) \big|_{\text{back}} \right)$$ (4.4a)

where

$$R_{eq} I(t) \big|_{\text{front}} = -R_{eq} I(t) \big|_{\text{back}} = R_{eq} \frac{e_{31} h}{2} \int_0^L F_{cr}(x) \frac{\delta^3}{\delta t \delta x^2} \omega(x,t) \delta x.$$ (4.4b)

The voltage signal $V_{cr}$ is proportional to the differenced current $I_f$. The term $F_{cr}$ represents the etched shapes on the two curvature rate sensors, $R_{eq}$ represents the

equivalent resistance of the circuit used to measure the voltage signal, and $G_{cr}$ is the curvature rate gain, which is represented by Equation 4.5.

$$G_{cr} = \frac{K_{cr}(x)}{R_{eq}\,e_{31}\,h\,F_{cr}(x)} \quad \frac{\text{Volts} \cdot \text{seconds}}{\text{Ohms} \cdot \dfrac{\text{Coulomb}}{\text{meters}^2} \cdot \text{meters}^2} \tag{4.5}$$

The curvature rate gain enables the equality,

$$V_{cr}(t) = \frac{1}{\kappa_2} f_{dr}(t), \tag{4.6}$$

where $f_{dr}$ is the displacement rate part of the feedback force. The term $K_{cr}$ in Equation 4.5 represents the curvature rate kernel prediction. The Kernel Derivation Technique is scaled to produce curvature rate kernel predictions in units of volts·seconds, allowing $G_{cr}$ to be determined. In employing the four-sensor fabrication design, the sum of the two voltage signals $V_c$ and $V_{cr}$ can be used to provide the needed LQR feedback command signal.

## 4.4  EXPERIMENT 1: RESULTS

In the actual implementation, it was beneficial to take advantage of the fact that the curvature and curvature rate kernels were almost identical in shape. Instead of using the four-sensor design, a proportional-derivative (PD) compensator could be applied to the output of the differenced pair of curvature sensors to simulate the same behavior. Therefore, only two curvature sensors were fabricated and applied to the beam. The implemented fabrication design is illustrated in Figure 4.4. The compensator was constructed from simple analog devices. The electric signals from the two curvature sensors were differenced,
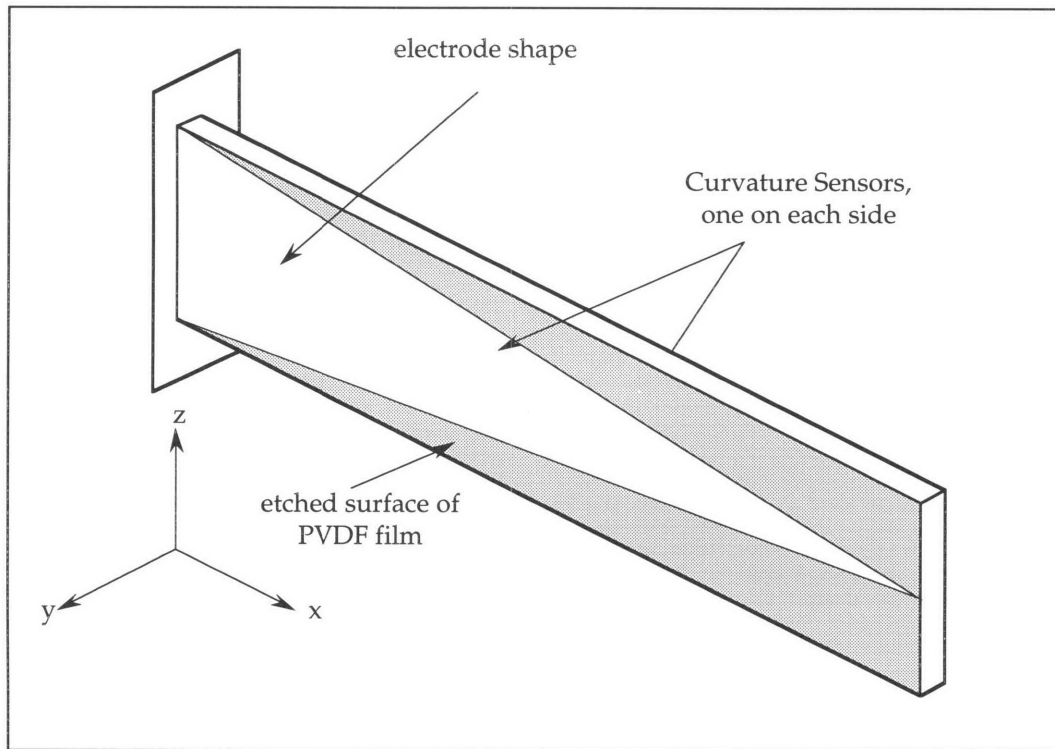
**Figure 4.4:** Illustration of the application of two curvature sensors to the cantilevered beam.

and the errors similar to those seen in the initial sensor tests were greatly reduced over the effective control design bandwidth. The transfer function of the required PD compensator is represented by Equation 4.7,

$$H_{PD}(j\varpi) \quad = \quad G_c + G_{cr} \frac{(2\pi p_{cr} j\varpi)}{(j\varpi + 2\pi p_{cr})} \tag{4.7}$$

where $G_c$ and $G_{cr}$ are the needed curvature and curvature rate gains defined previously. The differentiation part of the PD compensator was chosen to have the particular structure shown in Equation 4.7 because a perfect differentiator constructed from simple analog devices would amplify any ambient high frequency noise. The value of the cutoff frequency $p_{cr}$ shown in the

differentiation part of the compensator was chosen to be sufficiently large, such that the transfer function resembled

$$H_{PD}(j\varpi) \cong G_c + G_{cr}j\varpi, \qquad j\varpi << 2\pi p_{cr}. \qquad (4.8)$$

over the effective control design bandwidth. The implemented value of $p_{cr}$ was 504 Hertz. This was well above the first four bending modes of the beam, and the effective control design bandwidth only encompassed the first two modes. The feedback was implemented with this PD compensator, allowing the loop to be closed.

The performance transfer function was observed in open and closed-loop conditions. The results showed a good match between the predicted performance and the data, and are shown in Figure 4.5. As shown, the motion associated with the first bending mode has been substantially reduced, as desired. In contrast to the model, the experimental data manifested a slight stiffening of the second bending mode of the beam, and a decrease in damping for the third bending mode and third local zero.

It was probable that the cutoff frequency $p_{cr}$ was actually too low. The stiffening provided by the control design can be attributed to the proportional part of the PD compensator, and the damping can be attributed to the differentiation part. If $p_{cr}$ was too low, it would offset the stiffness-to-damping ratio in favor of more stiffening. This would have also decreased the damping level over the same range, but this is not observed. The second bending mode has been stiffened, but its measured damping level is comparable to its predicted level. However, experiments using higher values of $p_{cr}$ did cause the compensator to amplify ambient high frequency noise, jeopardizing the achievement of closed-loop results.

The cause of the discrepancies in the closed-loop data was most likely due the design choice of using the two curvature sensors in conjunction with the PD compensator. This choice provided only an estimate of the behavior that would have been obtained from the four-sensor design outlined in Section 4.3. It was an estimation in the sense that the curvature and curvature rate kernels were not exactly identical. The estimate was considered acceptable, but the consequences appear to be the discrepancies seen in the closed-loop transfer function data.

The poor resolution observed in the data transfer functions below 5 Hertz was due to the sensor used to measure the tip motion. The sensor was an accelerometer, and it could not resolve signals below that range. The transfer function data from the accelerometer was integrated twice to yield the tip displacement transfer functions shown in Figure 4.5.

In summary, other than the slight differences observed in the experiment mentioned above, the implementation of an LQR control design was successfully achieved with the PVDF area averaging sensors. The results were slightly suboptimal, but the design was very easy to implement. The implementation was much simpler than a design using a larger array of discrete point sensors, and the experiment demonstrated the ability to integrate feedback measurement devices into the design of a structure.

Modeled Open Loop vs. Closed Loop Performance, rho = 1e-5
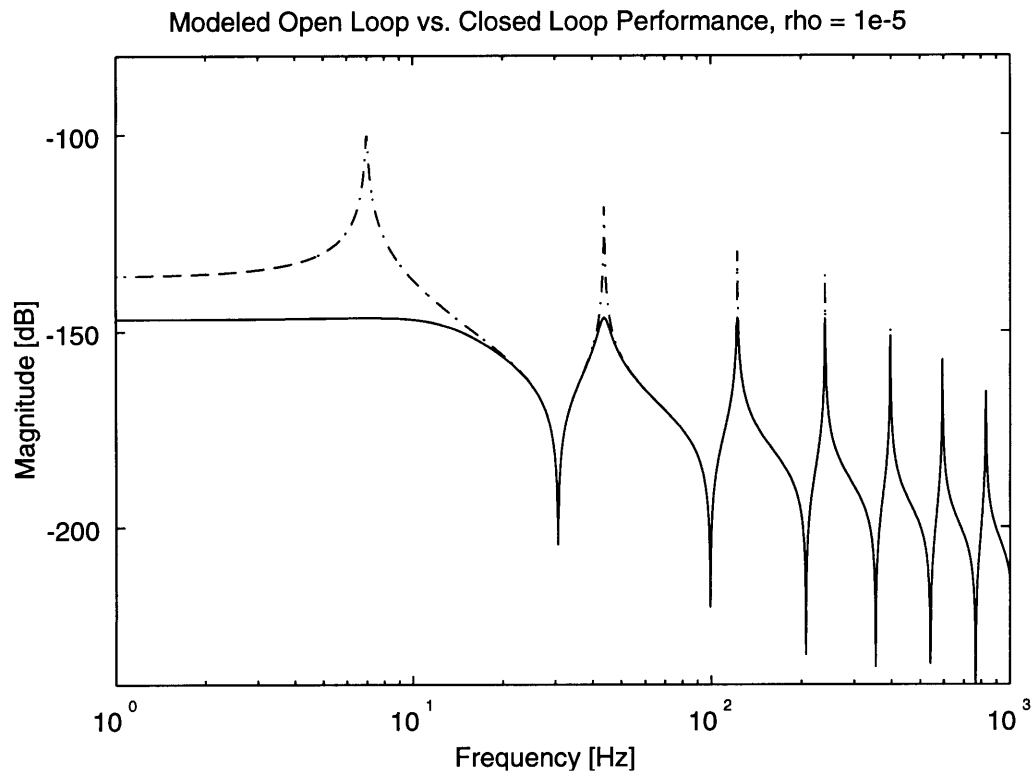
**Figure 4.5a:** Open-loop and closed-loop performance output transfer functions, model. Open-loop (dash - dotted), and closed-loop (solid).

71
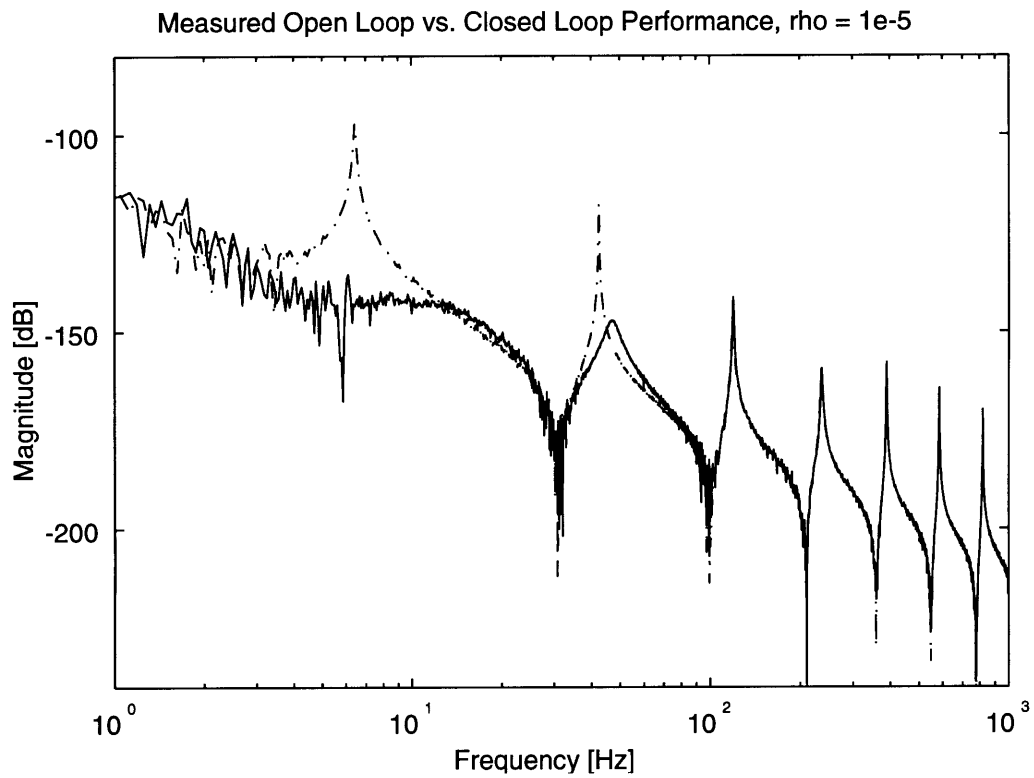
Figure 4.5b: Open-loop and closed-loop performance output transfer functions, measured data shown. Open-loop (dash-dotted), and closed-loop (solid).

## 4.5    EXPERIMENT 2: KERNEL PREDICTIONS

It was of particular interest to show the success of this control design approach for another case. The success of another case would help demonstrate the versatility of this type of control design. It would also reveal any common trends or characteristics present between different cases, be they good or bad. Therefore, a second experiment was performed. The control design tailored to regulate the difference between the transverse tip and mid-point displacement of the beam. The performance index for experiment 2 is represented by Equation 4.9.

$$\Im \quad = \quad \lim_{\tau \to \infty}\left[\frac{1}{\tau}\int_{0}^{\tau}\left(z^{T}C^{T}Cz + f^{T}\rho f\right)\delta t\right]$$

$$z^{T}C^{T}Cz \quad = \quad (\omega(L,t) - \omega(L/2,t))^{2} \qquad\qquad (4.9)$$

The control weighting $\rho$ for the LQR control design was chosen to be 1e$^{-6}$. The associated infinite-order kernels for the control problem were predicted with the Kernel Derivation Technique.

Plots of the modal weighting coefficients for the curvature kernel shape versus model order are shown in Figure 4.6 for the first four modes. The four plots are representative of the type of weighting coefficient trends observed for the control design. Therefore, the plots for the other six modes and the curvature rate weighting coefficients are not shown. The infinite-order values for the different modal contributions to the kernel shapes are shown in Figure 4.7. The distribution shows the kernel predictions to be dominated by the first and second curvature mode shapes. The infinite-order kernel predictions for experiment 2 are shown in Figure 4.8.

## First Mode Weighting Coefficient vs. Number of Elements



## Second Mode Weighting Coefficient vs. Number of Elements
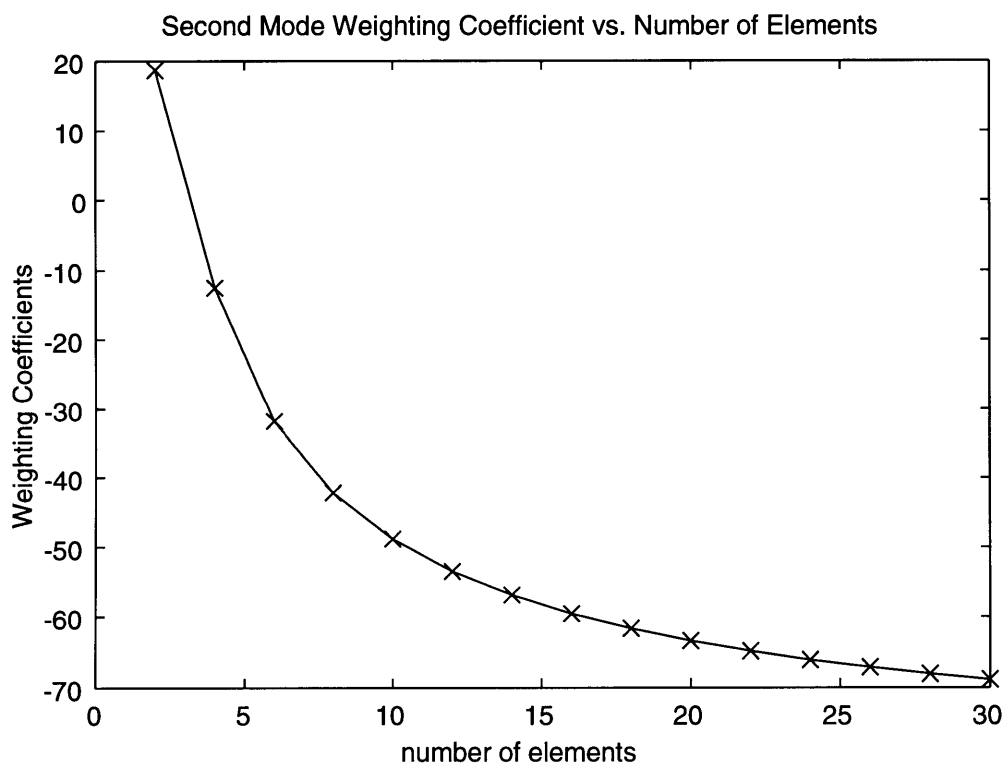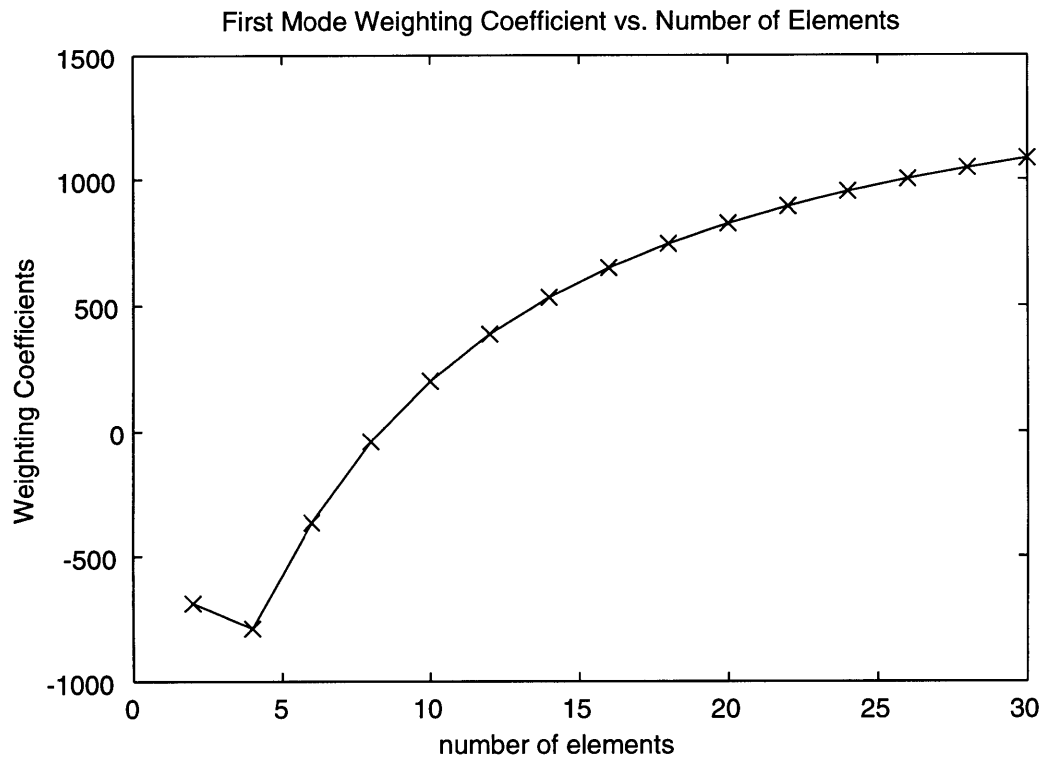


**Figure 4.6a:** First and second curvature mode shape weighting coefficients versus model order. Weighting coefficients are for the curvature kernel .

74
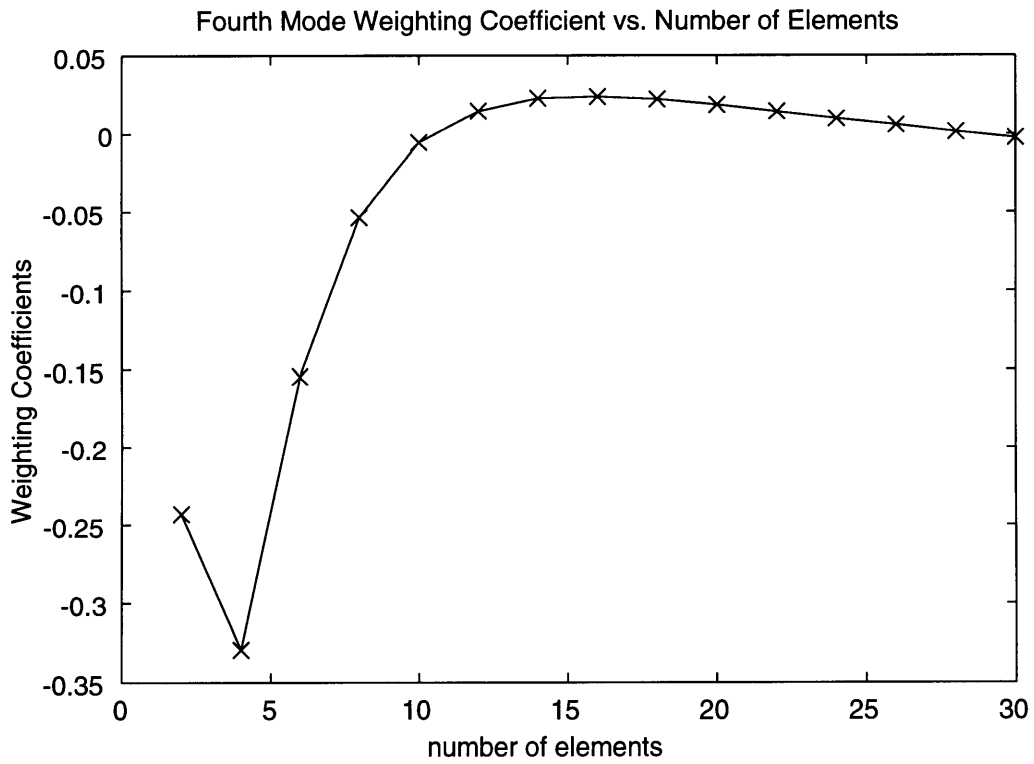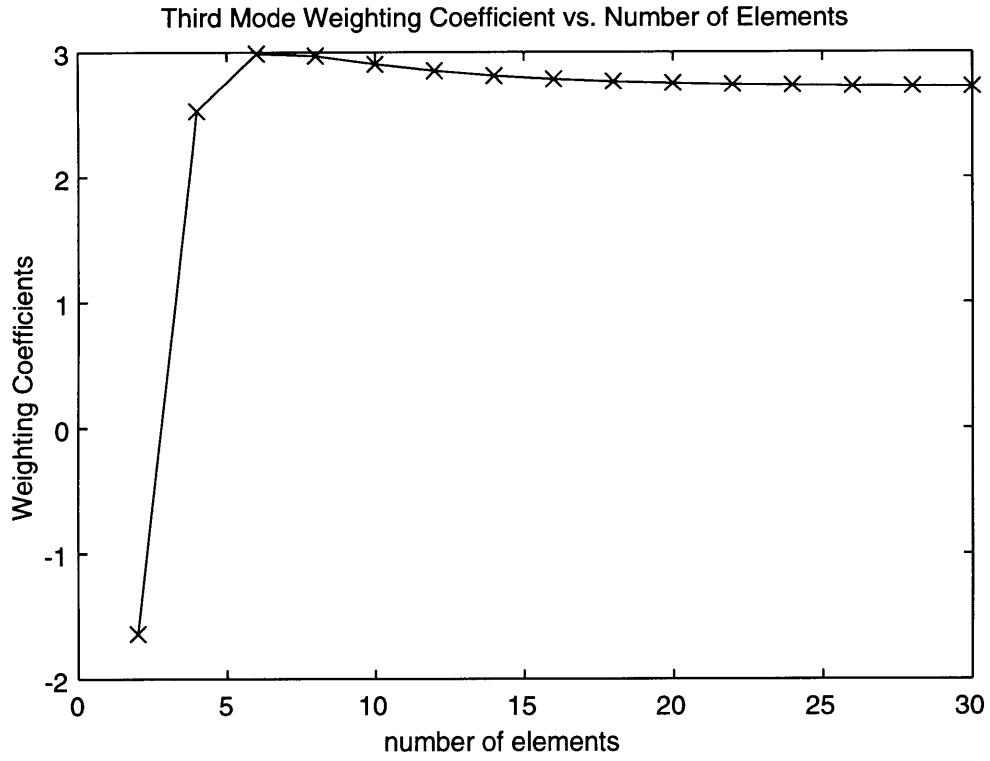
**Figure 4.6b:** Third and fourth curvature mode shape weighting coefficients versus model order. Weighting coefficients are for the curvature kernel.
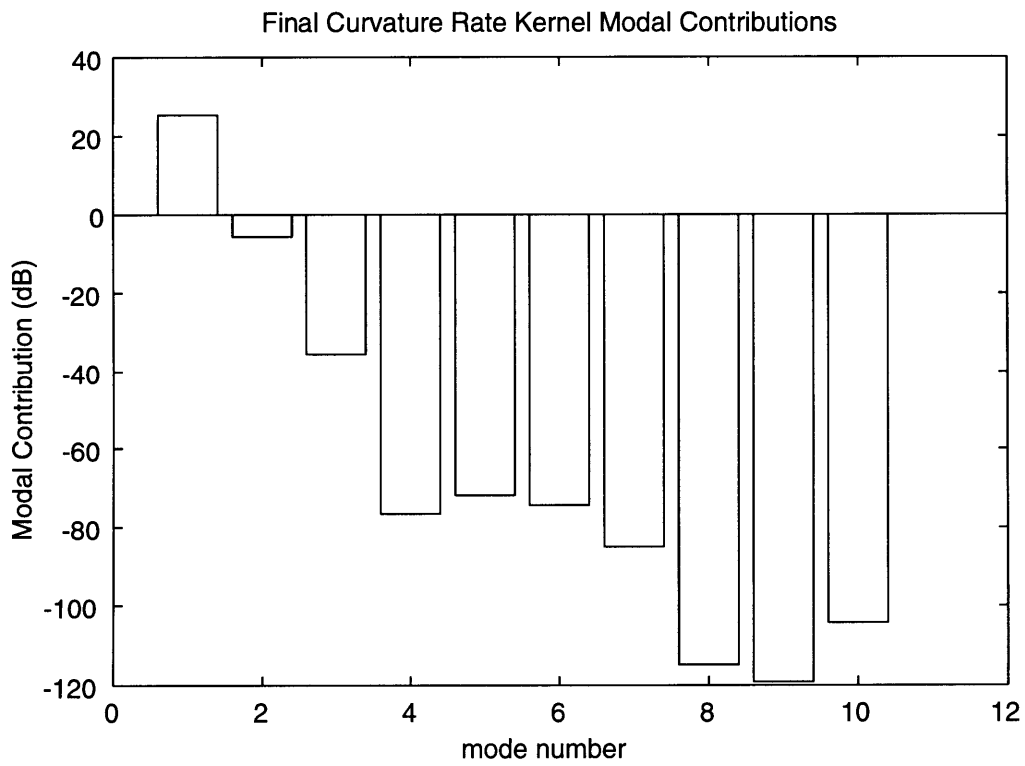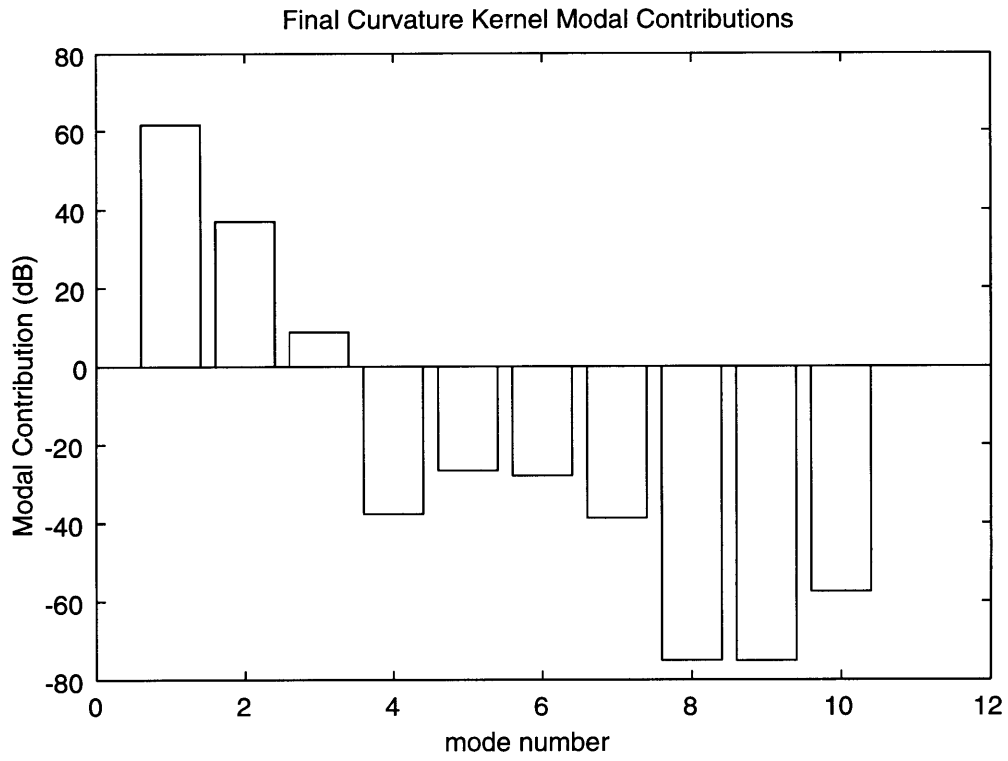
**Figure 4.7:** Final modal contributions to kernels.
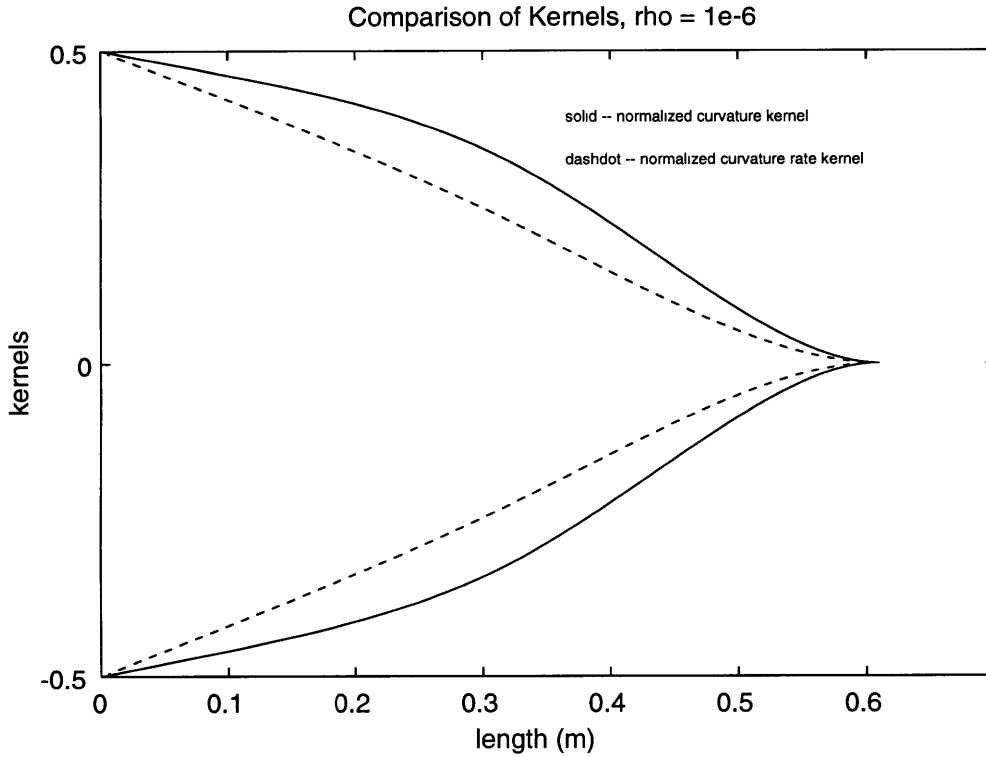
**Figure 4.8:** Infinite-order kernel predictions.

These trends can be compared to those determined in Chapter 3 for the tip-displacement regulator. In Chapter 3, the different modal weighting coefficients all converge in a relatively similar manner and rate. Most of them resemble a function of the form,

$$H_{WCM}(j)\big|_r = C_r(1 - e^{j/\tau_{decay}}),$$ (4.10)

where $C_r$ represents the infinite-order value for mode $r$ that the function decays towards. The term $\tau_{decay}$ represents the function decay rate, and variable $j$ is the model order.

The changes as a function of model order were mainly seen in the magnitudes of the kernels in Chapter 3; the shapes of the kernels determined from different models varied only slightly. Essentially, the final infinite-order

77

kernels in Chapter 3 were not very different in shape from kernels produced from a two beam-element model.

If this result applied to every case, it would be very convenient. Good estimations of the infinite-order kernel shapes could be found with very low order models. The full application of the Kernel Derivation Technique would still be required to find the infinite-order kernel magnitudes.

The kernel derivation results for experiment 2 show that these trends from the control design in Chapter 3 are not common to all cases. The mode shape weighting coefficients change in a completely different manner. This is visible in Figure 4.6 by the changes in signs for some of the mode shape weighting coefficients. The behavior corresponds to the fact that large changes in the kernel shapes determined from the different size models occur. There are also changes in the overall kernel magnitudes. The final infinite-order kernels for experiment 2 are very different in shape and magnitude from kernels produced from a low order model.

It is hypothesized that the different trends observed are a function of a performance output sensitivity to the model fidelity. It is probable that lower order finite element models can capture the true physical behavior of the some performance outputs very well, like the tip displacement. Other performance outputs, like the difference between the tip and mid-point displacement, may require a higher model fidelity to capture the true physical behavior.

The curvature and curvature rate kernel shapes in Figure 4.8 are dissimilar. This outcome is also in contrast to the results in Chapter 3, where the two kernel shapes are approximately the same. The dissimilarity between the curvature and curvature rate kernel can be attributed to the different damping-to-stiffness ratios achieved by the control effort for the modes.
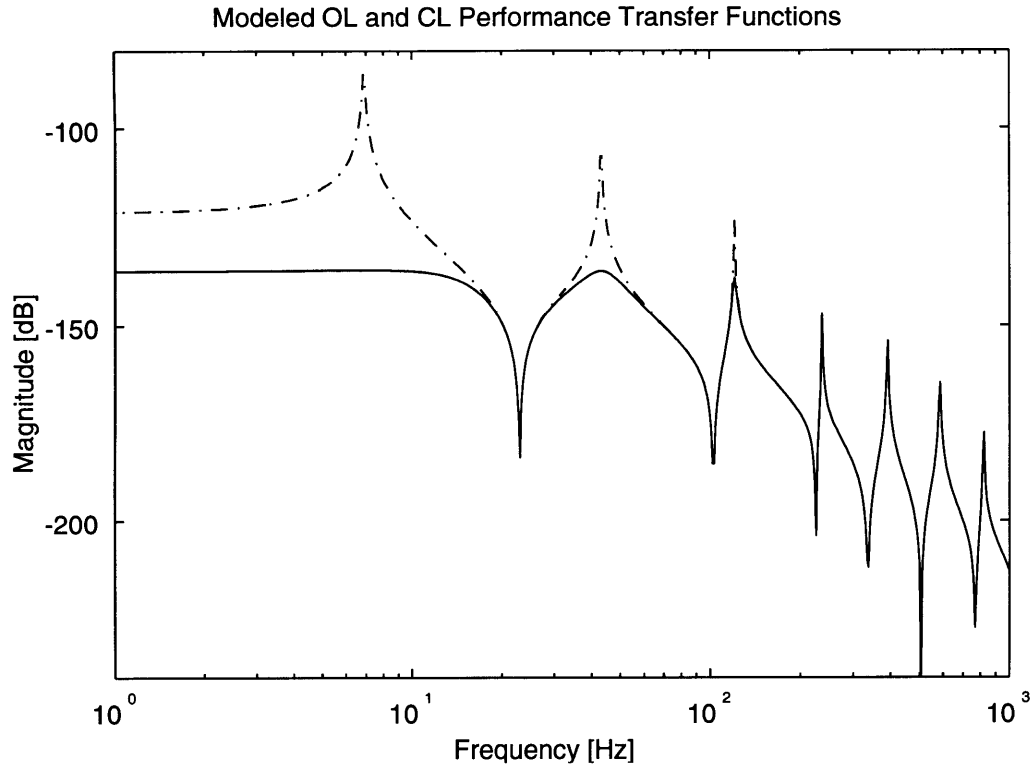
**Figure 4.9:** Modeled open-loop (dash-dotted) and closed-loop (solid) performance output transfer functions for the LQR differenced-displacement control design.

The kernels can be thought of as an optimal combination of modal sensors [4, 5]. The amount that each particular mode shape contributes to the kernel is related to the level that of vibration control achieved for that mode. The control effort for each mode can be divided into two parts: stiffening and damping. The stiffening achieved by the control effort is related to that mode's contribution to the curvature kernel, and the damping achieved is related to that mode's contribution to the curvature rate kernel.

For the differenced-displacement regulator, the ratio of damping-to-stiffening is different for each mode. The modeled open and closed-loop performance output transfer functions are shown in Figure 4.9. In particular, the closed-loop damping-to-stiffening ratios achieved by the control effort for the

first and second modes are completely different. The different ratios of dampening-to-stiffening correspond to the different ratios of first-to-second mode shapes in the curvature and curvature rate kernel predictions, thus the dissimilarity.

## 4.6   EXPERIMENT 2: RESULTS

Two PVDF sensors were constructed with the kernel shapes etched on their electrodes. The transfer functions of the sensors were measured. It was observed that the measured transfer functions differed from the wave model predictions. There was a new form of error present in the data that was not seen in the first experiment. The plots of the curvature and curvature rate sensor transfer functions versus their wave model predictions are shown in Figure 4.10.

The errors start at about 100 Hertz in the measured data. There is a shallow valley between the second and third modes of the measured transfer function with no appreciable phase loss. In contrast, the modeled transfer functions from the wave models have a lightly-damped, minimum phase pair of zeros located between the second and third mode. The model predicts the presence of lightly-damped, minimum phase zero pairs between all the modes. Most of the zeros in the measured transfer function data appear as if they have been "washed out" by noise. This is not the case, since the data does not appear to be corrupted by noise.

The kernel shapes derived for the sensors electrodes were also validated. A wave model of the beam could generate the loop transfer function (LTF) for the LQR control design with the kernels. This wave model prediction matched the LTF generated from a high-order finite element model, and is shown in Figure 4.11. It was therefore assumed that the predicted kernels were correct,
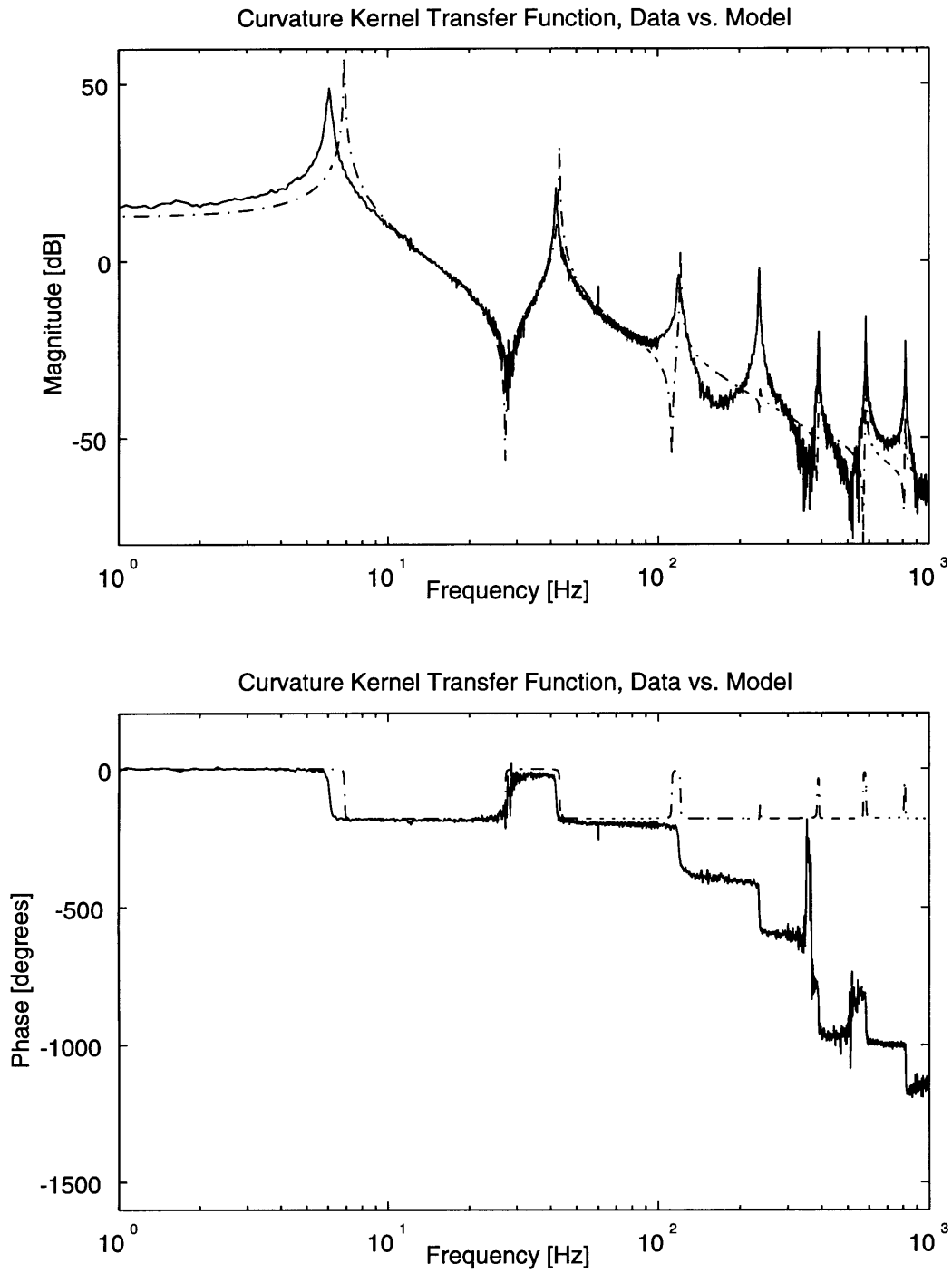
**Figure 4.10a:** Modeled (dash-dotted) and measured (solid) curvature kernel transfer functions.
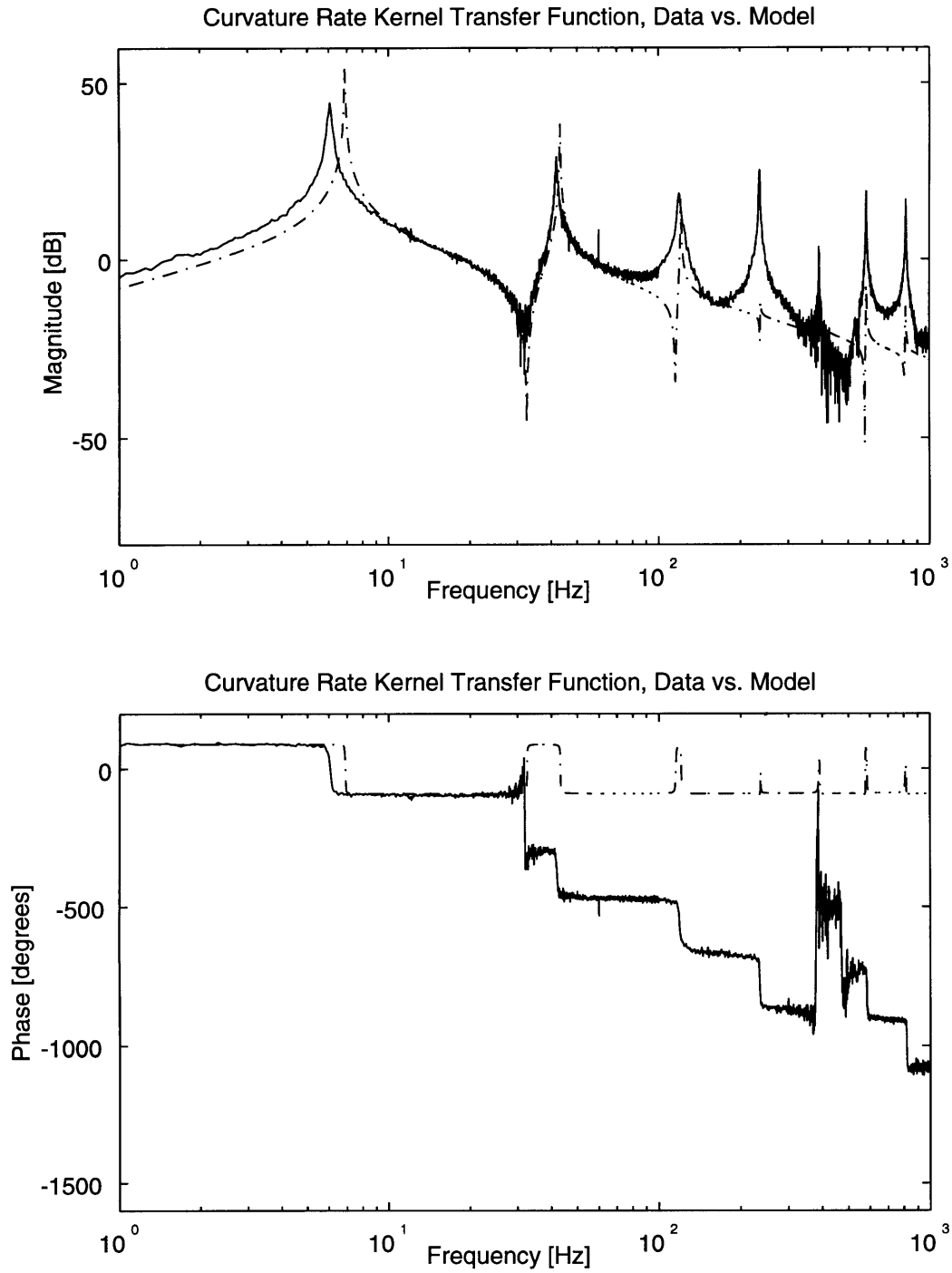
**Figure 4.10b:** Modeled (dash-dotted) and measured (solid) curvature rate kernel transfer functions.
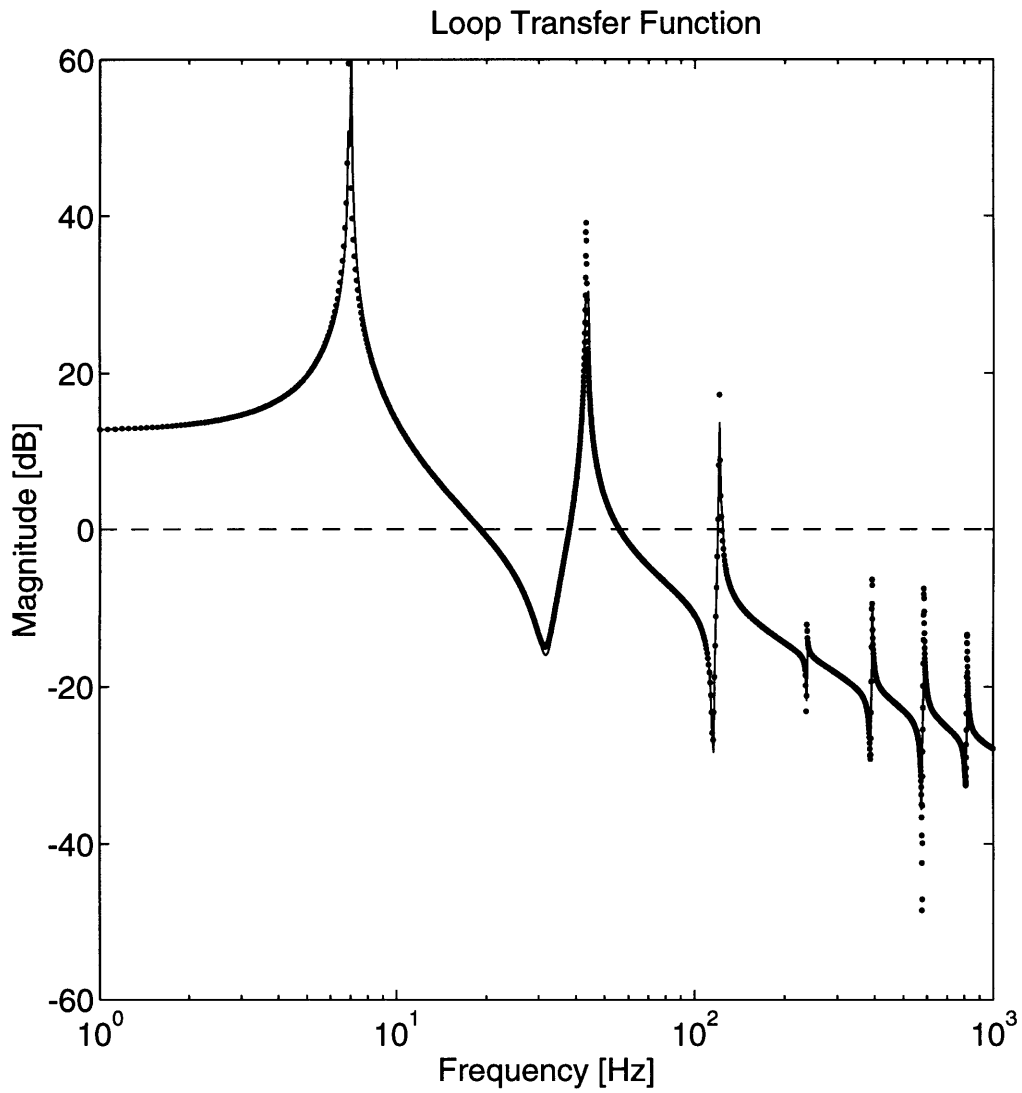
**Figure 4.11:** Comparison of wave mode LTF derived from the kernel predictions (dotted) versus LTF generated from high-order finite element model (solid).

and that some unmodeled fabrication or environmental error existed in the data.

There were several possibilities for the presence of the error. It was possible that the sensors were slightly mis-aligned on the beam. It was possible that slight errors in the fabrication of the electrode shape could significantly change the output behavior of the sensors. Also possible was the presence of discontinuities or breaks in the PVDF. It was observed that differencing the signals from sensors with these kernel shapes did not reduce or remove the erroneous behavior.

The wave model of the beam was used to simulate the effects of different types of fabrication errors. The kernel predictions were deliberately altered, and the wave model predicted the transfer functions for sensors with the altered shapes. A synopsis of the different types of fabrication errors that were simulated are shown in Figure 4.12. Part (b) represents the simulation of sensors with discontinuities, Part (c) and (d) represents the simulation of axially mis-aligned sensors, and Part (e) represents simulations done for poorly etched sensors. These and other types of fabrication errors were modeled. Unfortunately, no exact match in behavior to the measured transfer function data was found.

All the simulation evidence suggested that the unmodeled effects were present in the test bed environment, and not in the fabrication of the sensors. It was possible that the sensors were accurately made, but that the test bed conditions, specifically those at the root, the tip, and the epoxy layer, were not ideal. The combination of the metal blocks used for the clamp and the bench on which the experiment was performed was not a completely rigid system, and the force actuator did not really produce a point force, but a distributed load over a small area. Measurements of the epoxy layers showed them to be about 1 mil (25.4 μm) thick on average, which was assumed to be negligible (since the film

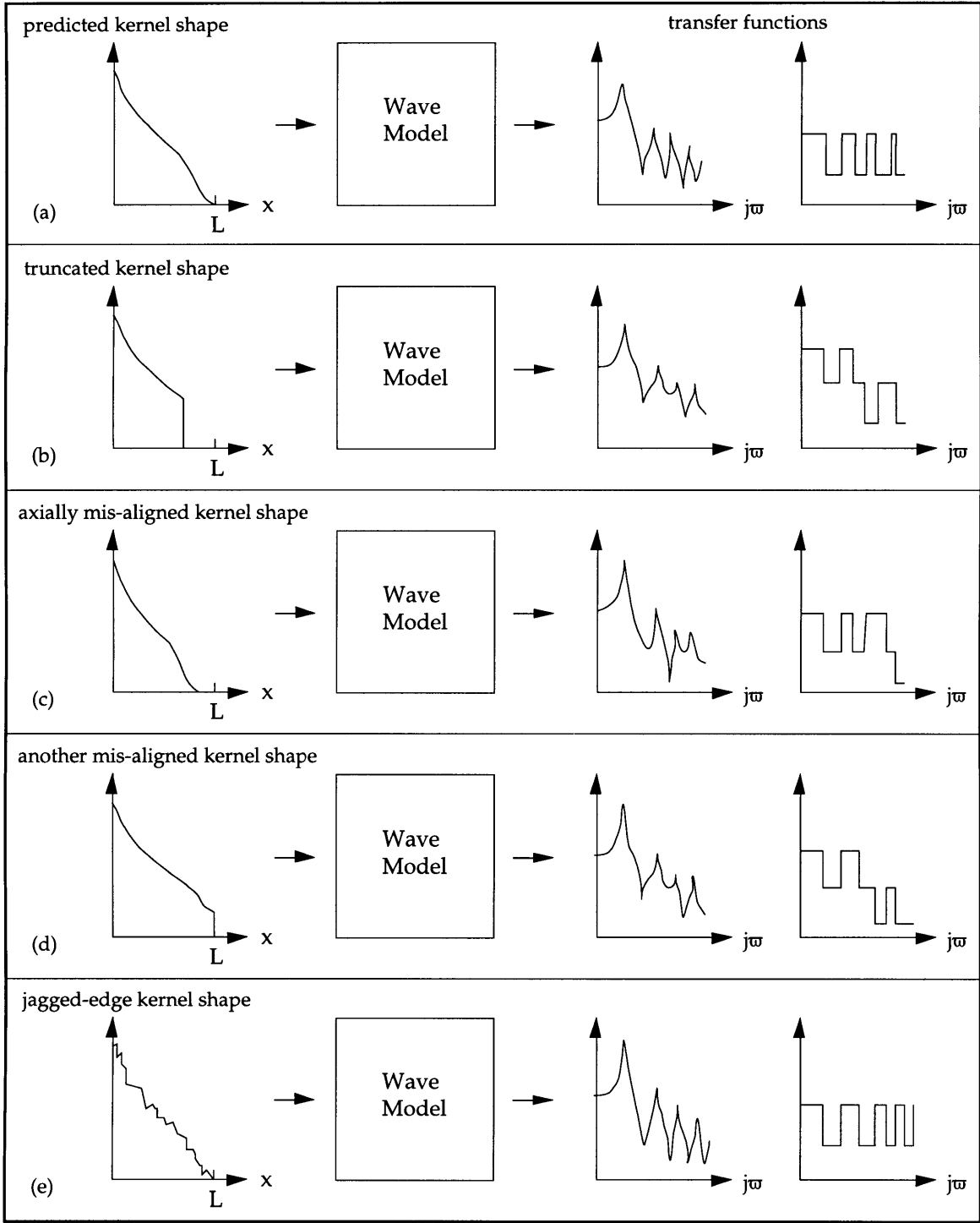**Figure 4.12:** Illustration of the modeling of possible fabrication errors.

thicknesses were 28 μm and 52 μm, and the beam thickness was 3,175 μm). No modeling of the sensor-epoxy-beam interaction was performed to confirm the assumption. To verify the distinction between fabrication and environmentally-caused errors, the experiment was repeated many times, constructing sensors for different beams. Much care and attention was taken in perfecting the fabrication process of the sensors. The same clamp and force actuator from the first experiment were used, and effort was made to provide thin, uniform epoxy layers less than or equal to 1 mil. Unfortunately, the transfer function data for the repeated experiments showed results similar to the prior data.

A new approach was needed to expose the non-idealities in a quantitative manner, accommodate for them, and allow for the successful implementation of the control design. Rectangular-shaped sensors were used in a new design attempting to accomplish these goals. In working with the PVDF film, it was observed that sensors with rectangular-shaped electrodes were very well behaved. The measured transfer function from the differenced signal of two of rectangular sensors placed on opposite sides of the beam could be accurately modeled. The reliability of the rectangular-shaped sensors was exploited to circumvent the problems seen with the kernel-shaped sensors.

# Chapter 5

# Rectangular Array Experiments

## 5.1  METHODOLOGY FOR RECTANGULAR ARRAY EXPERIMENTS

An array of ten rectangular sensor-elements located along the length of a cantilevered beam was constructed in the following manner. Two rectangular pieces of PVDF film were placed on each side of a cantilevered beam, covering the entire surfaces. Both pieces were divided into ten, equally-sized, rectangular segments. The divisions were made by etching thin lines on the film electrodes. Each parallel pair of rectangular segments, located on opposite sides of the beam, formed a single sensor-element. The voltage outputs from the pair were differenced to remove any noise common to both while amplifying the part of the signal related to the bending of the beam. The voltage signals were proportional to the average surface strain rate over the area covered by the elements. The setup of the beam is shown in Figure 5.1.

The ten sensor-element array was advantageous in three ways. First, it was hypothesized that the problems seen with the kernel-shaped sensors in Chapter 4 were possibly due to local non-idealites located at the root or the tip of the beam. The segmentation of the PVDF along the length presented an opportunity to attempt to pin-point the source of the non-idealities, assuming that they truly were a function of location. A wave model could be used to generate transfer functions from the tip disturbance force to each sensor-element
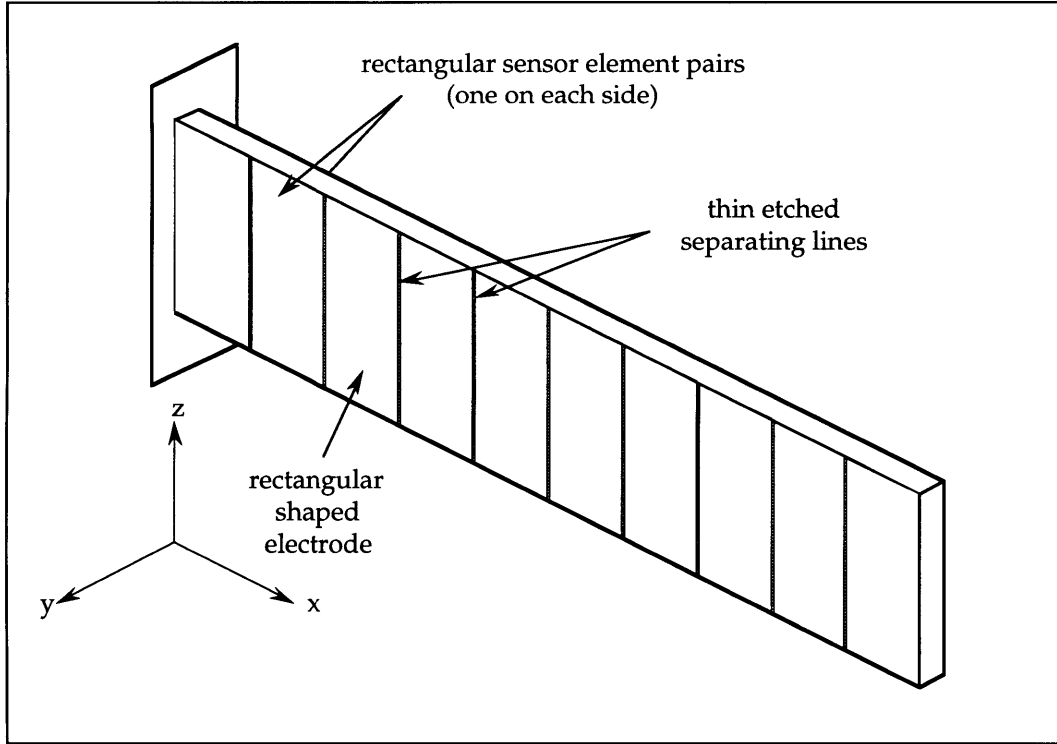
**Figure 5.1:** Illustration of a ten rectangular sensor-element array on a cantilevered beam. A single sheet of PVDF was placed on either side of the beam. The rectangular shapes were etched into the electrode surface.

signal, and the modeled results could be compared to the measured data to reveal any differences.

Secondly, the elements could be used in unison to approximate different transfer functions in the following manner. A linear combination of the sensor-element transfer functions multiplied by a set of gains could produce an estimate of some desired, nominal transfer function $G_{nom}$. The estimate generated from the sensor-element array can be represented by

$$G_{fit}(j\omega) \;=\; \sum_{p=1}^{10} g_p H_p(j\omega) \;\cong\; G_{nom}(j\omega), \tag{5.1}$$

where $H_p$ represents the transfer function for sensor-element $p$, and the term $g_p$

88

represents the electronic gain applied to element $p$. The transfer function $H_p$ is proportional to the average strain rate over the area covered by the electrodes. The term $G_{fit}$ is the estimate transfer function. It is an approximation to the desired, nominal transfer function $G_{nom}$. The accuracy of the approximation is dependent on the choice of the gain vector $g$.

Lastly, the approach was advantageous in that the rectangular array could generate estimates of many other transfer functions as well, each corresponding to a different set of gains. With the proper gains, the array could be used to implement a feedback control design. This is achieved by using a linear combination of the sensor-element transfer functions to estimate the desired loop transfer function (LTF) associated with that control design. In particular, the rectangular array could be used to implement the LQR differenced-displacement regulator design from Chapter 4. To test for the practicality of the rectangular array design, the gains needed to implement the differenced-displacement regulator were calculated and applied to the array in an experiment.

The approach to estimating the LTF with the rectangular array is as follows: a gain vector $g_{cker}$ is determined to make an estimate $G_{fit\ 1}$ of the curvature kernel transfer function $G_{cker}$. The estimate is represented by Equation 5.2.

$$G_{fit1}(j\omega) \quad = \quad \sum_{p=1}^{10} g_{c\,ker_p} H_p(j\omega) \frac{1}{j\omega} \quad \cong \quad G_{c\,ker}(j\omega) \qquad (5.2)$$

A different gain vector $g_{crker}$ is determined to make an estimate $G_{fit\ 2}$ of the curvature kernel transfer function $G_{crker}$. This estimate is represented by Equation 5.3.

$$G_{fit2}(j\omega) \quad = \quad \sum_{p=1}^{10} g_{cr\,ker_p} H_p(j\omega) \quad \cong \quad G_{cr\,ker}(j\omega) \qquad (5.3)$$

The two transfer functions $G_{cker}$ and $G_{crker}$ correspond to the frequency behavior of distributed curvature sensors with curvature and curvature rate kernel-shaped electrodes, respectively. The sum of the two transfer functions $G_{cker}$ and $G_{crker}$ form the desired LTF for the LQR control design. The approximation of the LTF made by the array is represented by

$$G_{fit1}(j\omega) + G_{fit2}(j\omega) \equiv \sum_{p=1}^{10} \left( \left( g_{cker_p}/j\omega \right) + g_{crker_p} \right) H_p(j\omega). \tag{5.4}$$

The process is similar to approximating the continuous kernel shapes with a series of step functions, as illustrated by Figure 5.2. Each step in the figure represents a different sensor-element located along the length. The different magnitude levels of the steps correspond to the electronic gains applied to the sensor-element signals. Ideally, a single PVDF sensor with this staircase-shaped
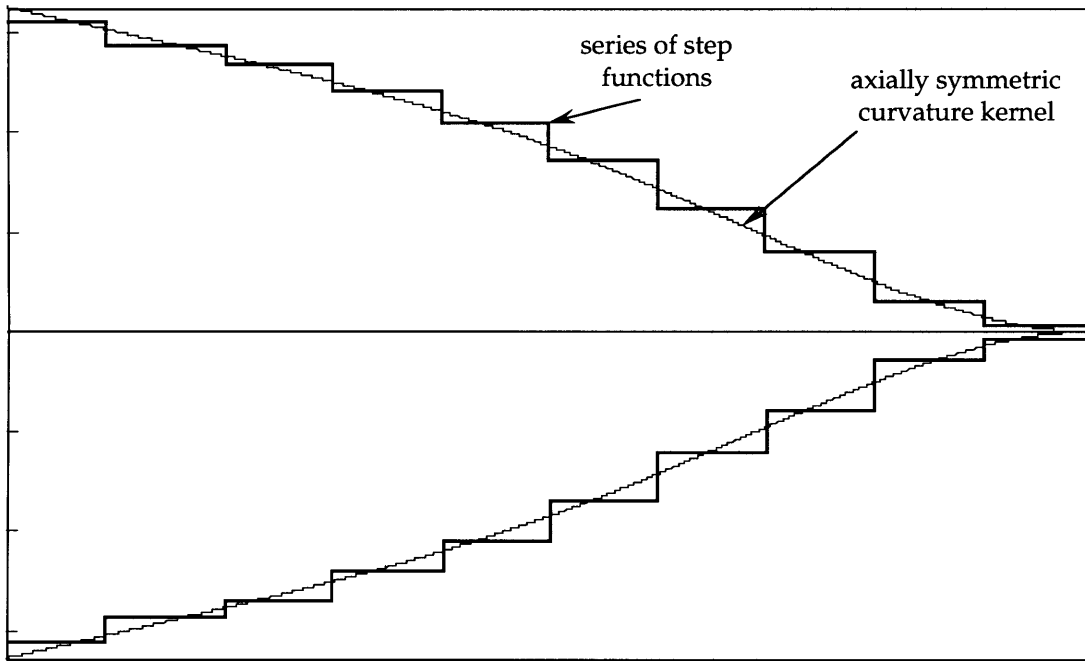


**Figure 5.2:** Illustration of an approximation of a curvature kernel shape with a series of step functions.

function etched on its electrode could achieve the same behavior. The array of elements is a better design choice because it allows for adjustments. Also, each sensor-element in the array has the same sensitivity to the surface strain rate over the step lengths.

## 5.2 GAIN DETERMINATION TECHNIQUES

There are two possible methods for determining the gains needed to implement the control design. Method 1 is based on the shape of the continuous kernels. The gain for each sensor-element is found by picking the median value of the curvature kernels over the area covered by the element. This is illustrated by Figure 5.3. A gain vector $g_{cker}$ is determined based on the curvature kernel along with a vector $g_{crker}$ based on the curvature rate kernel.
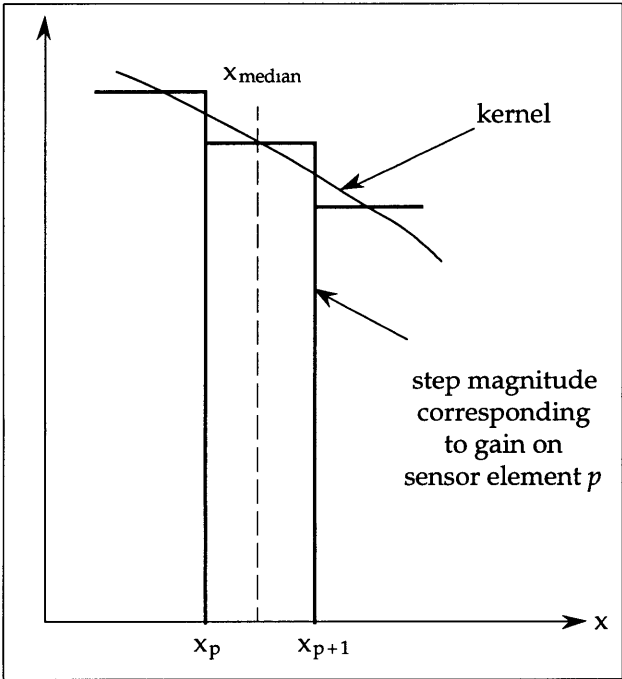
**Figure 5.3:** Illustration of gain selection technique for Method 1. The magnitude of each gain $g_p$ was chosen to be the median value of the kernel over that segment.

91

Method 2 is based on the continuous kernel transfer functions. The objective of this method is to minimize the logarithmic error between the desired loop transfer function (LTF) and that achieved using the rectangular sensor array. This logarithmic error is represented by

$$E_o(j\varpi) = \log\big(G_{cker}(j\varpi) + G_{crker}(j\varpi)\big) - \log\big(G_{fit1}(j\varpi) + G_{fit2}(j\varpi)\big)$$

$$= \log\big(G_{LTF}(j\varpi)\big) - \log\big(G_{fit1}(j\varpi) + G_{fit2}(j\varpi)\big)$$

$$= \log\left(\frac{G_{LTF}(j\varpi)}{G_{fit1}(j\varpi) + G_{fit2}(j\varpi)}\right)$$

$$= \log\left(\frac{G_{LTF}(j\varpi)}{\sum_{p=1}^{10}\left(\left(g_{cker_p}/j\varpi\right) + g_{crker_p}\right)H_p(j\varpi)}\right). \tag{5.5}$$

where $G_{LTF}$ symbolizes the desired LTF. The error $E_o$ varies with the choice of curvature and curvature rate gains $g_{cker}$ and $g_{crker}$. By employing a non-linear least squares approach [16], the error $E_o$ is minimized. The minimization process varies the gains to determine the lowest value of the error $E_o$. This value is found with the optimal choice of the two gain vectors $g_{cker}$ and $g_{crker}$. The logarithm of the error is used because it makes the minimization process sensitive to the zeros of the transfer function. The structure of this minimization technique is covered thoroughly in Ref. 16.

When employing this method, it is actually convenient to determine the two gain vectors separately. The LTF is divided into two parts: a curvature kernel transfer function $G_{cker}$, and a curvature rate transfer function $G_{crker}$. Two logarithmic errors are defined, one for the determination of each gain vector. The two errors are represented by Equation 5.6.

$$E_{O_{cker}}(j\varpi) = \log\big(G_{c\,ker}(j\varpi)\big) - \log\left(\sum_{p=1}^{10} g_{c\,ker_p} H_p(j\varpi)\frac{1}{j\varpi}\right)$$

$$= \log\left(\frac{G_{c\,ker}(j\varpi)}{\sum\limits_{p=1}^{10} g_{c\,ker_p} H_p(j\varpi)\frac{1}{j\varpi}}\right) \qquad (5.6a)$$

$$E_{O_{crker}}(j\varpi) = \log\big(G_{cr\,ker}(j\varpi)\big) - \log\left(\sum_{p=1}^{10} g_{cr\,ker_p} H_p(j\varpi)\right)$$

$$= \log\left(\frac{G_{cr\,ker}(j\varpi)}{\sum\limits_{p=1}^{10} g_{cr\,ker_p} H_p(j\varpi)}\right) \qquad (5.6b)$$

The errors $E_{O_{cker}}$ and $E_{O_{crker}}$ are minimized separately, yielding the gains needed to implement the control design.

Both methods can generate a set of curvature and curvature rate gains $g_{cker}$ and $g_{crker}$ needed to construct estimates of the curvature and curvature rate kernel transfer functions from the rectangular array transfer functions. The methods were applied to the wave model rectangular array transfer functions first, and then to the measured data from the beam.

## 5.3  MODELED AND EXPERIMENTAL RESULTS

Figure 5.4 shows the results of applying Method 1 to the modeled sensor-element transfer functions. The errors between the desired LTF and the estimate increased with frequency, but they were minimal. The gains were not de-stabilizing, because the estimate captured the alternating pole/zero structure of the desired LTF. There was still room for improvement. The gains found from
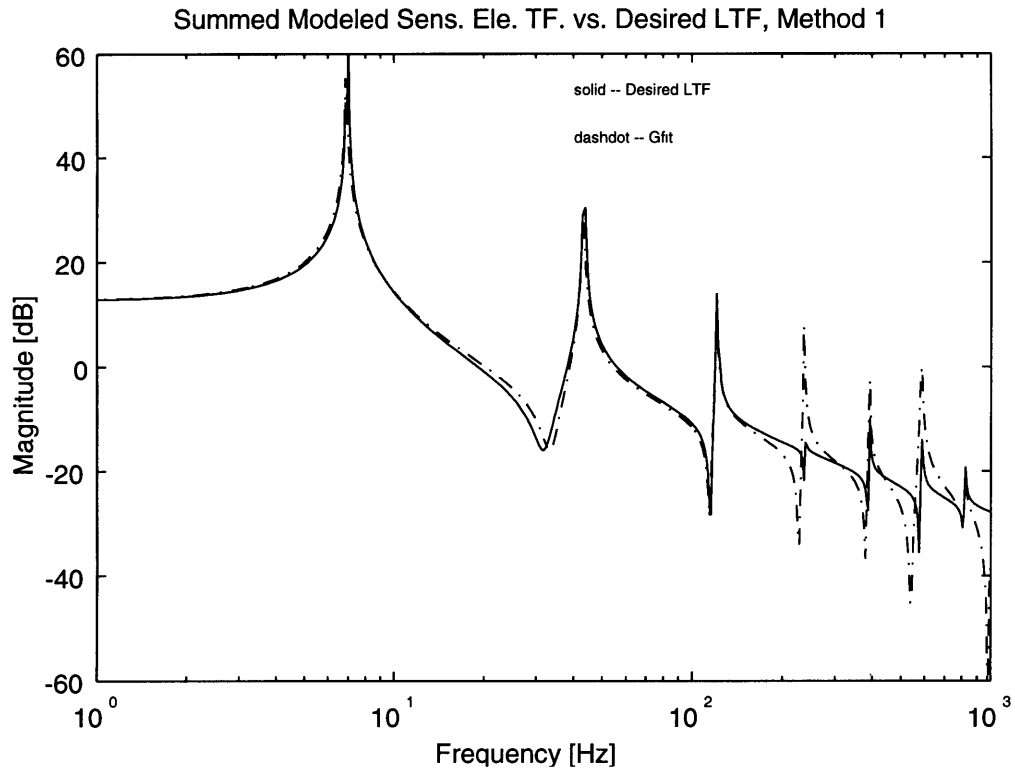
**Figure 5.4:** Linear combination of the modeled sensor-element transfer functions (dashed-dotted) versus the desired loop transfer function (solid). Gains obtained with Method 1.

Summed Modeled Sens. Ele. TF. vs. Desired LTF, Method 2
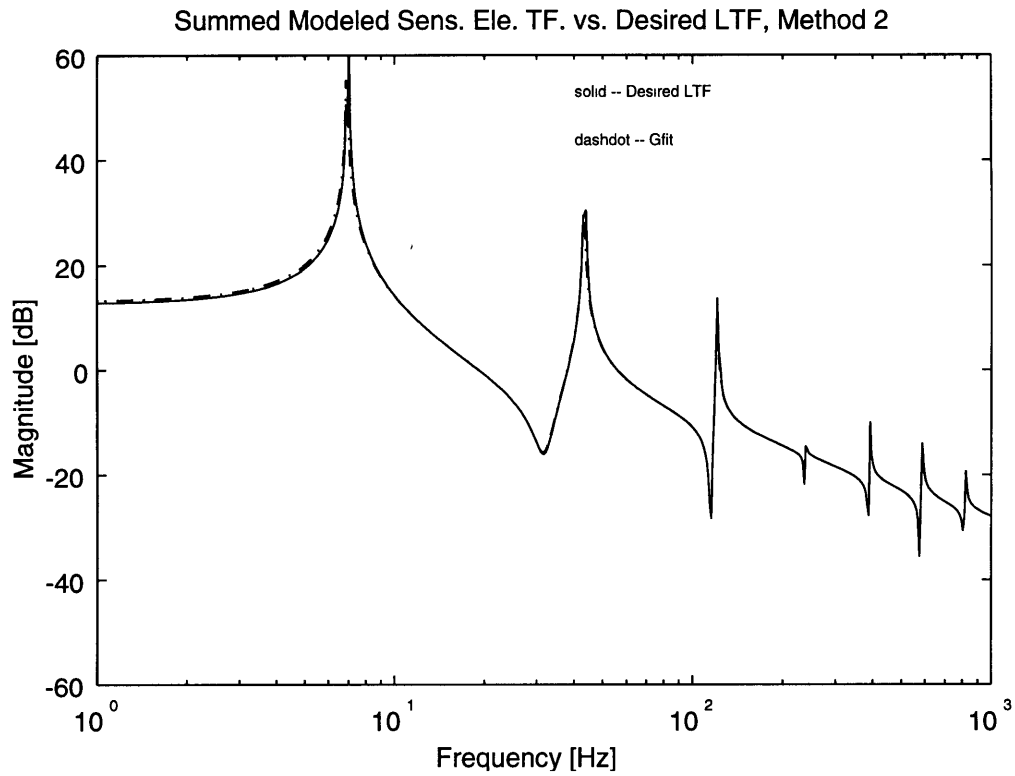
**Figure 5.5:** Linear combination of the modeled sensor-element transfer functions (dashed-dotted) versus the desired loop transfer function (solid). Gains obtained with Method 2.
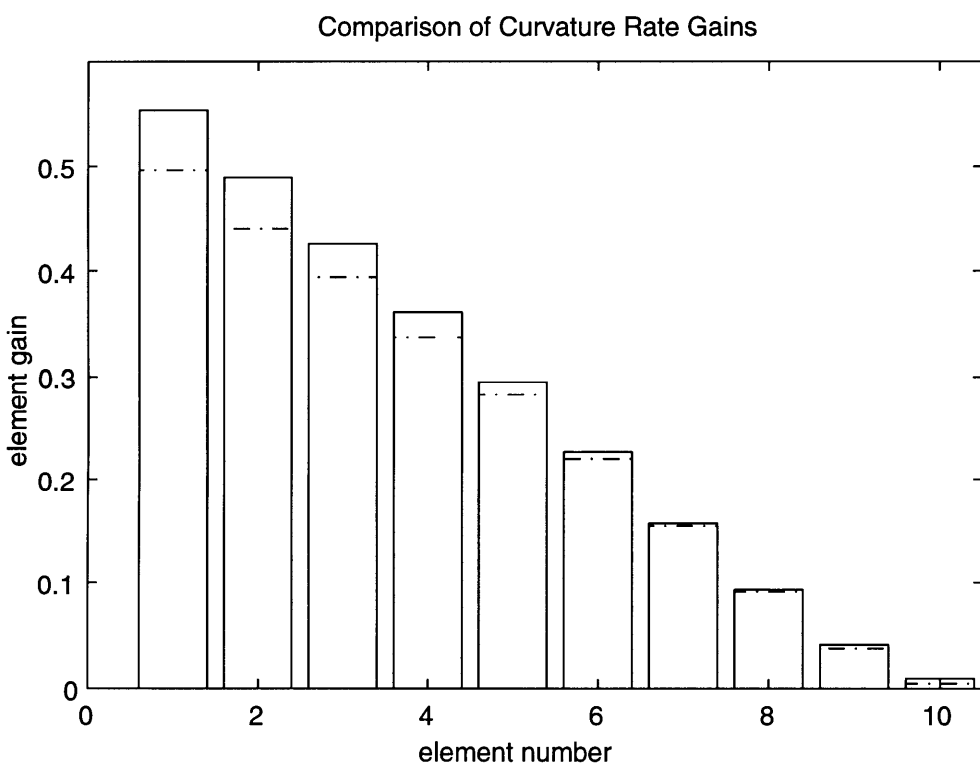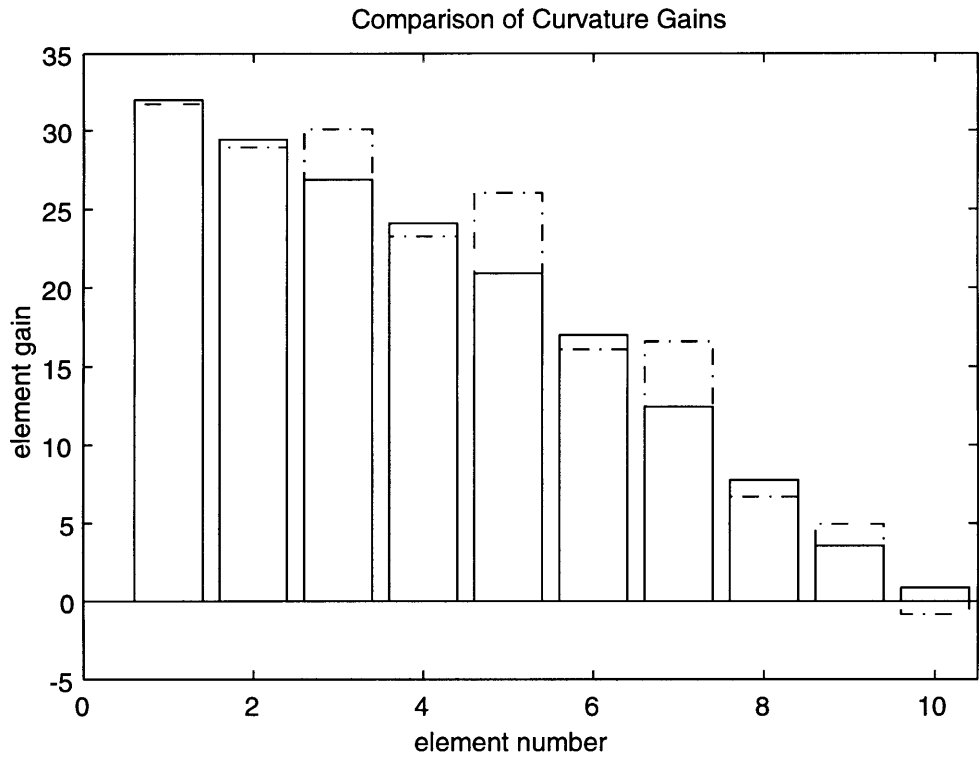
**Figure 5.6:** Comparison of gains for methods 1 (solid) and 2 (dash-dotted).

Method 1 could be used as an initial guess for Method 2. Figure 5.5 shows the results for applying Method 2 in this manner. A better match of the desired LTF and the estimate $G_{fit\,1} + G_{fit\,2}$ was made with this method. The gains for the two methods are compared in Figure 5.6. The largest gains are for sensor-element 1, and the gains generally decrease for each consecutive element. For both methods, the staircase patterns formed by the gains resemble discretized estimates of the continuous curvature and curvature rate kernel shapes. The continuous kernels decrease in magnitude as they progress along the length of the beam, as seen in Figure 4.8. The predicted kernel transfer functions also decrease in magnitude with increasing frequency, as seen in Figure 4.10. It is assumed for both methods that the estimates $G_{fit\,1}$ and $G_{fit\,2}$ also decrease in magnitude with increasing frequencies not shown, based on the staircase patterns observed for the gains.

In the experiment, each sensor-element transfer function was measured over the bandwidth of 0 to 1000 Hertz. A computer program produced a prediction of the estimate $G_{fit\,1} + G_{fit\,2}$, given the desired gains $g_{cker}$ and $g_{crker}$ along with the measured transfer functions $H_p$. The summed data did not match the modeled rectangular array behavior. The results for the Method 1 and Method 2 gains are shown in Figures 5.7 and 5.8. The errors in the figures are similar to the errors seen with the kernel-shaped sensor data from Chapter 4. The individual transfer functions for each element were inspected.

The measured transfer functions versus their models for the first four elements are shown in Figure 5.9. There were three discrepancies seen between the measured data and the model. The first was a mis-modeling of the fundamental frequency. It was lower than its predicted value by about 14 percent. This type of error was observed with all the measured data from experiments using the magnetic non-contacting actuator. The proximity of the
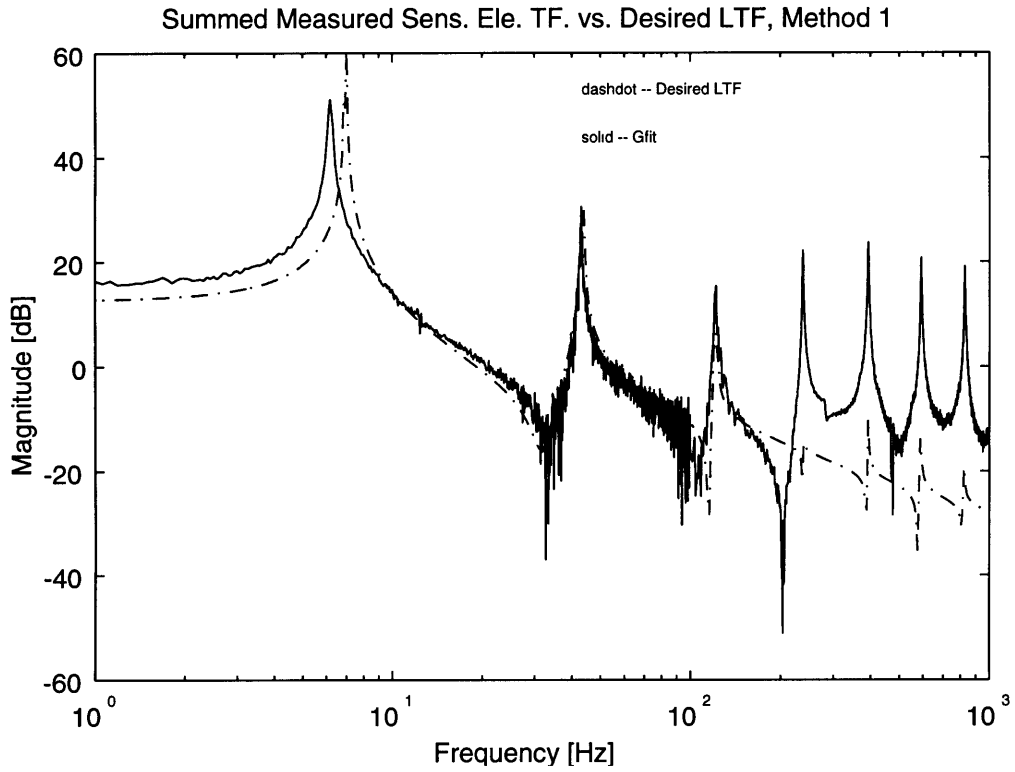
**Figure 5.7:** Linear combination of the measured sensor-element transfer functions (solid) versus the desired loop transfer function (dash-dotted). Gains obtained with Method 1.

Summed Measured Sens. Ele. TF. vs. Desired LTF, Method 2

dashdot -- Desired LTF

solid -- Gfit
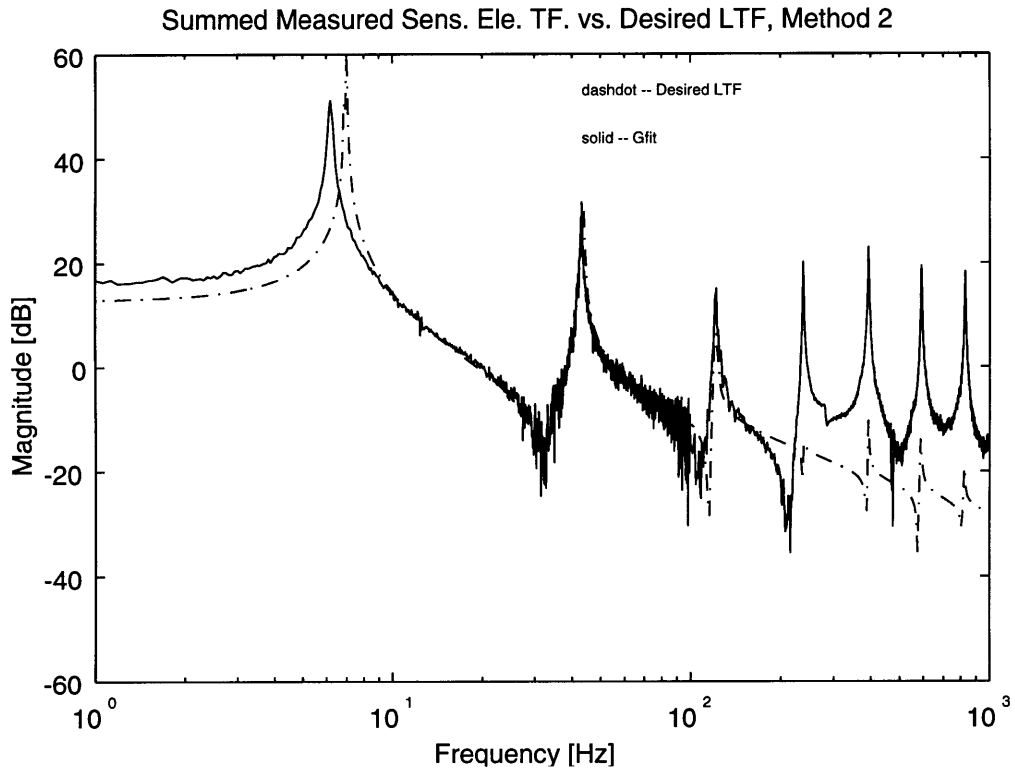
**Figure 5.8:** Linear combination of the measured sensor-element transfer functions (solid) versus the desired loop transfer function (dash-dotted). Gains obtained with Method 2.

99
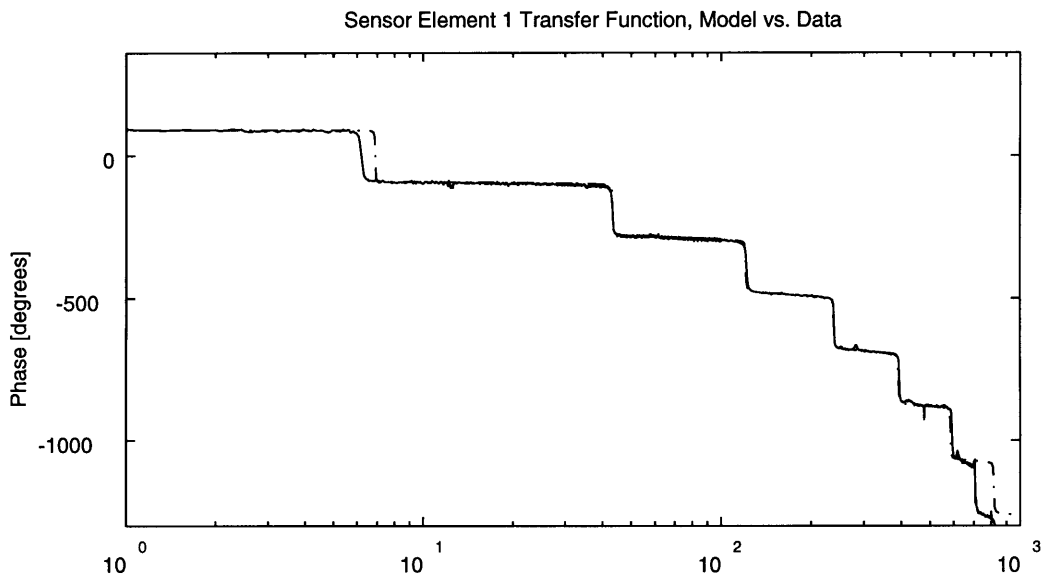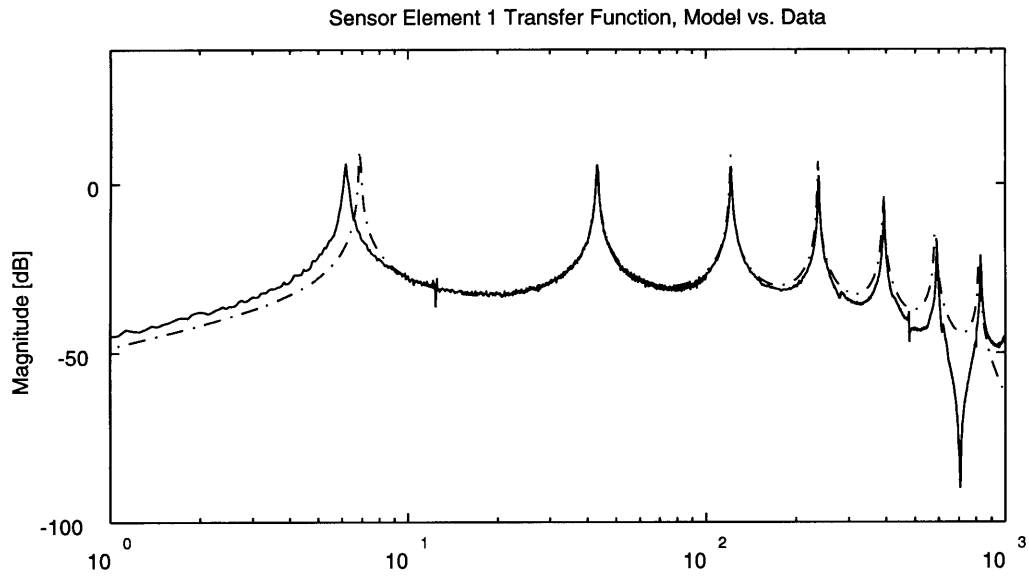
**Figure 5.9a:** Transfer function for sensor-element 1, measured data (solid) versus the wave model predictions (dash-dotted). A single pole roll-off at 250 Hertz has been added to the model to account for the actuator dynamics. Notice the additional unmodeled high frequency dynamics present in the magnitude plot.

Sensor Element 2 Transfer Function, Model vs. Data



Sensor Element 2 Transfer Function, Model vs. Data
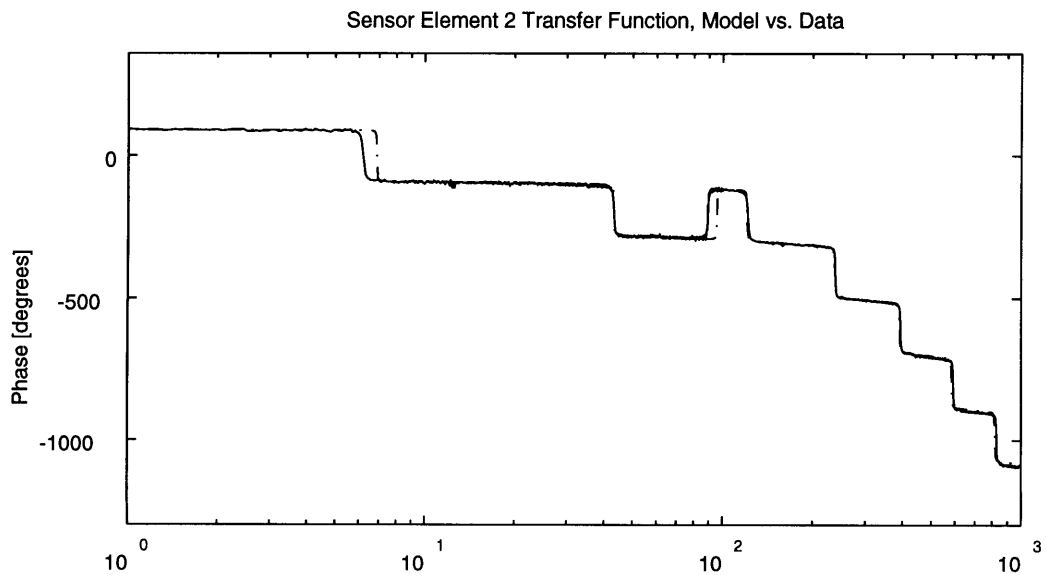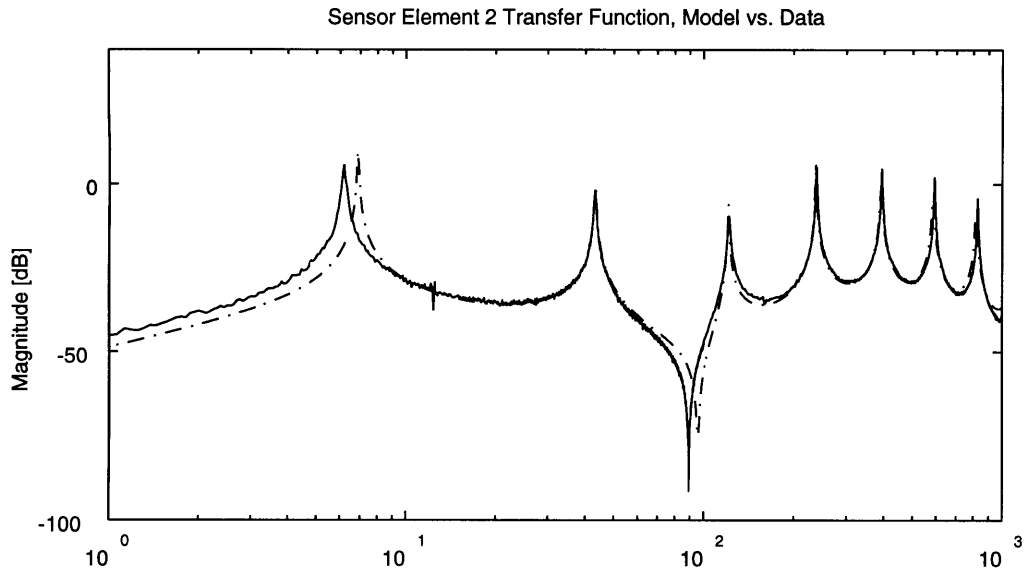


**Figure 5.9b:** Transfer function for sensor-element 2, measured data (solid) versus the wave model predictions (dash-dotted). A single pole roll-off at 250 Hertz has been added to the model to account for the actuator dynamics. There is particularly good agreement between the model and data for element 2 as well as for the other 8 consecutive elements.

Sensor Element 3 Transfer Function, Model vs. Data



Sensor Element 3 Transfer Function, Model vs. Data



**Figure 5.9c:** Transfer function for sensor-element 3, measured data (solid) versus the wave model predictions (dash-dotted). A single pole roll-off at 250 Hertz has been added to the model to account for the actuator dynamics. The second zero at about 450 Hertz is very lightly damped, accounting for the error in the phase.

Sensor Element 4 Transfer Function, Model vs. Data



Sensor Element 4 Transfer Function, Model vs. Data
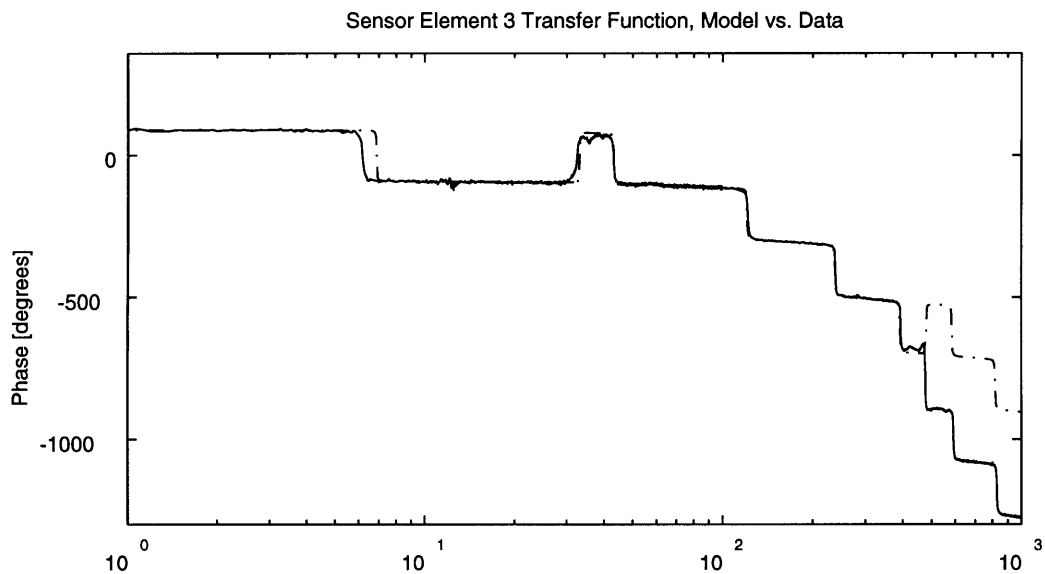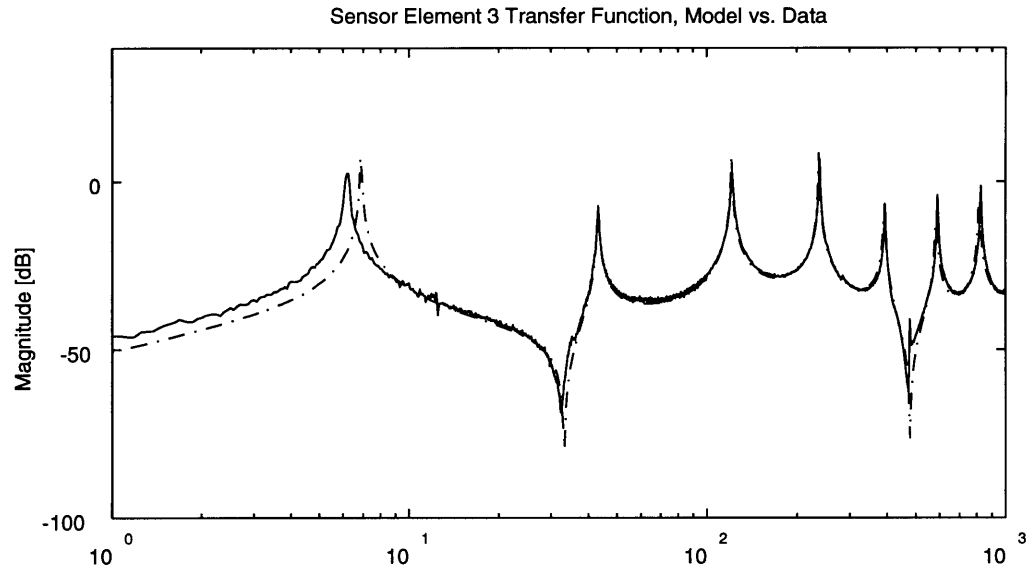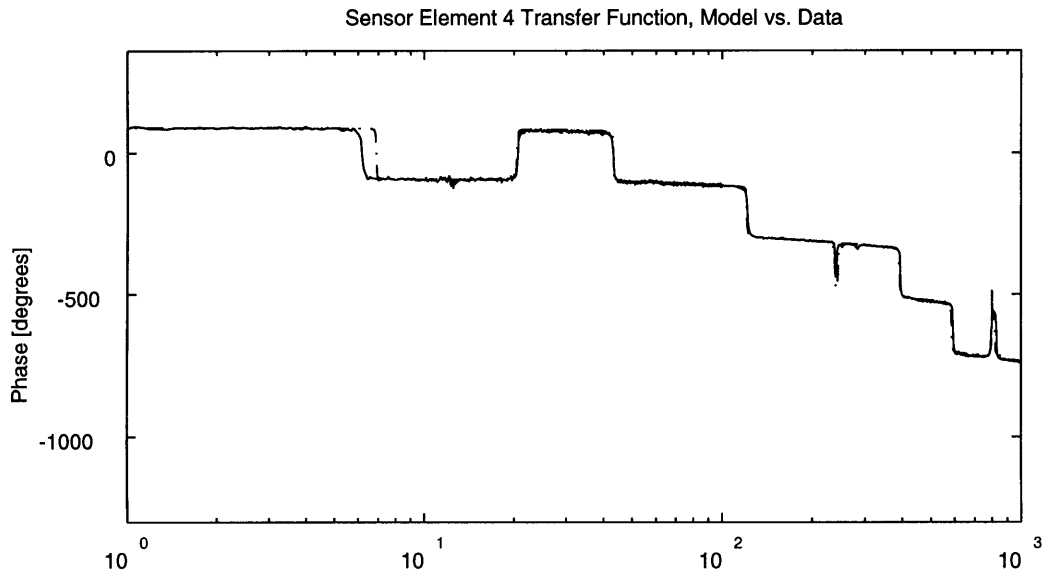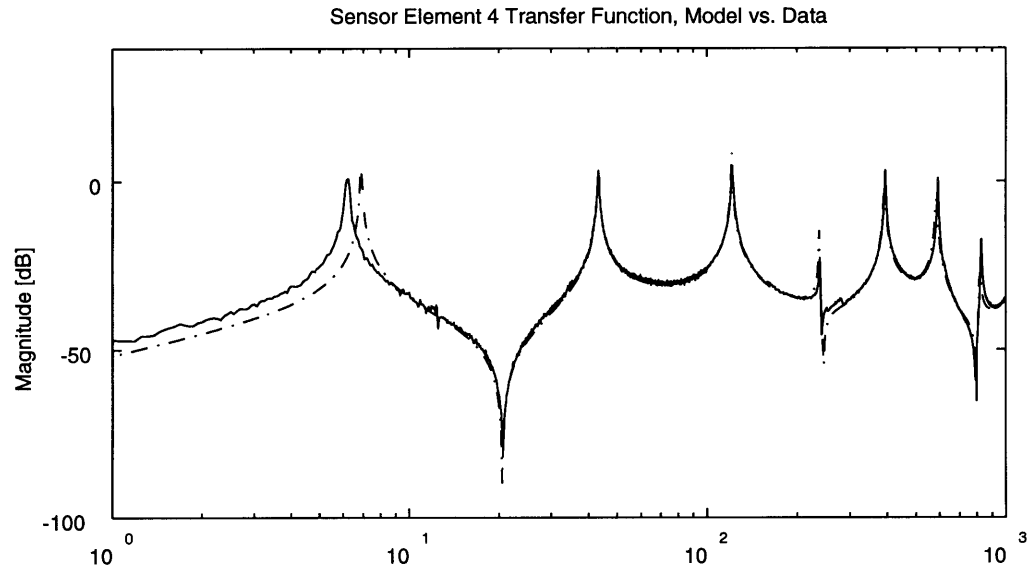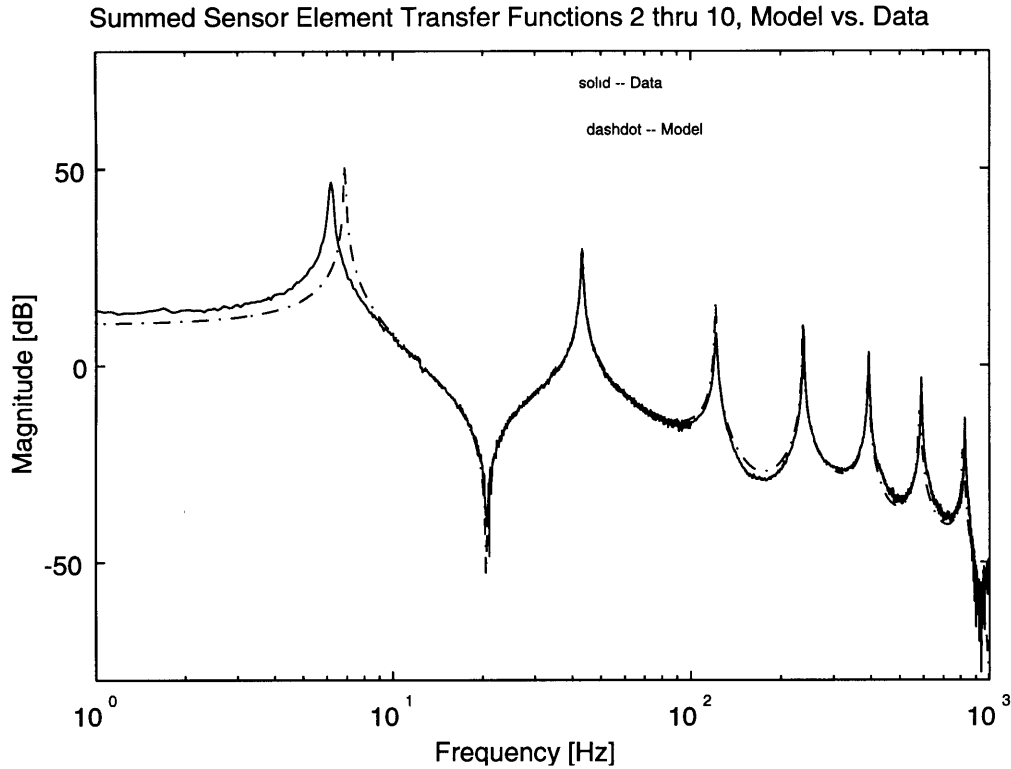


**Figure 5.9d:**    Transfer function for sensor-element 4, measured data (solid) versus the wave model predictions (dash-dotted). A single pole roll-off at 250 Hertz has been added to the model to account for the actuator dynamics.

actuator to the beam may have made the free end condition non-ideal, lowering the value of the first mode from its predicted value. Moving the actuator further away would reduce the percentage difference between the modeled and measured fundamental, but it would also reduce the available level of actuation. The reduced level of actuation would reduce the signal-to-noise ratio, which was not desired. The discrepancy was not caused by the PVDF sensors. The measurements of the transmission from the actuator to a tip accelerometer, taken before and after the PVDF sensors were applied to the beam, exhibited the same shift in the fundamental. The discrepancy was also not de-stabilizing and was therefore ignored.

The second was a decrease in phase and magnitude similar to a single pole roll-off present in all the measured transfer functions. The roll-off could also be accounted for by the actuator. It was a function of the inductor/resistor pole of the actuator and the distance between the magnet and the beam. Measurements of the transmission from the actuator to a tip accelerometer exhibited the same roll-off.

The third discrepancy was a further decrease in magnitude in the data for sensor-element 1. Element 1 was located adjacent to the root of the beam. There were also some higher frequency dynamics present in the data for sensor-element 1. This aberrant behavior could be due to non-ideal conditions present at the root of the beam. Such a suggestion was strengthened by the fact that linear combinations of the data from elements 2 through 10 could be modeled with acceptable accuracy. Figure 5.10 shows a sample linear combination of the data and modeled transfer functions for elements 2 through 10. The same roll-off has been added to each modeled element transfer function. It was possible that these same non-ideal conditions near the root of the beam were the cause of the errors seen with the kernel-shaped sensors in Chapter 4. To remove suspicions

104

Summed Sensor Element Transfer Functions 2 thru 10, Model vs. Data

solid -- Data

dashdot -- Model

Figure 5.10: Sample linear combination of the measured sensor-element transfer functions 2 through 10 (solid) versus the model (dash-dotted). The sample gains used were the curvature gains from Method 2.

of fabrication errors, another beam with a rectangular sensor array was created, and showed the same behavior.

Assuming that the test bed has remained within the Bernoulli-Euler beam modeling regime, the behavior seen by the model of sensor-element 1 should be the correct one. To use the Bernoulli-Euler beam assumptions, it is required that a beam be long and slender, and that the tip motion experienced be small compared to the length. The length-to-thickness aspect ratio was 192 to 1, and the length-to-average tip displacement was about 96 to 1. Accepted length-to-thickness aspect ratios for Bernoulli-Euler systems and some finite element codes have been as low as 5 to 1. Also, the signal from all the sensor-elements had

acceptable signal-to-noise ratios. The measured transfer functions did not appear to be corrupted by noise. Nonetheless, there was the undefined error hindering the success of the experiment.

To progress further, a method of compensating for the error was developed to allow the control design to be applied. It was possible to determine the difference between the desired LTF and the estimated LTF generated by the sensor-element transfer function measurements. This was possible given that the desired LTF had the same frequency resolution as the measured transfer functions. This quantitative difference could serve as the true system error. The error could be minimized using techniques similar to those employed in Method 2.

## 5.4 APPLYING METHOD 2 TO THE MEASURED DATA

The Method 2 gains used in generating the plots in Figure 5.5 came from minimizing an error between the desired LTF and the modeled sensor-element transfer functions, as was explained in Section 5.2. Since non-idealities caused the measured data to differ from the model, the true optimum gains needed to produce an implementable estimate of the desired LTF were re-calculated. They were found by applying Method 2 to the measured data. If the Method 2 gains from Section 5.2 were a good initial guess, the true system error could be minimized enough to provide a stable, implementable, closed-loop system. As with the model, there were actually two errors minimized separately: one associated with the curvature kernel transfer function and another associated with the curvature rate kernel transfer function.

There were two risks associated with the implementation of the true optimum gains. The first risk was that there were no guarantees that deviations

from the gains wouldn't cause the system to be unstable. The second risk was that there were no assurances about the behavior of the estimates at higher frequencies not observed. As shown in Figure 5.8, the desired LTF rolls off at -20 dB per decade with increasing frequency. The desired LTF continues to roll off even over the ranges not shown. This result is guaranteed for a Linear Quadratic Regulator control design [1, 8]. The LTF is also guaranteed to satisfy Nyquist stability criterion. There are no such guarantees for the rectangular array design, even with implementing the correct gains. The severity of the risks were exposed in the experiment.

Figure 5.11a shows the curvature kernel transfer function $G_{cker}$ versus the estimate $G_{fit\,1}$ and Figure 5.11b shows the curvature rate kernel transfer function $G_{crker}$ versus the estimate $G_{fit\,2}$. Figure 5.12 shows the desired LTF versus the sum of the two functions $G_{fit\,1}$ and $G_{fit\,2}$. The optimum gains are compared with their initial guesses in Figure 5.13. Over the observed bandwidth, the estimate $G_{fit\,1}$ + $G_{fit\,2}$ in Figure 5.12 will give a stable closed-loop system.

To reproduce this result in a real-time experiment, an adjustable, analog compensator was built. The initial sensor-element circuitry measured a voltage signal proportional the surface strain rate, represented by

$$V_p(t) \quad = \quad \frac{e_{31}h}{2C_f}\int_{l_p}^{l_{p+1}}F_p(x)\frac{\delta^3}{\delta x^2\,\delta t}\omega(x,t)\delta x \quad = \quad H_p\cdot V_{com}(t) \qquad (5.7a)$$

where

$$F_p(x) \quad = \quad 1 \qquad\qquad\qquad (5.7b)$$

and $V_{com}$ represents the input voltage signal for the tip actuator. The subscript $p$ denotes the different elements. The compensator multiplied each of different the

Linear Combination corresponding to smallest error e_cker
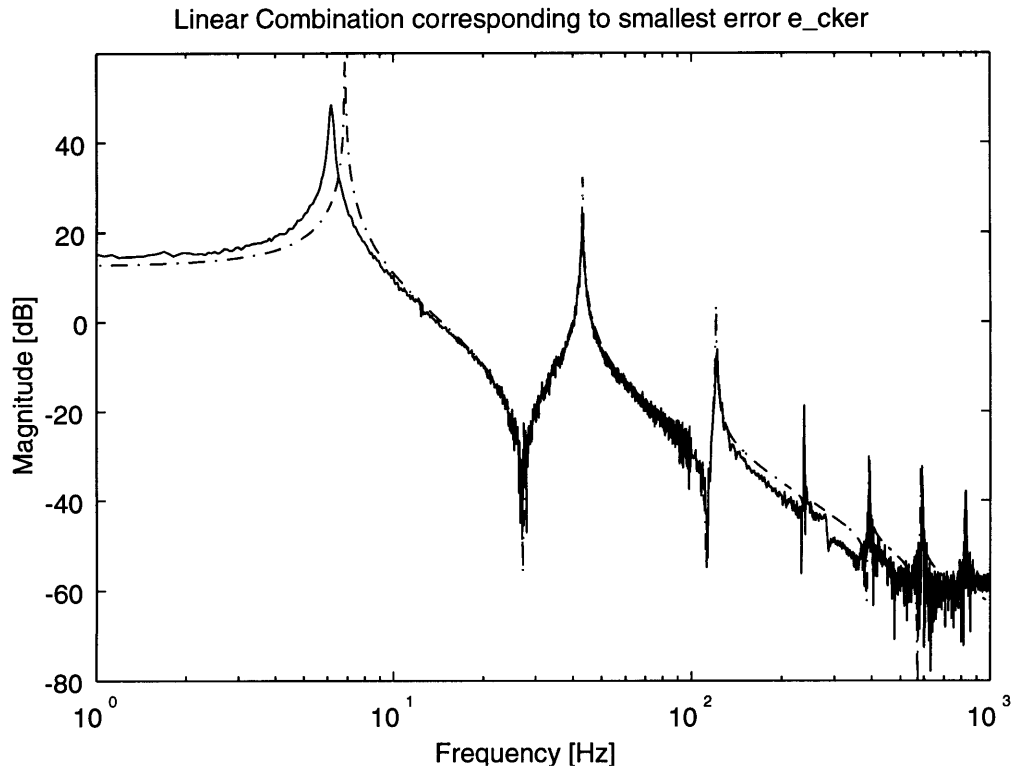
**Figure 5.11a:** The curvature kernel transfer function $G_{cker}$ (dash-dotted) versus the estimate $G_{fit\,1}$ (solid).
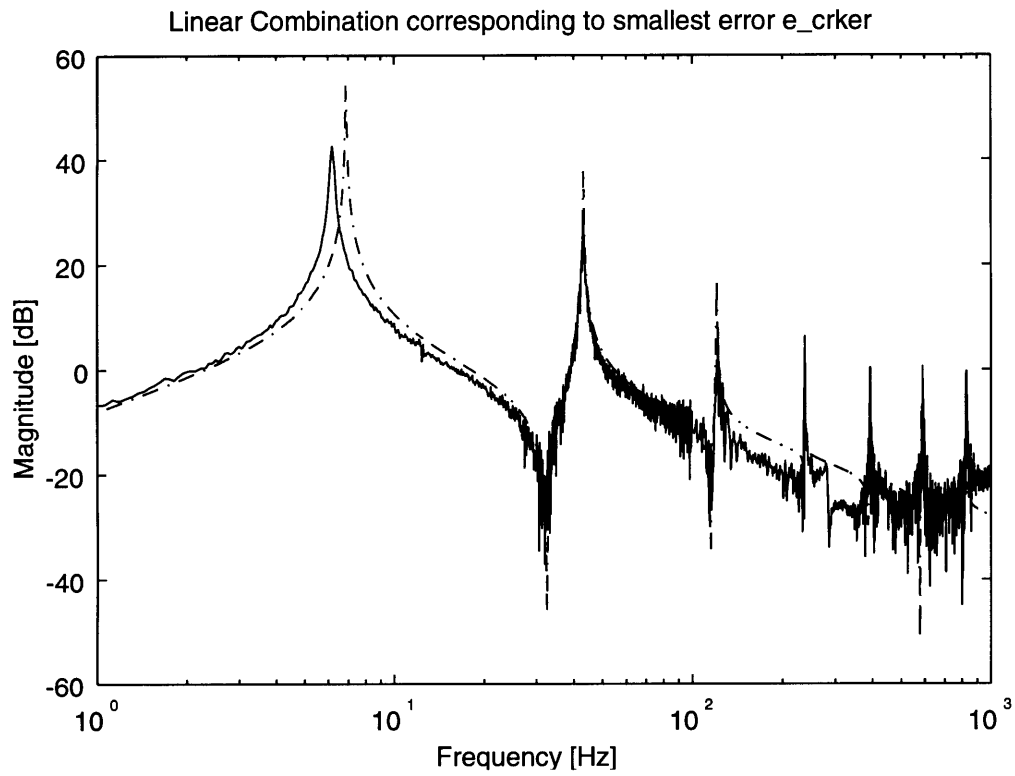
**Figure 5.11b:** The curvature kernel transfer function $G_{crker}$ (dash-dotted) versus the estimate $G_{fit\,2}$ (solid).

Desired LTF vs. estimated LTF generated from sensor array
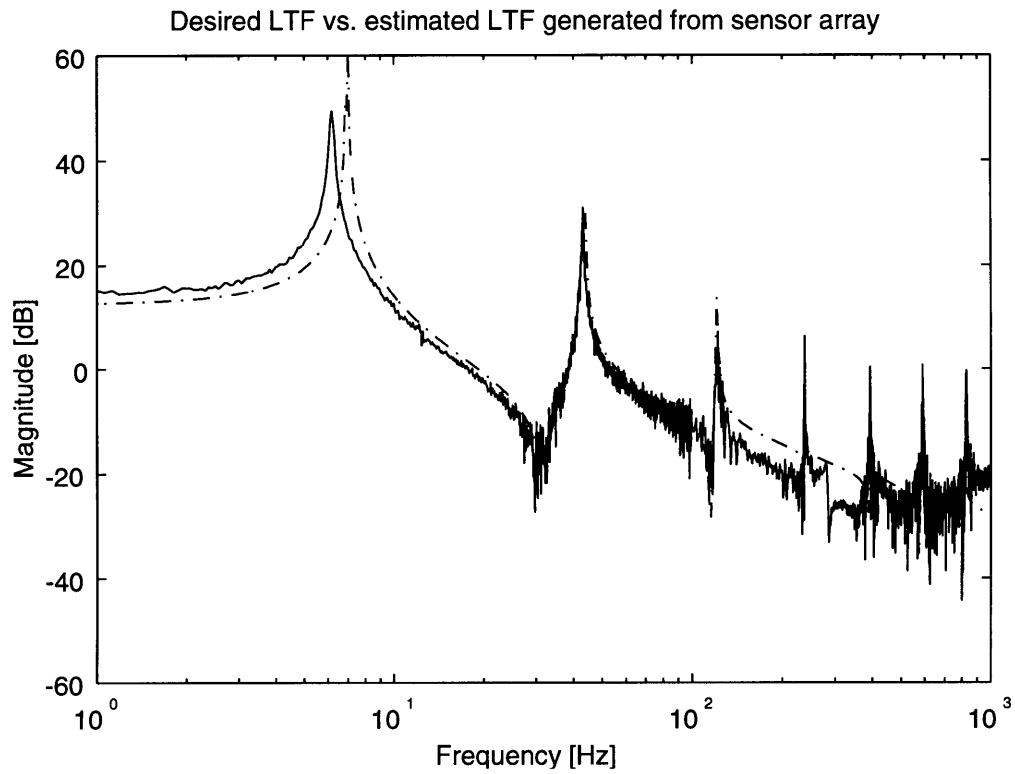
**Figure 5.12:** Desired LTF (dash-dotted) versus estimated LTF (solid) generated from sensor-element transfer functions. The estimated LTF will give a stable, closed-loop system over the observed bandwidth, given the gains are correctly applied.
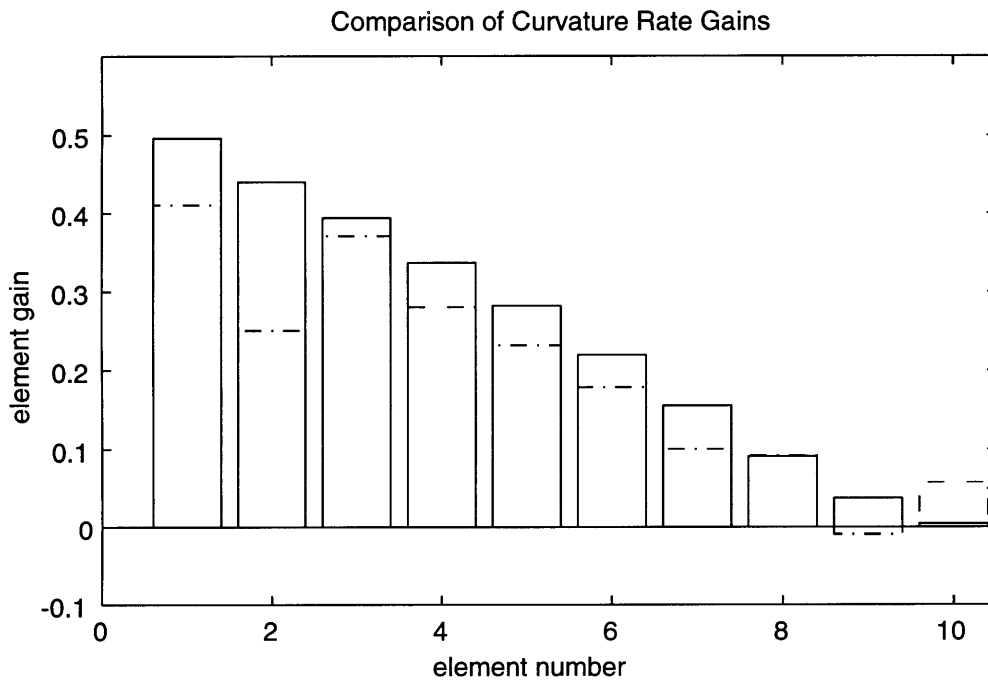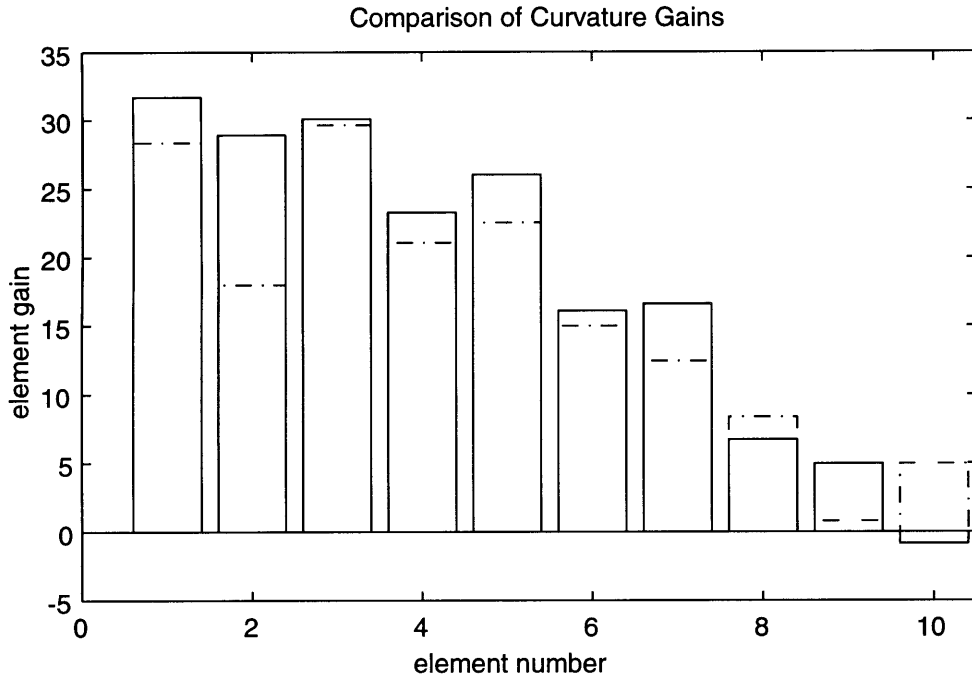
**Figure 5.13:** Comparison of optimum gains (dash-dotted) with their initial guesses (solid). The initial guesses were obtained by applying Method 2 to the modeled sensor element transfer functions.

sensor-element signals $V_p$ by

$$G_{channel\,p}(j\omega) \;=\; g_{cr\,ker_p} + g_{cker_p}\,\frac{1}{\left(j\omega + 2\pi p_c\right)}. \tag{5.8}$$

The compensator also sums the contributions from each element, represented by

$$G_{fit1} + G_{fit2} \;=\; \sum_{p=1}^{10} G_{channel\,p} \cdot H_p(j\omega). \tag{5.9}$$

Note that a single pole roll-off is used to provide the integration part for each channel. This is because a perfect integrator constructed from analog devices would amplify any small DC offset. The value of $p_c$ was chosen to be 0.1 Hertz, such that over the effective control bandwidth, each compensator channel resembled Equation 5.10.

$$G_{channel\,p}(j\omega) \;\cong\; g_{cr\,ker_p} + g_{cker_p}\,\frac{1}{(j\omega)}, \qquad j\omega >> 2\pi p_c \tag{5.10}$$

Figure 5.14 shows the measured transfer function represented by Equation 5.9. There were small high frequency errors introduced by the analog circuitry. The presence of the errors required that a single pole roll-off be applied to the output of the compensator to provide stability. The roll-off pole was placed at 267 Hertz, which was sufficiently above the bending modes that the control design was working to penalize. Figure 5.15 shows the modeled and measured open and closed-loop performance transfer functions for the differenced-displacement regulator. The agreement between the measured and model performance outputs verify the success of the rectangular sensor array control design.

The roll-off that was applied to the control signal is not an unusual step or an undesired one, but it would have been of particular interest to have all the

Modeled vs. Measured LTF
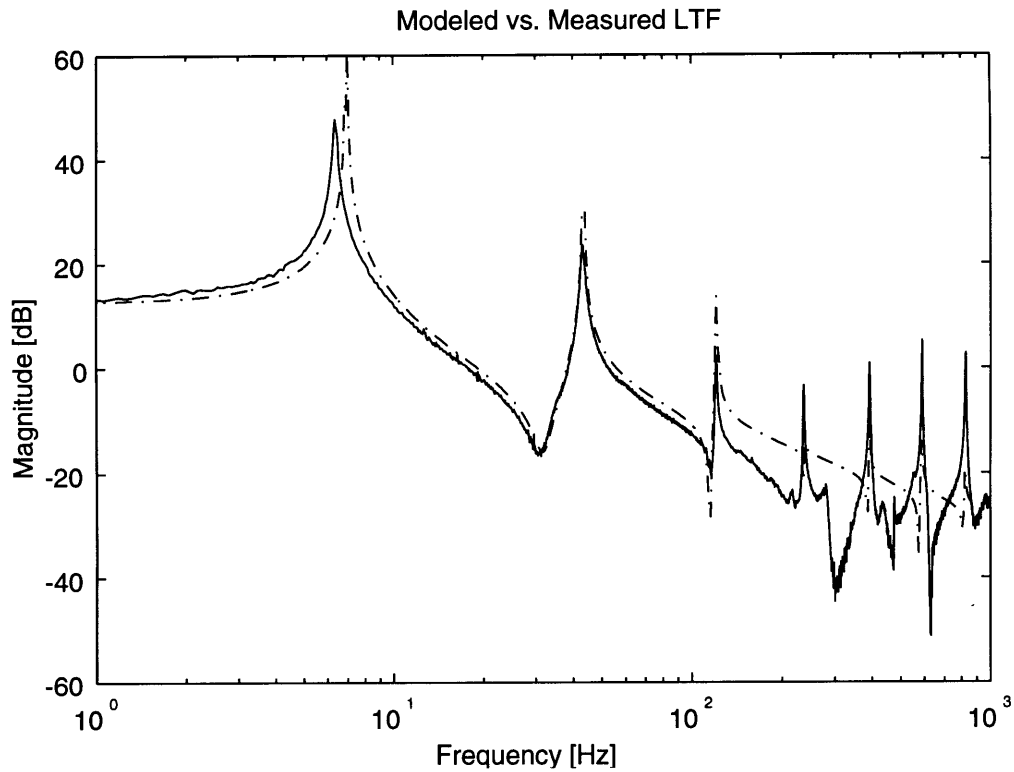
**Figure 5.14:** Desired LTF (dash-dotted) versus measured LTF (solid) generated from sensor-element transfer functions. The measured LTF has an added control roll-off at 267 Hertz to guarantee a stable, closed-loop system over and above the observed bandwidth. The control design primarily penalizes the first and second modes. It is also designed to slightly affect the third mode. Since the control roll-off has been added to the measured LTF, the third mode will not be affected in the implementation.

properties of the desired LTF estimate integrated into the shapes or the choice of gains. The presence of high frequency errors introduced by the circuitry prevented this, and typically all control designs are limited by such errors and require a roll-off to prevent any interference from them.

Modeled OL and CL Performance Transfer Functions
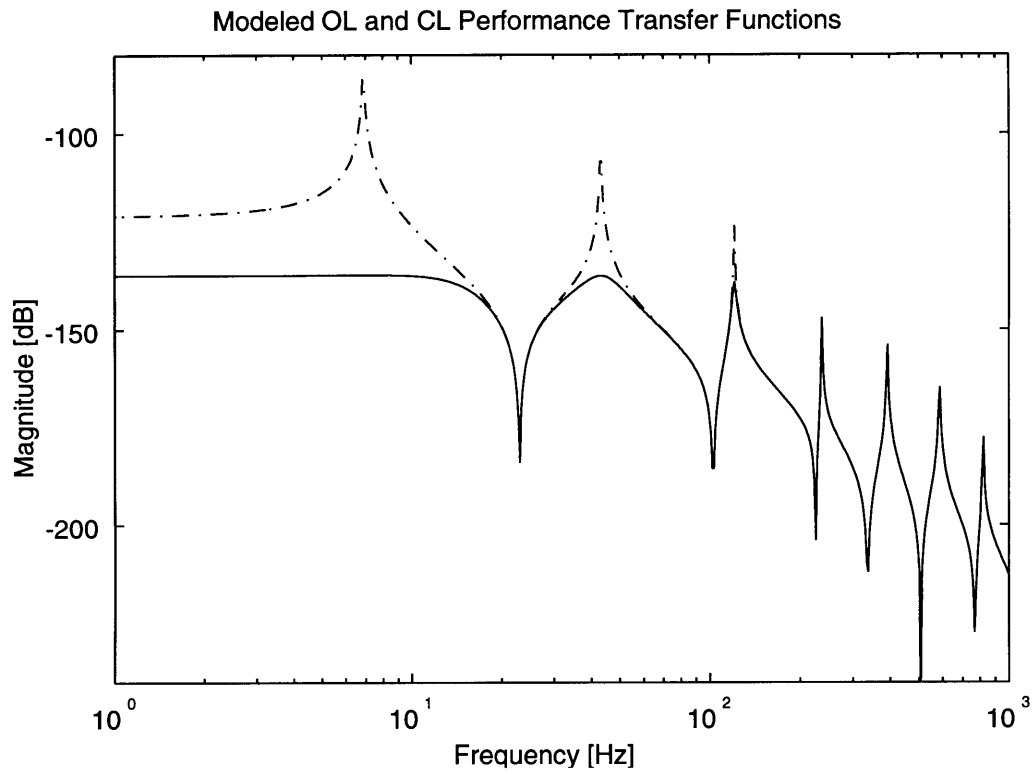
**Figure 5.15a:** Modeled open-loop (dash-dotted) and closed-loop (solid) performance output transfer functions for the LQR differenced-displacement control design. Control and actuator roll-off included in the model.

115
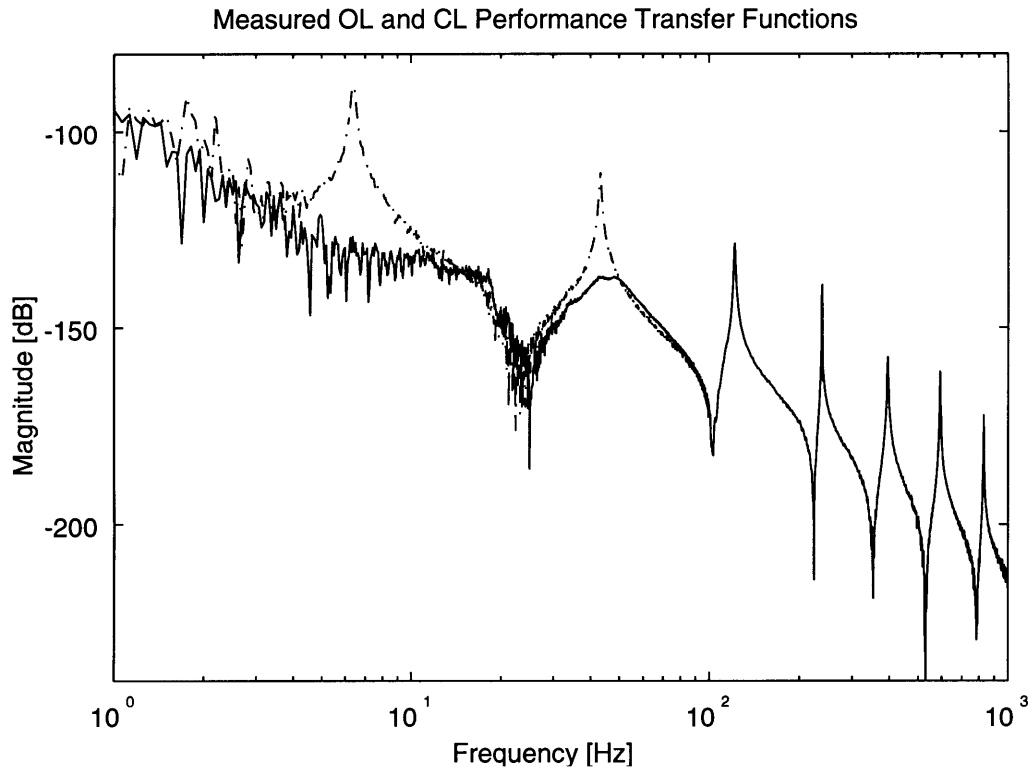
**Figure 5.15b:** Measured open-loop (dash-dotted) and closed-loop (solid) performance output transfer functions for the LQR differenced-displacement control design.

**Figure 5.15c:** Comparison of measured (solid) and modeled (dash-dotted) closed-loop performance output transfer functions for the LQR differenced-displacement control design.

# Chapter 6

# Conclusions and Recommendations

## 6.1 SUMMARY

The goal of this work was to implement a number of Linear Quadratic Regulator (LQR) control designs on a cantilevered beam using polyv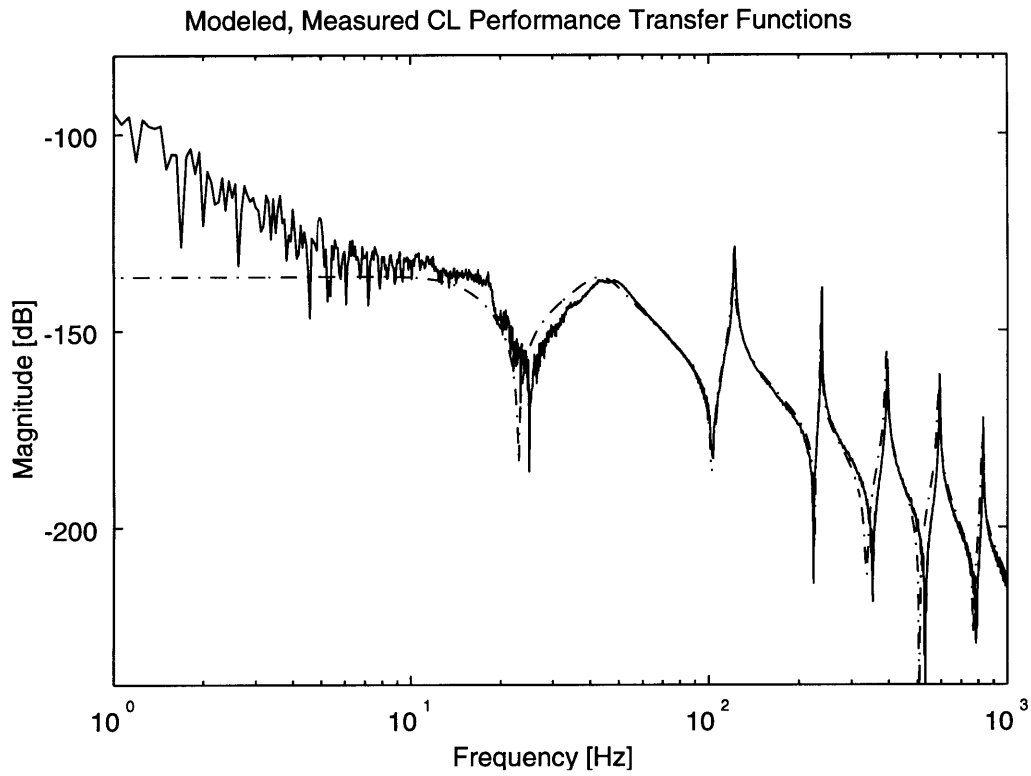inylidene floride (PVDF) area averaging sensors. The control designs were based on the infinite-order LQR formulations for the cantilevered beam. The feedback control signal in this formulation is the convolution of the continuous curvature state functions of the beam with spatially distributed feedback kernels. The implementation of the feedback control required distributed curvature measurements. This type of measurement can be provided for using PVDF area averaging sensors.

PVDF area averaging sensors are distributed, piezoelectric, surface strain sensors. They consist of a thin layer of PVDF film with metal electrodes vapor-deposited on each side. The voltage output of a PVDF area averaging sensor attached to a cantilevered beam is proportional to the convolution of the curvature state function of the beam with the spatial sensitivity weighting function of the sensor. The spatial sensitivity weighting is determined from the shape of the sensor electrodes. To implement the LQR control design, the spatial weightings for the sensors were chosen to be the feedback kernels associated with the infinite-order LQR control design.

A method of calculating the kernels for specific LQR control designs was accomplished by using an extrapolation of a set of discrete feedback gains. The feedback gains were obtained from a finite-order LQR control design. The extrapolation was based on the one-dimensional finite element interpolation functions for a Bernoulli-Euler beam. An estimate of the spatially distributed feedback kernels could be found based on the set of feedback gains. Each estimate was dependent on the order of the model used to find the gains. A set of models of increasing order were used in unison to extrapolate the infinite-order feedback kernels.

To verify the validity of the kernels, a wave model was created which would capture the behavior of the PVDF area averaging sensors on the beam. The wave model produced the loop transfer function (LTF) that would be generated from the output of the sensors. This wave model LTF was compared to a high-fidelity finite element model LTF. The high-order finite element model gave an accurate prediction of the desired LTF needed to implement the control. If sufficiently accurate predictions of the kernels were made, the wave model LTF and the high-order model LTF would be in good agreement. The results showed that the methodology used to find the kernels was valid. The control design could be implemented as long as the test structure remained within the Bernoulli-Euler modeling regime. The results were reinforced by experimental implementation.

For an experiment which penalized the tip displacement of the beam, the associated sensors were implemented experimentally. Although there were slight errors, the measured closed-loop performance for the experiment matched the predictions well. For another experiment which penalized the difference between the tip and mid-point displacement of the beam, the presence of non-idealities hindered the achievement of closed-loop results. Many tests and

simulations were done to attempt to quantitatively define the non-idealities, but no definition was found.

An alternate design technique was investigated and implemented. The technique used an array of rectangular area averaging sensor elements to mimic the behavior of the kernel-shaped sensors. The rectangular shapes were chosen for the sensor electrode patterns since their behavior could be modeled accurately. The rectangular array design was advantageous in that it was adjustable, and it could accommodate many different control designs. The sensor array design also exposed the presence of non-ideal conditions near the root of the test beam. The non-idealities were environmentally-induced errors, and they may have been the cause of the problems with the second experiment. The non-idealities were compensated for, and successful closed-loop results were achieved with the rectangular sensor array design.

## 6.2 CONCLUSIONS AND RECOMMENDATIONS

A successful control application was achieved using PVDF area averaging sensors. The film sensors were integrated into the fabrication of the cantilevered structure with ease. They did not significantly alter the structure's dynamics. Tip accelerometer measurements before and after the application of the sensors were approximately identical. Only very simple circuitry was needed along with the sensors to apply the control design, and even in the presence of environmentally-induced errors, the sensors could assist in substantially reducing the vibrations associated with the lower modes of a structure. Considering the results seen in the above experiments, the best design employed the rectangular sensor elements. In this design, the issues associated with etching were removed, and the adjust-ability allowed for the implementation of

different control designs as well as the ability to optimize the design in the presence of the errors. Though the sensor array used rectangular shapes for the sensor electrodes, it is possible that more flexibility could be gained with trapezoidal shapes, as future research may show. A series of trapezoidal shapes can possibly make a better approximation of the curvature kernels needed to implement the LQR control designs.

The best improvement would come from clearly defining the errors seen in the second and third experiments. It was hypothesized that conditions at the root might be responsible for the errors seen in the experiments. At the root, the beam experiences large stress concentrations. It is possible that the stresses caused the first element to operate above its linear voltage-to-strain region. The remedy might come from reducing the level of actuation the beam experiences.

Also at the root, the rotation angle may not have not been exactly zero due to any motion of the blocks used for the clamp. It was observed that the first element was most sensitive to the bench and clamp dynamics. Any perturbations experienced by the bench and the clamp would increase the level of which their dynamics were seen in the data for the first element. The remedy for this lies in the creation of a more rigid clamp and bench for future experiments.

If the problem was solely due to the clamped boundary condition, then rectangular sensor-element array design presented an effective way to counteract the affects caused by the non-ideal clamp. Many structural beam elements in applications are modeled as cantilevered beams when, in reality, they are not. The adjust-ability of the rectangular array design can successfully compensate for this. Also, it would not be difficult to alter the modeling of the beam to allow for a less rigid boundary condition. The control theory for the infinite-order LQR control design can account for rigid body motions, however small they might be.

The application of the control design without the rigid body contributions could be observed to verify if their absence could cause the problems seen.

The only theory remaining that was not fully investigated was the film-epoxy-beam interaction. The analysis of the interaction may turn out to be laborious but necessary. As an alternative, relying only on the theory developed in this thesis, more experiments may help to reveal the cause of the errors. The investigation of a beam with a single sensor element located near the root may be beneficial. It may also be beneficial to divide the element near the root into a number of smaller segments. This might further clarify if the errors are a function of the larger stresses or the slight non-idealities near the root.

# Bibliography

[1]     Van de Vegte, J., Feedback Control Systems, Prentice-Hall, Inc., New Jersey, 1990.

[2]     *KYNAR* Piezo Film Technical Manual, Pennwalt Corp., Valley Forge, PA, 65 pp., 1987.

[3]     Collins, S., Dr. D. W. Miller, and Dr. A. H. von Flotow, "Sensors for Structural Control Applications Using Piezoelectric Polymer Film", S. M. Thesis, Massachusetts Institute of Technology, Cambridge, MA., 1990.

[4]     Collins, S., Dr. D. W. Miller, and Dr. A. H. von Flotow, "Distributed Sensors as Spatial Filters in Active Structural Control", to appear in Journal of Sound and Vibration, Vol. 170, No. 2., 1994.

[5]     Lee, C. K., and F. C. Moon, "Modal Sensors/Actuators", Journal of Applied Mechanics, Vol. 57, No. 2, pp. 434 - 441, June 1990.

[6]     Miller, S. E., and J. Hubbard, "Theoretical and Experimental Analysis of Spatially Distributed Sensors on a Bernoulli-Euler Beam", C. S. Draper Laboratory Report CSDL-C-5953, Cambridge, MA., July 1987.

[7]     Miller, Dr. D. W., and Dr. M. van Schoor, "Formulation of Full State Feedback for Infinite-order Structural Systems", Massachusetts Institute of Technology, Cambridge, MA., 1989.

[8]     Kwakernaak, H. and R. Sivan, Linear Optimal Control Systems, John Wiley and Sons, Inc., New York, 1972.

[9]   de Luis, J., Prof. E. Crawley, and Prof. S. Hall, "Design and Implementation of Optimal Controllers for Intelligent Structures Using Infinite-order Structural Models", Space Systems Laboratory Report No. 3-89, Massachusetts Institute of Technology, Cambridge, MA., 1989.

[10]  Bathe, Klaus-Jürgen, <u>Finite Element Procedures in Engineering Analysis</u>, Prentice-Hall, Inc., New Jersey, 1982.

[11]  Crawley, Prof. E., and Prof. S. Hall, "The Dynamics of Controlled Structures", Space Engineering Research Center Report, No. 10-91-I., Massachusetts Institute of Technology, Cambridge, MA., 1991.

[12]  Yang, T. Y., <u>Finite Element Structural Analysis</u>, Prentice-Hall, Inc., New Jersey, 1986.

[13]  Strang, Prof. G., <u>Introduction to Applied Mathematics</u>, Wellesley-Cambridge Press, Wellesley, MA., 1986.

[14]  Miller, Dr. D. W., "Modeling and Active Modification of Wave Scattering in Structural Networks", Ph. D. Thesis, Department of Aeronautics and Astronautics, Massachusetts Institute of Technology, May, 1988.

[15]  Miller, Dr. D. W., and Prof. A. von Flotow, "A Traveling Wave Approach to Power Flow in Structural Dynamics", Journal of Sound and Vibration, Vol. 128, No. 1, pp. 145-162., 1989.

[16]  Jacques, R., "On-Line System Identification and Control Design for Flexible Structures", Ph. D. Thesis, Department of Aeronautics and Astronautics, Massachusetts Institute of Technology, May, 1994.

[17]  Lindner, D. K., K. M. Reichard, and W. T. Baumann, "Measurement and Control of Structures Using Distributed Sensors", Proceedings of the 29th Conference on Decision and Control, Honolulu, Hawaii, December 1990.

[18]    Miller, Dr. D. W., R. N. Jacques, and J. de Luis, "Typical Section Problems for Structural Control Applications", Paper No. AIAA-90-1225, presented at the Dynamics Specialist Conference, Long Beach, CA., April 1990.

[19]    Cady, W. G., Piezoelectricity, Dover Publications, Inc., New York, 1964.

[20]    Kawai, H., "The Piezoelectricity of Poly(vinylidene Floride)", Japan Journal of Applied Physics, Vol. 8, No. 7, pp. 975 - 976, July 1969.

[21]    Sessler, G. M. , "Piezoelectricity in Polyvinylidene Floride", Journal of the Acoustical Society of America, Vol. 70, No. 6, pp. 1567 - 1576, December 1981.

[22]    Meirovitch, L., Analytical Methods in Vibrations, Macmillan Publishing Co., Inc., New York, 1967.

[23]    Timoshenko, S., D. H. Young, and W. Weaver, Jr., Vibration Problems in Engineering, John Wiley and Sons, Inc., New York, 1974.

[24]    Blevins, R. D., Formulas for Natural Frequency and Mode Shape, Robert E. Krieger Publishing Company, New York, 1967.

[25]    Strang, Prof. G., Linear Algebra and its Applications, Harcourt Brace Jovanovitch, Inc., Orlando, Florida, 1976.

[26]    French, A. P., Vibrations and Waves, W. W. Norton and Company, New York, 1971.

[27]    Burke, S. E., J. E. Hubbard, "Active Vibration Control of a Simply-Supported Beam Using a Spatially Distributed Actuator", IEEE Control Systems Magazine, Vol. 7, No. 4, pp. 25 - 30, August 1987.

[28]    Athens, M., P. L. Falb, Optimal Control, McGraw-Hill Book Company, New York, 1966.

[29]   Edwards, C., D. Penny, <u>Elementary Differential Equations with Boundary Value Problems</u>, Prentice Hall, Inc., New Jersey, 1989.

[30]   Thomas, G., R. Finney, <u>Calculus and Analytic Geometry</u>, Addison-Wesley Publishing Company, Reading, Massachusetts, 1988.

[31]   Andersson, M. S., Prof. E. Crawley, "Discrete Distributed Strain Sensing of Intelligent Structures", 2nd Annual U. S. / Japan Conference on Adaptive Structures, Nagoya, Japan, November 12 - 14, 1991.